UC San Diego
UC San Diego Electronic Theses and Dissertations

Title

The Small Magellanic Cloud: Dust Extinction and Three-Dimensional Structure from Hubble Space Telescope Observations

Permalink

https://escholarship.org/uc/item/0vx1d05p

Author

Yanchulova, Petia

Publication Date

2020

Peer reviewed|Thesis/dissertation

UNIVERSITY OF CALIFORNIA SAN DIEGO

The Small Magellanic Cloud: Dust Extinction and Three-Dimensional Structure from Hubble
Space Telescope Observations

A dissertation submitted in partial satisfaction of the
requirements for the degree of Doctor of Philosophy

in

Physics

by

Petia Yanchulova

Committee in charge:

  Professor Karin M. Sandstrom, Chair
  Professor James M.D. Day
  Professor George M. Fuller
  Professor Dušan Kereš
  Professor Mark H. Thiemens

2020

The Dissertation of Petia Yanchulova is approved, and it is acceptable in quality

and form for publication on microfilm and electronically:

_____

_____

_____

_____

Chair

University of California San Diego

2020

DEDICATION

To my parents, Nina and Todor Yanchulovy,
sister, Lina Yanchulova Taylor,
and husband, Tristan Merica-Jones.

EPIGRAPH

The heavens declare the glory of God;
    the skies proclaim the work of his hands.
Day after day they pour forth speech;
    night after night they reveal knowledge.
They have no speech, they use no words;
    no sound is heard from them.
Yet their voice goes out into all the earth,
    their words to the ends of the world.
In the heavens God has pitched a tent for the sun.
    It is like a bridegroom coming out of his chamber,
like a champion rejoicing to run his course.
    It rises at one end of the heavens
and makes its circuit to the other;
    nothing is deprived of its warmth.
The law of the Lord is perfect,
    refreshing the soul.
The statutes of the Lord are trustworthy,
    making wise the simple.
The precepts of the Lord are right,
    giving joy to the heart.
The commands of the Lord are radiant,
    giving light to the eyes.
The fear of the Lord is pure,
    enduring forever.
The decrees of the Lord are firm,
    and all of them are righteous.
They are more precious than gold,
    than much pure gold;
they are sweeter than honey,
    than honey from the honeycomb.
By them your servant is warned;
    in keeping them there is great reward.
But who can discern their own errors?
    Forgive my hidden faults.
Keep your servant also from willful sins;
    may they not rule over me.
Then I will be blameless,
    innocent of great transgression.
May these words of my mouth and this meditation of my heart
    be pleasing in your sight,
Lord, my Rock and my Redeemer.

Psalm 19

TABLE OF CONTENTS

LIST OF FIGURES

LIST OF TABLES

VITA

2000	B.A., International Relations, University of San Diego
2012-2013	Graduate Student Researcher, Teaching Assistant Department of Astronomy, University of Washington
2013–2015	Teaching Assistant, University of California San Diego
2015–2020	Graduate Student Researcher, Center for Astrophysics and Space Sciences, University of California San Diego
2017	M.S., Physics, University of California San Diego
2020	Ph.D., Physics, University of California San Diego

PUBLICATIONS

Yanchulova Merica-Jones, P., Sandstrom, K.M., Johnson, L.C., Dolphin, A.E., Dalcanton, J., Gordon, K., Roman-Duval, J., Weisz, D.R., Williams, B.F., *Three-Dimensional Structure and Dust Extinction in the Small Magellanic Cloud*, August 2020, Submitted to The Astrophysical Journal

Roman-Duval, J., Jenkins, E.B., Tchernyshyov, K., Williams, B., Clark, C.J.R., Gordon, K.D., Meixner, M., Hagen, L., Peek, J., Sandstrom, K., Werk, J., Yanchulova Merica-Jones, P., *METAL: The Metal Evolution, Transport, and Abundance in the Large Magellanic Cloud Hubble Program. II. Variations of Interstellar Depletions and Dust-to-gas Ratio Within the LMC*, September 2020, Submitted to The Astrophysical Journal

Roman-Duval, J., Jenkins, E.B., Williams, B.F., Tchernyshyov, K., Gordon, K., Meixner, M., Hagen, L., Peek, J., Sandstrom, K.M., Werk, J., Yanchulova Merica-Jones, P., *METAL: The Metal Evolution, Transport, and Abundance in the Large Magellanic Cloud Hubble Program. I. Overview and Initial Results*, The Astrophysical Journal, Vol 871, pp151:178, February 2019

Yanchulova Merica-Jones, P., Sandstrom, K.M., Johnson, L.C., Dalcanton, J., Dolphin, A.E., Gordon, K., Roman-Duval, J., Weisz, D.R., Williams, B.F., *The Small Magellanic Cloud Investigation of Dust and Gas Evolution (SMIDGE): The Dust Extinction Curve from Red Clump Stars*, The Astrophysical Journal, Vol 847, pp 102–118, October 2017

Chakraborty, S., Yanchulova P., Thiemens, M.H. *Mass-Independent Oxygen Isotopic Partitioning During Gas-Phase SiO_2 Formation*, Science, 342, 463, October 2013

ABSTRACT OF THE DISSERTATION

The Small Magellanic Cloud: Dust Extinction and Three-Dimensional Structure from Hubble
Space Telescope Observations

by

Petia Yanchulova

Doctor of Philosophy in Physics

University of California San Diego, 2020

Professor Karin M. Sandstrom, Chair

Interstellar dust is a ubiquitous component of galaxies, but some of its most fundamental
properties are still poorly understood. This work analyzes the average extinction properties
of dust in the Small Magellanic Cloud (SMC) through color-magnitude diagrams (CMDs) of
resolved stars observed with the Hubble Space Telescope (HST). It also investigates the three-
dimensional structure of the SMC, since the galaxy's proximity and dynamic interaction history
provide a unique way to simultaneously study both dust extinction and galactic geometry. The
observations are taken as part of the Small Magellanic Cloud Investigation of Dust and Gas
Evolution (SMIDGE) program examining a 200×100 parsec region in the SW bar of the SMC.

SMC-like dust extinction is frequently used to correct observations of high-redshift
or low-metallicity galaxies due to SMC's own low metallicity (Gordon et al., 2003). The

dust extinction law, or extinction curve, describing the stellar extinction in magnitudes as a function wavelength is the quantity used for this purpose. Fundamentally, the extinction law holds information about the dust grain size and composition. The SMIDGE survey has made it possible to find the average dust extinction properties in the SMC and build upon the handful of measurements in existence prior to the survey.

Chapter 1 is an introduction to the importance of SMC dust extinction curve and galactic geometry measurements, and to the approach taken here to answer questions about these two measurements. Chapter 2 explores the average SMC dust extinction curve through multiband HST photometric observations of evolved red clump stars. The study focuses on the measurement of the slope of the red clump reddening vector from the CMD relying on a simple model which takes into account the extinction curve shape, a log-normal distribution of extinctions, and the distance distribution of the stellar component along the line of sight. The results for the shape of the average SMC extinction curve are consistent with prior measurements, and also point to a significant galactic depth along the line-of-sight, in line with recent studies.

Chapter 3 describes work on a more complex model for the SMC, using red clump and red giant branch stars on a CMD. The model simulates the dust-stars offset and the stellar distance distribution, yielding the reddened fraction of stars. It also simulates a dust layer with a log-normal extinction distribution A_V - the extinction in magnitudes in the optical V photometric band - with width σ_{A_V}. This work results in the first detailed dust extinction and 3D geometry properties in a key region in the SMC. It also produces a photometry-based A_V result allowing for a measurement of the dust mass content of the galaxy which is independent from infrared dust emission observations. This is one of a few measurements of A_V at low metallicity which can be compared to gas and dust content measured from infrared emission. Similarly to other photometry-based extinction results in Andromeda and the Milky Way, it points to a potential overestimation of the dust mass derived from dust grain models relying on IR dust emission data.

Chapter 4 summarizes this dissertation and describes future work on SMC's dust extinction properties. This future study relies on the results derived in Chapter 3 to obtain a

refined SMC average dust extinction curve. It also aims to obtain spatially-resolved maps of the extinction curve and A_V in order to answer questions about the distribution of SMC extinction curves.

Chapter 1

Introduction

Interstellar dust properties, and in particular dust's absorption and scattering effects on starlight - i.e., extinction - are not yet fully understood. Yet dust affects almost all astronomical observations and is a fundamentally-important component of galaxies. It interacts with light at a range of wavelengths and provides surface area for gas-phase chemical reactions. As a result, dust causes changes in the brightness and color of almost all astronomical objects, shields regions of dense molecular gas from UV photodissociation, and its formation causes a depletion of the elements. Further, it catalyzes the formation of the H_2 molecule (a precursor to star formation) and acts as the progenitor of planetary systems (Trumpler, 1930; Gould & Salpeter, 1963; Draine, 2003).

Dust grains are primarily composed of C, O, Mg, Si, S, and Fe, which are some of the most abundant elements able to undergo condensation into solid grains. Infrared emission observed from dust around evolved stars, such as red giants and carbon stars, and planetary nebulae, shows that dust is present in stellar winds and outflows (Fleischer et al., 1992; Netzer & Elitzur, 1993; Winters et al., 2003; Speck et al., 2009). These observations indicate that dust grains condensed out of the gaseous form and either formed in stellar atmospheres or in the stellar outflows themselves, and were then blown into the interstellar medium (ISM), which is the gas and dust between the stars. Isotopic evidence from presolar grains in meteorites supports the notion that dust formed from stellar outflows, and that some of this dust comes from

supernova ejecta (Hoppe & Zinner, 2000; Hoppe et al., 2012). Dust can also form by growth inside protoplanetary disks (Testi et al., 2014; Compiègne et al., 2011) or the ISM through the processes of coagulation and accretion in amounts dependent on the initial abundances of the grains (Zhukovska et al., 2008). The evolution of dust in the ISM depends on the formation-destruction balance, and also on the dust-to-gas and dust-to-metals ratios, which in turn indicate a dependence on the fraction of heavy elements.

Understanding the evolution of interstellar dust properties from the ancient Universe to the present is key to understanding galactic evolution itself. Studies of our own Milky Way (MW) have laid the foundations for understanding the properties of dust. However, there are inherent challenges with interpreting MW observations due to the complex distribution of stars and dust along the line of sight, and uncertainties in MW distances and the global galactic structure. Additionally, the MW has evolved significantly, and its current conditions may not be representative of distant, young galaxies. The SMC, on the other hand more closely resembles a primordial galaxy in that ISM do not seem to have been processed to the degree observed in the MW. High-redshift (distant and young) galaxies are thought to have produced stars most abundantly in an ISM more like the SMC's than the Milky Way's (Madau & Dickinson, 2014). The SMC is also nearby: its apparent size on the sky is almost twice that of Andromeda (the nearest massive galaxy) and it is ~10 times closer. This work therefore focuses on the SMC as one of the most suitable galaxies where the properties of dust extinction and its relationship to galactic geometry can be examined in the context of an environment similar to the early Universe.

The SMC is a dwarf irregular satellite galaxy of the Milky Way located at ~62 kpc (~200,000 light years, Scowcroft et al., 2016) and is a part of the Local Group of galaxies. Due to their relative proximity, Local Group galaxies present a unique opportunity to measure the properties of galactic structure, star formation, and dust extinction. This is because many galactic processes and features can be well-understood only when they are studied on scales where individual stars and molecular clouds are spatially resolved. Further, spatial variations in these properties can currently be reliably measured only through Local Group studies.

The SMC is especially useful for studying the properties of the ISM and its evolution as it relates to star formation and ultimately to galaxy evolution. This is due in large part to SMC's relatively low content of heavy elements (elements other than H or He), also known as "metallicity", Z. While the solar metallicity is $Z_\odot \simeq 0.014$ (Asplund et al., 2009) – where solar abundances are assumed to be similar to the total abundances of the MW ISM today – the SMC today has only $1/5 - 1/8$ $Z_\odot$ (Dufour, 1984; Russell & Dopita, 1992; Kurt et al., 1999; Lee et al., 2005; Rolleston et al., 1999, 2003). For comparison, the peak of star formation in the Universe most likely occurred at ~$0.01 - 0.06$ $Z_\odot$ (Madau & Dickinson, 2014). At the same time, all massive galaxies seem to have undergone chemical enrichment, thus the SMC can inform us about star formation and evolution in the MW as well due to MW's own metallicity evolution.

Starlight is scattered and absorbed by dust, leading to its extinction. The wavelength-dependent attenuation of light is represented by the extinction curve. A sample of Milky Way and Magellanic Clouds (LMC and SMC) curves is shown in Figure 1.1. The extinction at wavelength λ is measured in magnitudes and is expressed as A_λ, where, for instance, the extinction in the optical B and V photometric bands (at 4405 Å and 5470 Å) is A_B and A_V. The extinction curve is generally described by the parameter $R_V \equiv A_V/(A_B - A_V)$, which is a dimensionless ratio of total to selective extinction (the latter also known as "reddening") at visible wavelengths (Cardelli et al., 1989). R_V is reflective of the dust grain size and composition, as these are the main properties which determine how dust interacts with light. R_V can be transformed to R_λ to express the extinction curve shape in a chosen wavelength combination. In Chapter 2, for example, we measure $R_{475} = A_{475}/(A_{475} - A_{814})$ as the ratio of absolute to selective extinction in the Hubble Space Telescope optical $F475W$ and infrared $F814W$ photometric bands.

The amount and type of dust seems to be strongly dependent on metallicity (e.g. Dwek, 1998; Zubko, 1999; Clayton et al., 2003; Sofia et al., 2006; Zhukovska et al., 2008; Asano et al., 2013; Rémy-Ruyer et al., 2014; Roman-Duval et al., 2014; Feldmann, 2015; Chastenet et al., 2019; De Vis et al., 2019). A consequence of this is that dust extinction in turn changes significantly in a low-metallicity environment (i.e., Gordon et al., 2003). For example, it appears
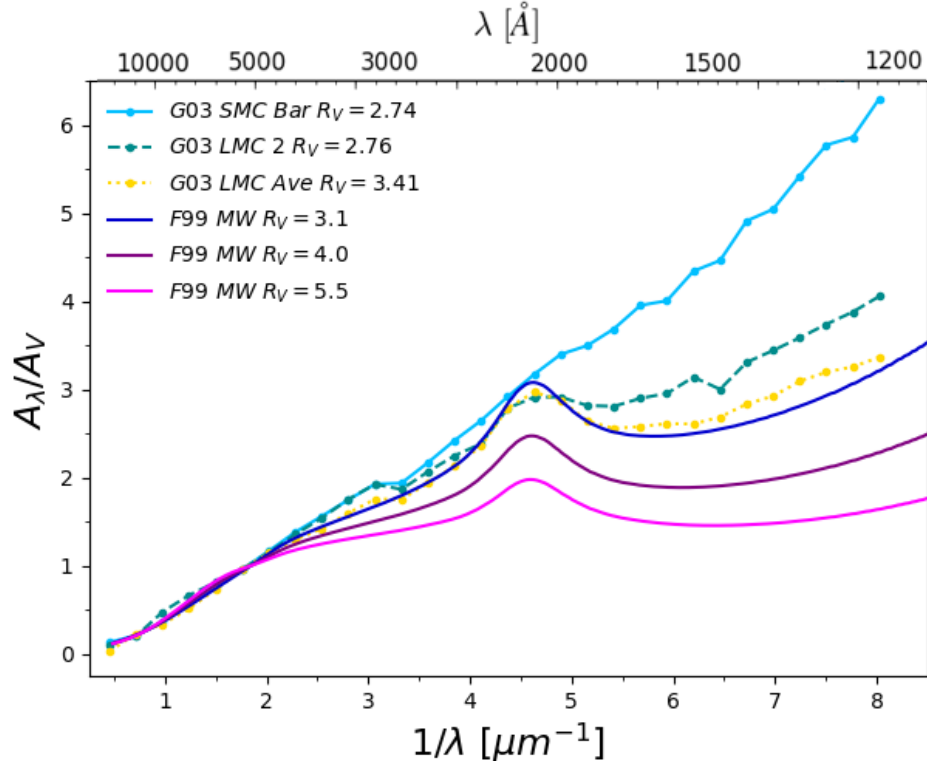
Figure 1.1. Extinction curves for the Milky Way (MW, Fitzpatrick, 1999) and the Large & Small Magellanic Clouds (Gordon et al., 2003) show the wavelength dependence of interstellar extinction and are indicative of the composition and size distribution of dust grains. The range of extinction properties clearly seen in the UV reflects the optical properties of grains along the line of sight and may indicate differences in dust grain processing in the ISM. Extinction is highest at a wavelength comparable to the size of the grains ($a/\lambda \approx 1$). MW variations are well-described by properties of the diffuse (dark blue) and dense (magenta) gas. A larger extinction at shorter wavelengths (such as in the SMC Bar in light blue) indicates a larger fraction of smaller dust grains. The SMC curve lacks a 2175 Å bump (seen in MW & LMC sightlines), which is thought to be produced primarily by absorption by polycyclic aromatic hydrocarbons (PAHs).

that extinction features at UV wavelengths at low-Z are quite distinct from those in the Milky Way (an evolved high-Z galaxy) in that they experience a steep UV rise and lack or show a weak 2175 Å "bump". These SMC and MW extinction curve differences are significant, and this is why SMC-like dust extinction is the primary model used to correct observations of low-metallicity or high-redshift galaxies.

While much is known about Milky Way dust extinction curve properties, information about the SMC's dust extinction curves is limited as it has relied on results derived from a sample of less than ten stars. The traditional method to study dust extinction curves has been through the "pair" method (Trumpler, 1930; Massa et al., 1983; Cardelli et al., 1992; Gordon et al., 2003) where the spectra of a reddened and an unreddened star of a known spectral type are compared. In this sense only a few lines of sight requiring high signal-to-noise UV spectroscopy can be explored at one time due to the time-consuming nature of the observations done on a star-by-star basis from space. These selected stars are often UV-bright objects of spectral type O and B which are giant, massive stars residing in the vicinity of star-forming regions whose intense radiation field may alter dust grain, and therefore dust extinction, properties. It has therefore remained unknown whether the dust extinction properties derived from these select stars/regions can be universally applied to the rest of the SMC, and therefore to low-metallicity and/or high-redshift systems for which the SMC is considered a proxy.

This work addresses these potential drawbacks through a significant modification of the pair method. The approach enables an analysis of the average extinction curve and dust extinction properties in the SMC through spatially-resolved observations of stars which are expected to randomly sample the distribution of gas and dust in the ISM. Such observations are made possible by The Hubble Space Telescope which takes simultaneous images of hundreds of thousands of stars in photometric bands spanning the UV-IR wavelength range. These multiband observations can then be compared to theoretical predictions of a star's color and magnitude instead of to spectral observations of a comparison star. The stars' displacement from a known unreddened location on a color-magnitude diagram can be measured across photometric bands

to extract the extinction at a given wavelength and find the extinction curve shape.

Another advantage of CMD-based extinction studies beside finding the extinction curve shape is that they provide a way to measure a galaxy's or a region's dust mass independently from infrared dust emission observations. The dust mass can be estimated by fitting the observed shape of the spectral energy distribution (SED; emitted energy as a function of wavelength) from IR emission to the emission spectrum of dust predicted by dust grain models. The models are fairly complex and specify the dust temperature (governed by the starlight intensity), the grain composition, abundance, and size distribution, the assumed grain emissivity and opacity, and other grain properties. A series of relationships between the dust mass, the dust mass surface density (dust mass per area), the hydrogen column density N_H (H atoms per area), and the ratio of A_V to N_H can give the line-of-sight dust extinction, A_V (Draine & Li, 2007). Conversely, measuring A_V from CMD-based extinction can give the dust mass, and a self-consistency check can be made.

Notable differences exist between CMD- and emission-based A_V results in Andromeda (M31) and the Milky Way (Draine et al., 2014; Planck Collaboration et al., 2016; Dalcanton et al., 2015) where A_V estimates from IR emission are higher by a factor of $2 - 2.5$ compared to CMD-based A_V measurements. Dalcanton et al. (2015), who make the CMD-based measurement in M31, conclude that the discrepancies are unlikely to be due to CMD A_V measurements errors, but most likely stem from issues with the dust models, the SED fitting, or other assumptions made using IR emission methods. Overestimates in A_V suggest an overestimate in the dust mass. One way to reconcile the results is if a given amount of emission is produced by a smaller amount of dust which would imply that dust grains are more emissive than the model assumes. One significant source of uncertainty in the dust models is the assumed far-IR dust opacity (absorption cross section per unit dust mass). Another related issue stems from the fact that the models are calibrated to match the diffuse ISM in the evolved, high-metallicity Milky Way and may not be accurate under different conditions (including in the MW itself). For example, evolution of dust in the ISM adds to the complexity due to changes in the dust abundances, the dust-to-gas and

6
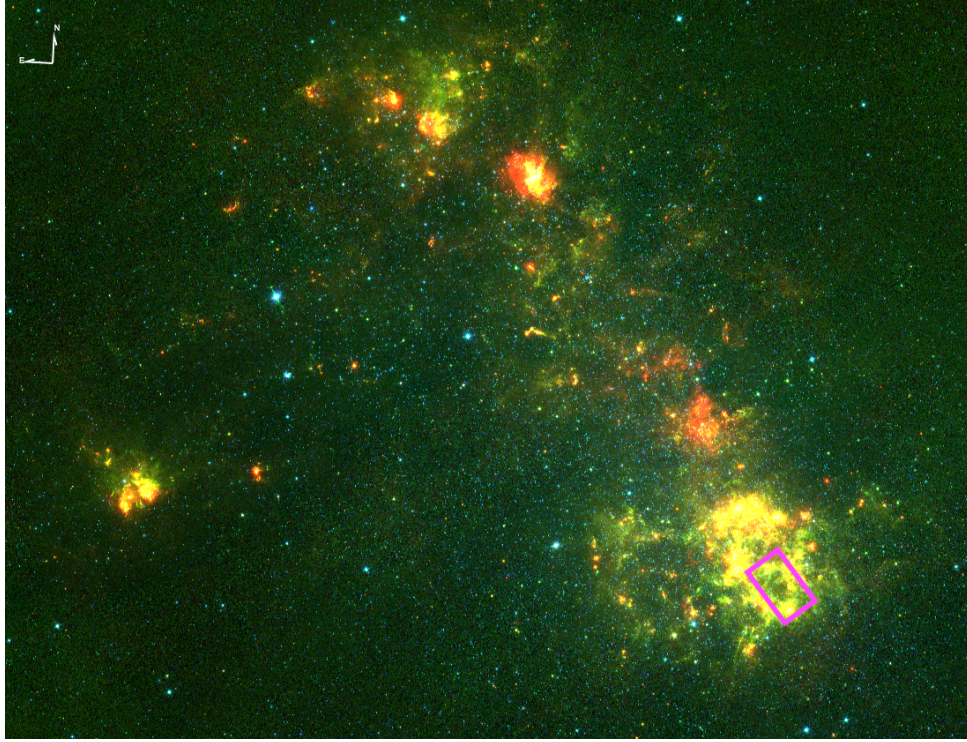
Figure 1.2. The SMIDGE survey field covers a $12' \times 6.5'$ region in the SW bar of the SMC and is overlaid (in magenta) on a Spitzer Space Telescope composite image in 3.6, 8, and 24 μm from the SAGE-SMC survey (Gordon et al., 2011) showing the galaxy's bar/body (center-right) and wing region (left). See Fig. 3.1 for a detailed *HST* camera imaging footprint.

dust-to-metals ratios, and other grain properties which in turn introduce variations in the far-IR dust opacity / measured emission.

A more thorough understanding of far-IR emissivity is therefore necessary in a variety of dust environments at low and high redshifts (looking at nearby / present-day and at distant / young galaxies, respectively). Emission-based dust masses can be calculated for very distant galaxies using observations with the Atacama Large Millimeter/Submillimeter Array. But first the far-IR emissivity of dust at low metallicity needs to be understood. The SMC is a natural choice for a low-Z measurement. This study derives A_V from a CMD-based extinction measurement and performs a consistency check for the dust mass from extinction- and emission-based perspective.

The Small Magellanic Cloud Investigation of Dust and Gas Evolution (SMIDGE) survey was designed specifically to understand the spatial variations of dust extinction and the distribu-

tion of dust extinction curves through resolved maps at low-metallicity. SMIDGE focused on the dustiest spot in the SMC - the Southwest Bar shown in Figure 1.2 - as the most suitable location to enable such mapping and examine the properties of dust grains at low Z. It is now known from detailed observations by the Spitzer Space Telescope that very small and very important dust grains known as polycyclic aromatic hydrocarbons (PAHs) are concentrated in the SW Bar of the galaxy (Sandstrom et al., 2010, 2012). slaPAHs dominate the total dust grain surface area, radiate a large fraction of a galaxy's infrared power, and are believed to be the carriers of the prominent 2175 Å absorption feature of MW and LMC extinction curves (Li & Draine, 2001; Weingartner & Draine, 2001; Zubko et al., 2004; Draine & Fraisse, 2009).

Similarly to observations from the Pan-chromatic Hubble Andromeda Treasury survey (PHAT; Dalcanton et al. (2012)) which have been used to make the first map of extinction properties in an external galaxy (Dalcanton et al., 2015), SMIDGE observations are based on an eight-filter Hubble Space Telescope photometry. Observations in the following broad-band filters were obtained by the Advanced Camera for Surveys (ACS) Wide Field Camera (WFC), and the Wide Field Camera 3 (WFC3) instrument's infrared (IR) and ultraviolet-optical (UVIS) imagers, covering the wavelength range $0.24 - 1.5$ μm: *F225W*, *F275W* and *F336W* from *WFC3/UVIS*; *F475W*, *F550M*, *F658N*, and *F814W* from *ACS/WFC*; and *F110W* and *F160W* from *WFC3/IR*.

The multiband observations provide coverage of stellar SEDs from the near-UV to the near-IR and in this way allow for a distinction to be made between the changes of stellar properties and the changes in extinction since stars populate a color-magnitude diagram differently due to these effects. Similarly to PHAT, the SMIDGE survey was designed to use HST's high angular resolution and depth to obtain observations of hundreds of thousands of individual stars such that extinction measurements in each spatial pixel would be based on stars of different spectral types to give the average extinction properties (versus those based on the pair method targeting individual O- and B-type stars). The PHAT Andromeda dust extinction study focuses on the near-IR CMD ($F110W$ and $F160W$) to study the reddening effects on red giant branch stars. RGB stars in the M31 near-IR CMD occupy a small range of color for a given magnitude (see

Fig. 1.3 for the theoretical optical SMIDGE CMD where the RGB is also nearly vertical). On the theoretical "unreddened" CMD RGB stars should appear as a single, narrow, and an almost vertical sequence, but in the observed M31 CMD the RGB is subject to broadening and bimodality, much like the RGB on the observed SMIDGE CMD discussed below. This effect is due to the displacement of some RGB stars from their theoretical location due to dust extinction and a dust-stars offset, and is what enables the measurement of dust extinction from the M31 CMD.

The effects of dust and galactic geometry on the multiband SMIDGE CMDs are even more prominent due to SMC's proximity. This work takes a slightly different approach from the M31 dust study and examines dust extinction properties in tandem with the 3D geometry of the SMC (the distance and the distribution of the stellar component, and its position relative to the ISM dust layer).

Much observational and theoretical work has been done on studying SMC's galactic structure (Besla et al., 2007; Subramanian & Subramaniam, 2009; Besla et al., 2012; Haschke et al., 2012; Subramanian & Subramaniam, 2012; Nidever et al., 2013; Besla et al., 2016; Jacyszyn-Dobrzeniecka et al., 2016; Subramanian et al., 2017). The results show a highly-elongated galactic shape along the line of sight, perhaps due to SMC's repeated interactions with its neighbor, the Large Magellanic Cloud (LMC). The relative positions of the stars and the ISM in the SMC have not been studied as extensively, but models suggest that the Magellanic System is most likely disrupted due to internal interactions and not gravitational interactions with the Milky Way (Besla et al., 2012; Murray et al., 2019).

Although this dissertation is primarily focused on using the CMD to study dust, both galactic geometry and dust extinction can affect the positions of stars on a color-magnitude diagram (CMD). First, an understanding of the underlying factors governing the intrinsic stellar positions on a CMD are essential. CMDs are used to plot the relationship between the "color" and brightness ("magnitude") of stars in a galaxy. The color can be represented by differences in a chosen magnitude combination and is indicative of the relative temperature of stars. (A related
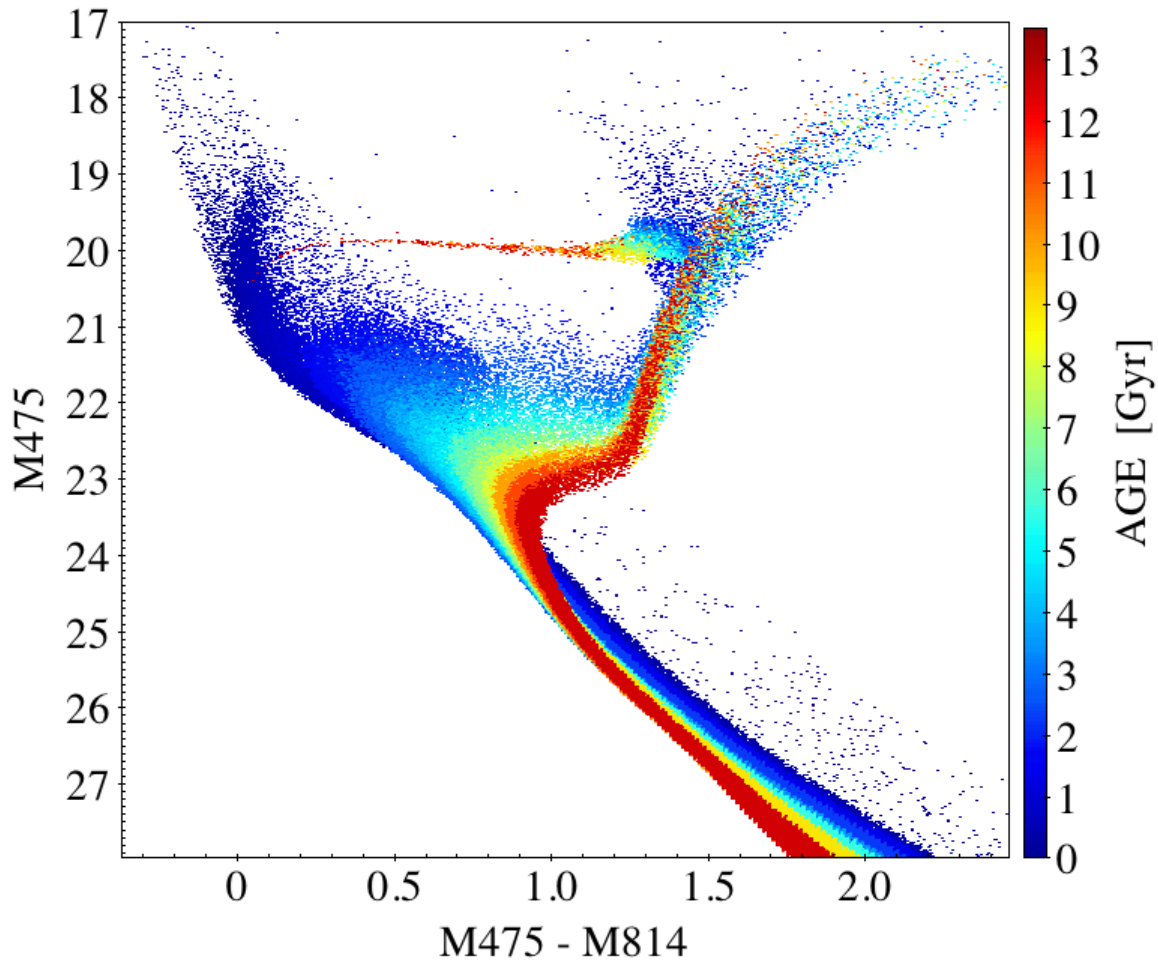
Figure 1.3. Theoretical color magnitude diagram (CMD) of stars in the SMIDGE SMC region. The CMD contains ~800,000 stars and is color-coded by stellar age. Color is plotted on the x-axis (bluer stars are on the left; redder on the right) and magnitude (brightness) on the y-axis (stellar brightness increases as magnitude decreases). The CMD can serve as a proxy for a temperature-luminosity plot (stellar surface temperature increases to the left; luminosity increases upward). Some prominent features on the CMD are, (1) the main sequence, stretching from the lower right to the upper left, where stars spend most of their lives while they undergo nuclear fusion in their cores, (2) the red giant branch (RGB) which is an almost vertical sequence rising from the main sequence, and (3) the red giant clump, or red clump (RC) which is an accumulation of stars midway up the RGB. This CMD was generated with the MATCH/fake synthetic CMD tool of Dolphin (2002).

plot is the Hertzsprung-Russel diagram which shows the relationship between stellar surface temperature and intrinsic luminosity). Figure 1.3 shows a theoretical CMD where brightness increases upwards and stars get redder (or cooler) to the right. The CMD is color-coded by stellar age (and not stellar color).

Stellar positions on a CMD and lifetimes in these positions are determined by a number of factors: the initial stellar mass, the age-metallicity relation and star formation history, the stellar evolution model specifying the initial stellar chemical composition (i.e., the fractional abundance of heavy elements), the distance to the stars ("distance modulus"), and any potential foreground Milky way dust extinction affecting the observations. For example, while undergoing hydrogen nuclear fusion in their cores, stars occupy a narrow diagonal feature on the CMD known as the main sequence. As stars evolve during their lifetimes, their size and luminosity can change drastically, and this would in turn change their location on the CMD. Their spectral type and ultimate fate (trajectory on the CMD) are by and large determined by their initial mass as they begin to fuse hydrogen.

Since stellar magnitude is indicative of the brightness of stars, a spread in the stellar distribution along the line of sight spreads the stars in magnitude. Dust extinction affects both the stellar color and magnitude on a CMD: the attenuation of starlight moves stars vertically (downward) in magnitude and redward in color, and features which would appear compact or narrow in the absence of dust tend to get spread out due to the amount and type of dust present. A CMD can contain both reddened and unreddened stars since, 1) it may be based on observations of a large enough region encompassing dusty and non-dusty parts of a galaxy, and 2) it is always based on observations of stars along the line of sight, therefore CMD features may experience changes in response to intervening dust (including foreground Milky Way dust) and to the variable structure of the ISM column density along the line of sight. It can be reasonably expected that the latter effect will impact similarly all stars on a CMD with a given color-magnitude combination along the same sightline since dust affects stars due to their physical location in space and not due to their location on the CMD; that is, along the same line

11

of sight reddened main sequence stars experience a similar displacement from their unreddened location on a CMD as, say, RGB stars.

A relative offset between the dust layer and the stars can create the appearance of additional CMD effects to those caused by the extinction of starlight. One can imagine a very simple geometry along the line of sight with a single thin layer of dust and a single thin layer of stars where the dust can be either in front of or behind the stars (reddening 100% or 0% of the stars). Figure 2.4 contains a visual presentation of the effect. In reality galactic geometry is often more complex and can be challenging to interpret depending on the galaxy's orientation in space: there can be multiple dust layers and multiple stellar layers, they can vary in thickness, and stars can be embedded in the dust layer or vice-versa. The strength of the effect on a CMD will depend on a number of factors, including the distance to the galaxy, the relative size/depth along the line of sight of the dust and star distributions, the amount of dust and the number of stars in the region (dust and stellar density), etc. If stars are embedded within the dust layer, they will experience differential reddening along the line of sight. If, on the other hand the dust is embedded within the stars, a fraction of stars will be reddened depending on the relative position of the stars and the dust.

The SMIDGE data, and in particular the bimodality of red giant branch stars, supports the hypothesis that within the SMIDGE field the dust is in a thin layer relative to the stars. If the dust and stars were well mixed, the stellar distribution would fully sample the extinction distribution and we would see a continuously reddened RGB, which is not what we observe. While most easily seen in the nearly vertical RGB, the bimodality should be present in other CMD features assuming they follow the same spatial distribution. Indeed, observing the CMD of the densest parts of the SMIDGE field in molecular cloud regions shows a bimodality in the main sequence as well. (The red clump must be bimodal as well, but since the unreddened RGB falls in the region between the unreddened and reddened red clump, it is difficult to observe this effect.)

Measuring the stellar displacement on a CMD along with an understanding of the

theoretical (unreddened and unaffected by galactic geometry) stellar location, therefore, can be used to study properties of the galactic structure and the dust extinction (Dalcanton et al., 2015). There is a complex relationship between SMC's elongation and proximity, where the distance distribution of SMC's stellar component along the line of sight can account for ~15% of the distance to the center of the SMC. Due to this effect, stars on the SMC CMD can experience appreciable displacement from a theoretical location which may have been predicted if the stars were all lying in a plane equidistant from the point of view of the observer, or equivalently, if the galaxy were located farther such that it would in effect appear flat.

It is therefore imperative that when CMDs are used to study SMC dust properties, the effects of galactic structure and dust extinction on the CMD are accounted for simultaneously, as in Chapter 2. Such considerations may be necessary when deriving dust extinction properties for any nearby galaxy whose stars may exhibit these potentially degenerate effects on a CMD. Otherwise one may conclude dust extinction which may not accurately represent actual dust grain properties, or galactic structure which may in fact be caused by dust extinction.

The approach taken in the SMC dust extinction analysis in Chapter 2 is to measure changes in the theoretical CMD location of stars. The focus is on red giant clump, or simply red clump (RC) stars, since the effect of dust extinction on this CMD population can be studied in a relatively straightforward way. RC stars have exhausted their hydrogen fuel, have thus moved away from the main sequence and into a helium-burning stage, and for ~10 Gyr reside in a tight clump on the CMD in the absence of dust, where the clump can be easily spotted in Fig. 1.3 (at $M475 - M814 \approx 1.3$ and $M475 \approx 20$). This property renders them very suitable as a distance indicator to objects within the Milky Way and nearby galaxies (Cannon, 1970; Girardi & Salaris, 2001; Bovy et al., 2014, also see Girardi (2016) and references therein). Measuring the observed elongation, or slope, of the clump toward fainter magnitudes and redder colors can theoretically be a straightforward way to infer the properties of dust which cause this displacement. If this displacement can be measured across photometric bands by examining CMDs with magnitudes ranging from UV to IR wavelengths (keeping the CMD color constant), the result will be a

measurement of the observed changes in starlight due to dust with wavelength. This would then directly result in the dust extinction curve (Nataf et al., 2013; De Marchi & Panagia, 2014; De Marchi et al., 2014, 2016).

The SMIDGE CMD shows features which hold a wealth of information about 3D galactic geometry properties and details about the extinction. This study begins with a simple model for the SMC red clump CMD built upon the theoretical CMD location of RC stars obtained from star formation history studies of a nearby region (Weisz et al., 2013). The model simulates a log-normal distribution of extinctions, A_V, sampled randomly by the stars, a distance distribution of stars along the line of sight, and a RC reddening vector slope which simulates R_V, or the extinction law. Several reasons for choosing a log-normal distribution are outlined by Dalcanton et al. (2015). Observations and simulations suggest that log normal probability density functions should be a ubiquitous feature of the turbulent interstellar medium (Hennebelle & Falgarone, 2012; Kainulainen et al., 2009; Hill et al., 2008).

This model enables exploring the relationship between the SMC dust extinction properties and the galactic depth along the line-of-sight which are known to affect the SMC CMD at the same time. The same approach is applied also to the LMC (located at ~50 kpc, at 1/2 solar metallicity, and also significantly extended along the line of sight) to disentangle the effects of dust extinction and galactic geometry in SMC's neighbor.

Chapter 3 expands upon work described in Chapter 2 to develop a more accurate model built on the CMD of red clump and red giant branch (RGB) stars. The goal is to model the 3D SMC geometry, the dust extinction, and also the star formation (SF) history of the SMIDGE region by leveraging information about the position, width, and effects of dust and geometry on the RGB in addition to these effects on the RC. The vertical CMD appearance of the RGB population enables the observation of SF, dust extinction and geometry effects which can not be inferred from the effects on the RC alone. For example, the RGB experiences an obvious bimodality on the SMIDGE CMD (see Fig. 2.2). This bimodality is believed to be a result of the structure of the ISM and the relative positions of the ISM and the centroid of the stellar

distribution. It suggests that the dust is in a thin layer relative to the distribution of stars which are either in front of or behind the dust from our point of view, and thus experience all of the dust column or none of it. If instead the dust and stars were mixed, the stars would sample the entire dust distribution and the RGB would be continuously reddened, but this is not what is observed. The doubling of the RGB can be used to infer the fraction of reddened stars in the SMIDGE field. A less obvious effect is the widening of the unreddened RGB (located blueward of its reddened counterpart). A close examination of the RGB width and a comparison to synthetic CMD models examining a range of star formation histories (SFHs) reflecting changes in the star formation rate and metallicity over time results in the ability to accurately model the range of SMIDGE metallicities.

Once the appropriate SMIDGE SFH is found by matching stellar number counts on the observed and modeled CMDs, this SFH is used to generate an unreddened theoretical CMD containing a synthetic population of stars which should accurately represent the SMIDGE region in the absence of dust extinction and galactic geometry. The approach is to build upon this model by incorporating a line of sight depth, the relative positions of the dust and the stars, a log-normal distribution of extinctions A_V with width σ_{A_V}, and a simulated observational noise. The latter reflects the inherent uncertainty in the precise positions of stars from HST observations due to the effects of stellar crowding. This sophisticated model allows for the simultaneous measurement of the distance distribution of the stellar component, the fraction of reddened stars behind the dust, and the mean and the width of the extinction distribution. The approach taken is to search through a grid of model CMDs simulated according to a range of values for each dust and geometry parameter, and find the closest fit to the observed SMIDGE CMD. This CMD matching technique has traditionally been used in SFHs studies (Tosi et al., 1989; Tolstoy & Saha, 1996; Harris & Zaritsky, 2001; Dolphin, 2002; Williams, 2002; Zaritsky & Harris, 2004; Cignoni et al., 2009; Weisz et al., 2014; Williams et al., 2017; Rubele et al., 2018), and here it is specifically used to constrain the dust extinction and geometry properties.

Chapter 4 is a summary and discusses future work. The dust extinction and 3D galactic

geometry parameters for the SMC Bar found in Chapter 3 can serve to refine the measurement of the average SMC extinction curve and to derive maps of the spatial variation in R_V and A_V. Since the galactic geometry parameters are not expected to vary across the SMIDGE field, they can be held fixed while the CMD is fit by varying the extinction curve, R_λ. A test can be performed to examine if the dust extinction distribution A_V and σ_{A_V} can also be held fixed if a minimum variation is expected in their values as well. This will allow for an independent non-parametrized extinction curve measurement which does not assume an existing form (as it does in the analysis in Chapter 3). The measurement will in effect again show changes in the slope of the red clump reddening vector on a CMD, but this time it will be done by CMD fitting with a pre-existing knowledge of values for geometry and extinction parameters which should allow for a refined R_λ measurement. It will be representative of the average curve in the SMC Bar since red clump stars are expected to be randomly distributed throughout the region.

Measuring the spatial variability of R_V across the SMIDGE region (which samples a variety of environments across the low-metallicity SMC) will result in the most comprehensive distribution of extinction curves in the SMC to date. We will then be much better informed about what "SMC-like" extinction truly means, and the environments in which the SMC extinction law can be applied. Fundamentally, it will illuminate the detailed properties of dust in high-redshift / low-metallicity galaxies and in turn perhaps enable a better understanding of the evolution of these properties, and the evolution of the Universe itself through astrophysical processes in which interstellar dust plays a role.

Chapter 2

The Small Magellanic Cloud Investigation of Dust and Gas Evolution: The Dust Extinction Curve from Red Clump Stars

Abstract of Chapter 2

We use *Hubble Space Telescope (HST)* observations of red clump stars taken as part of the Small Magellanic Cloud Investigation of Dust and Gas Evolution (SMIDGE) program to measure the average dust extinction curve in a ~200 pc $\times$ 100 pc region in the southwest bar of the Small Magellanic Cloud (SMC). The rich information provided by our 8-band ultra-violet through near-infrared photometry allows us to model the color-magnitude diagram of the red clump accounting for the extinction curve shape, a log-normal distribution of A_V, and the depth of the stellar distribution along the line of sight. We measure an extinction curve with $R_{475} = A_{475}/(A_{475} - A_{814}) = 2.65 \pm 0.11$. This measurement is significantly larger than the equivalent values of published Milky Way $R_V = 3.1$ ($R_{475} = 1.83$) and SMC Bar $R_V = 2.74$ ($R_{475} = 1.86$) extinction curves. Similar extinction curve offsets in the Large Magellanic Cloud (LMC) have been interpreted as the effect of large dust grains. We demonstrate that the line-of-sight depth of the SMC (and LMC) introduces an apparent "gray" contribution to the extinction curve inferred from the morphology of the red clump. We show that no gray dust component is needed to explain extinction curve measurements when a full-width half-max depth of 10 ± 2 kpc in the stellar distribution of the SMC (5 ± 1 kpc for the LMC) is considered, which agrees

with recent studies of Magellanic Cloud stellar structure. The results of our work demonstrate the power of broad-band HST imaging for simultaneously constraining dust and galactic structure outside the Milky Way.

Chapter 2 analyzes the average SMC dust extinction curve from color-magnitude diagrams (CMDs) of red clump star using a simple model for the SMC galactic depth along the line-of-sight. Chapter 3 attempts to simultaneously understand galactic geometry and dust extinction properties by incorporating red giant branch and red clump stars into an expanded CMD model. Chapter 4 contains a summary and describes future work on a refined measurement of the average SMC dust extinction curve using the galactic geometry and dust extinction properties derived in Chapter 3. It also describes an outline for deriving spatially resolved SMC dust extinction maps to understand the distribution of extinction curves in the low-metallicity environment of the SMC.

2.1 Introduction

Studying dust and its extinction is essential for our interpretation of the observational properties and evolution of galaxies. By examining dust extinction in the Small Magellanic Cloud, we can obtain a high-resolution picture of a low metallicity environment of $1/5 - 1/8\, Z_\odot$ (Dufour, 1984; Russell & Dopita, 1992; Kurt et al., 1999; Lee et al., 2005; Rolleston et al., 1999, 2003) at a distance of 62 kpc (Scowcroft et al., 2016). SMC-like extinction is widely used to correct for the effects of dust in low metallicity or high redshift galaxies (Noll & Pierini, 2005; Galliano et al., 2005; Cignoni et al., 2009; Glatt et al., 2008; Sabbi et al., 2009). Currently, however, there are only a handful of measurements of the extinction curve in the SMC.

Extinction curve measurements exist for only about ten individual SMC sight lines towards O and B stars derived from UV spectroscopy (Lequeux et al., 1982; Prevot et al., 1984; Gordon & Clayton, 1998; Gordon et al., 2003; Maíz Apellániz & Rubio, 2012). These few sight lines allow only low-number statistics of extinction and dust properties in the Small Magellanic

Cloud while they also tend to probe the vicinity of star-forming regions which may alter the dust grains in their surroundings due to the intense UV radiation fields. A more thorough appreciation of the extinction curve shape and its possible variations can be gained through large-scale multiwavelength studies which can reveal features difficult to reliably detect by observing a handful of individual stars (e.g. Schlafly et al., 2016). To fully understand dust extinction in a low-metallicity environment it is therefore critical to study the SMC on a wider scale to obtain a more representative sample of extinction curves.

It is immediately clear from existing SMC extinction curve measurements that SMC-like dust is distinct from Milky Way dust. Most extinction curves in the Milky Way (MW) are well-described by an empirical relationship based on one parameter, $R_V = A_V/E(B-V) = A_V/(A_B-A_V)$, representing the ratio of total to selective extinction at optical wavelengths (Cardelli et al., 1989) and serving as a proxy for the average dust grain size along a sight line. Curves outside the Galaxy show deviations from this relationship, including all measured curves to date in the SMC (Gordon et al., 2003; Cartledge et al., 2005; Maíz Apellániz & Rubio, 2012). Figure 1.1 shows that particular differences from MW-type dust extinction include a steeper far-UV rise and/or a weaker 2175 Å bump are evident near the 30 Doradus region in the Large Magellanic Cloud (LMC) (Clayton & Martin, 1985; Fitzpatrick, 1985) and in the star-forming bar of the SMC (Prevot et al., 1984).

The pair method (Trumpler, 1930; Massa et al., 1983; Cardelli et al., 1992) has produced the majority of extinction curves in the SMC. This method measures extinction as a function of wavelength by comparing the spectra of a reddened and an unreddened star of approximately the same spectral type. In addition to being limited to only a few lines of sight, the pair method requires high signal-to-noise ultraviolet spectroscopy which additionally places a strict limit on the brightness of stars which can be studied. Modifications to the pair method can be made to increase the efficiency of the technique. These include using photometric measurements instead of spectroscopy and using theoretical predictions for the star's color and magnitude rather than a specific matched comparison star. In this study we use the latter approach and produce

color-magnitude diagrams (CMDs) for thousands of stars allowing us to simultaneously measure the stars' displacement due to dust from a known unreddened location. Measuring this effect, which is evident across photometric bands ranging in wavelength from ultraviolet to infrared, allows us to determine the extinction curve shape.

To measure a star's displacement in CMD space due to dust extinction, we must have an idea of its initial location. The red giant clump, or red clump (RC), population is an ideal target for such techniques due to the narrow intrinsic distribution of the stars in CMD space (Girardi & Salaris, 2001; Girardi, 2016). RC stars are mostly low-mass 1-12 Gyr K giants in their He-burning phase found at the red end of the horizontal branch occupying a compact region on a CMD. Due to variable reddening by dust, the RC appears as an extended sequence stretching toward fainter magnitudes and redder colors from the unreddened RC location. By measuring the vertical displacement of the reddened RC feature, it is possible to find the dust extinction in magnitudes, A_λ. From the slope of the reddened RC, one can also measure the value of the ratio of the absolute to selective extinction, $R_\lambda = A_\lambda/(A_{\lambda'} - A_{\lambda''})$, where $A_{\lambda'} - A_{\lambda''}$ is the extinction in a chosen color combination. The selective extinction is traditionally measured in B and V filters (at 4405 Å and 5470 Å) giving $A_B - A_V = E(B-V)$ and a corresponding $R_V = A_V/E(B-V)$. This technique can be applied with a variety of different color combinations to study the extinction curve shape. The application of the red clump method to measure extinction has been used in the Milky Way (Nataf et al., 2013) and the LMC (De Marchi et al., 2014; De Marchi & Panagia, 2014; De Marchi et al., 2016). Some of these previous studies have led to unexpected results. De Marchi et al. (2014) first present the red clump method (subsequently employed by De Marchi & Panagia (2014) and De Marchi et al. (2016)) to study the shape of the extinction curve using multi-band photometry in LMC's Tarantula Nebula. They find R_V values of 5.6 ± 0.3 and 4.5 ± 0.2 for R136 and 30 Doradus, respectively, indicating curves with a steeper optical reddening vector than the diffuse Galactic interstellar medium (ISM) of $R_V = 3.1$ (Cardelli et al., 1989) and LMC's average of $R_V = 3.4$ (Gordon et al., 2003). The authors attribute this result to the presence of "gray" extinction (i.e. extinction with small changes in color). "Gray" UV/optical extinction

curves with high values of R are attributed to the presence of large dust grains (Strom et al., 1971; Dunkin & Crawford, 1998). Indeed, high $R_V \sim 5.5$ is observed in the dense Galactic ISM, where dust grain growth is thought to have occurred (Cardelli et al., 1989; Weingartner & Draine, 2001). De Marchi & Panagia (2014) and De Marchi et al. (2016) argue that the observed LMC extinction curve with high R_V is indicative of large grains injected into the ISM by recent Type II supernova explosions.

Here we present the results of a study using *Hubble Space Telescope (HST)* multi-band observations of the SMC to characterize the average extinction curve at a range of wavelengths and over a large region of the galaxy. Our survey, named the Small Magellanic Cloud Investigation of Dust and Gas Evolution (SMIDGE), focuses on a 100 pc $\times$ 200 pc region in the southwest bar of the SMC with observations spanning the ultraviolet (UV) to near-infrared (NIR) wavelength range. Similarly to the work of De Marchi et al. (2016), we perform an analysis of HST observations of the 30 Doradus region in the LMC. In addition to De Marchi et al. (2016)'s study, we also aim to explain how the SMC's and the LMC's depth along the line of sight impacts the extinction curve shape in the region. We present the SMIDGE data in Section 2.2. In Section 2.3 we give details about how the extinction curve can be measured from red clump stars and present a model of how the depth along the line of sight of the SMC impacts extinction curves measurements. In Section 2.4 we quantify the effect of the SMC and LMC depth along the line of sight on existing observed and model extinction curves, and test the agreement between the latter and the newly-derived extinction curves. We then compare our results to other extinction curve measurements. In Section 3.5 we discuss the significance of our results for the extinction curve shape in the SMC and we conclude in Section 2.6.

2.2 Data

We use imaging obtained by the SMIDGE survey (GO 13659) covering an area of ~200 pc $\times$ 100 pc in the southwest bar region of the Small Magellanic Cloud. The location of the
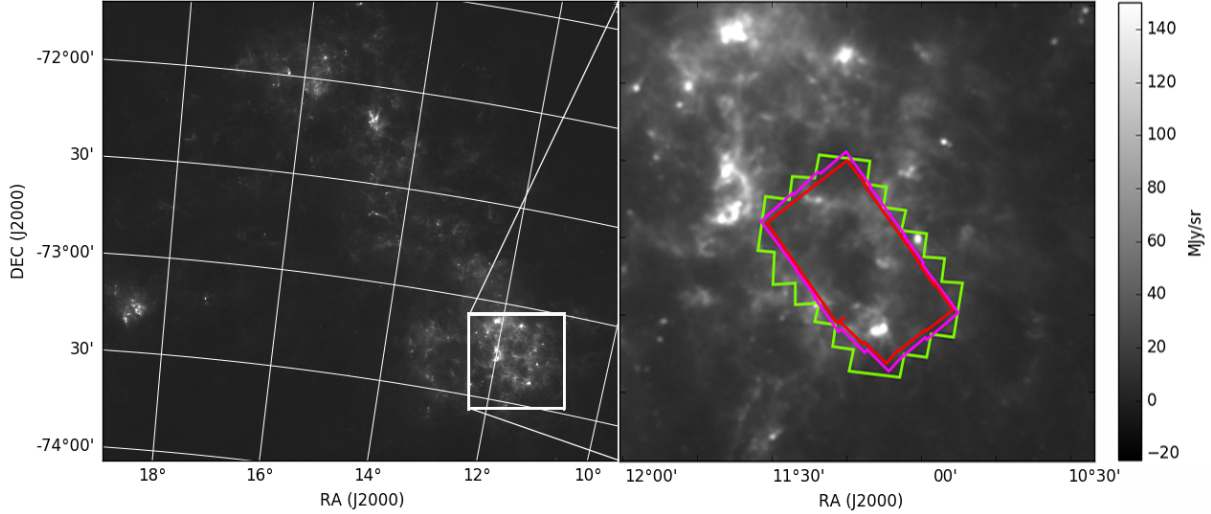
Figure 2.1. Location of the SMIDGE region in the southwest bar of the Small Magellanic Cloud superimposed on a Herschel 250 μm map. The imaging footprint of *Hubble Space Telescope's* cameras are shown in green (ACS/WFC), magenta (WFC3/UVIS), and red (WFC3/IR).

imaging footprint is displayed in Figure 2.1. The data were obtained by the *Hubble Space Telescope's* Advanced Camera for Surveys (ACS) Wide Field Camera (WFC), and the Wide Field Camera 3 (WFC3) instrument's infrared (IR) and ultraviolet-optical (UVIS) imagers. The following broad-band filters were used, covering the wavelength range 0.24 - 1.5 μm: *F225W*, *F275W* and *F336W* from *WFC3/UVIS*; *F475W*, *F550M*, *F658N*, and *F814W* from *ACS/WFC*; and *F110W* and *F160W* from *WFC3/IR*. We omit the *H*α narrow-band filter *F658N* for the purposes of this study.

We perform PSF-fitting photometry using the DOLPHOT package, an updated version of HSTPHOT (Dolphin, 2000). We follow analysis procedures similar to those used by the Panchromatic Hubble Andromeda Treasury (PHAT) survey, as described by Williams et al. (2014). Namely, we follow the same methodologies and processing code for image alignment, cosmic ray and artifact rejection, and DOLPHOT execution. SMIDGE processing differs in a number of ways: we use a `TinyTim`-based PSF library, photometer full-depth stacks of all images simultaneously, and improve image distortion corrections. Complete details about the survey's observations, reduction, data quality, and catalog presentation will be outlined in the

Table 2.1. SMIDGE data quality cuts

Camera	Sharpness	Crowding
UVIS	0.15	1.3
ACS	0.2	2.25
IR	0.15	2.25

Note. — For details see Section 2.3 of Williams et al. (2014).

Table 2.2. SMC Red Clump Properties

Filter	Theoretical RC_{Mag}	σ_{Mag}
F225W	23.22	0.21
F275W	21.83	0.15
F336W	20.32	0.11
F475W	19.78	0.09
F550W	19.22	0.09
F814W	18.40	0.09
F110W	17.96	0.09
F160W	17.44	0.09

Note. — Unreddened red clump location from synthetic CMD. The mean $F475W - F814W$ color for all photometric bands is 1.38 ± 0.059. This includes MW foreground reddening toward the SMC of A_V=0.18 and R_V=3.1, and a distance modulus of 18.96.

upcoming SMIDGE survey paper (Sandstrom et al., in preparation).

We have made a number of culls on the photometry catalogs to eliminate low-quality measurements and obtain color-magnitude diagrams (CMDs) with well-defined features. Table 2.1 lists the sharpness and crowding culling values we have used to obtain `gst` catalogs. We plot the CMDs for the SMIDGE survey in Figure 2.2. We note that a red leak in *HST's WFC3/UV F225W* affects our photometry of the red clump. This is only an issue for the UV-faint red clump stars in *F225W* where the red leak can cause a significant offset in the photometry. Although we present the derived values of the reddening vector for *F225W*, we suggest caution in interpreting these values.

To analyze the extinction curve in the 30 Doradus region in the Large Magellanic Cloud, we use data from the Hubble Tarantula Treasury Project (HTTP) survey. The survey data, described in Section 2 of Sabbi et al. (2016), encompasses ultraviolet to infrared wavelengths
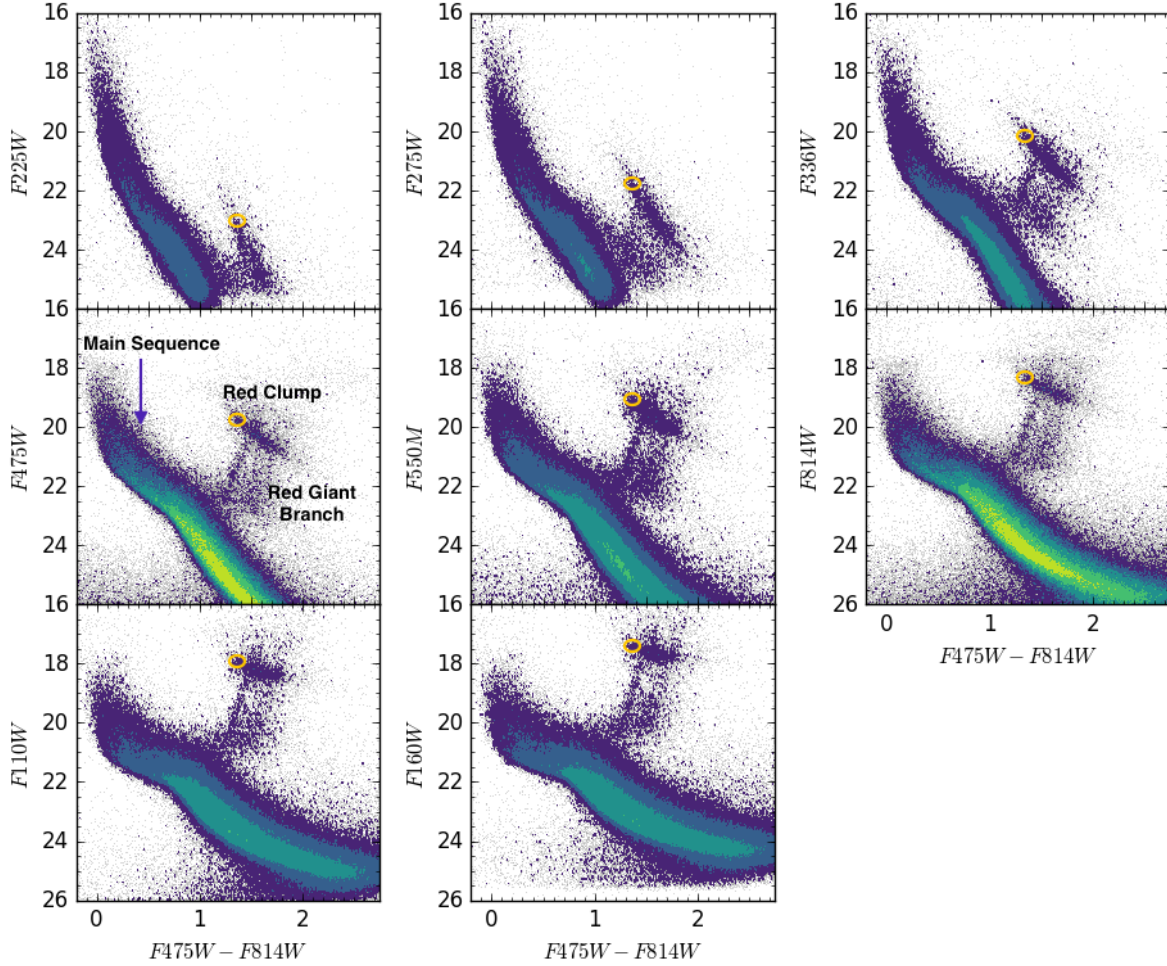
Figure 2.2. Color-magnitude diagrams (CMDs) for the eight SMIDGE photometric bands plotted in the optical $F475W - F814W$ color after applying the culling values in Table 2.1. Stellar density contours range from 2 to 1200 stars decimag^{-2}. The main features are shown in $F475W$'s CMD. The red clump population is seen as a streak above and somewhat parallel to the main sequence where the orange ellipse indicates its theoretical unreddened location determined as described in Sec. 2.3.2 with values listed in Table 2.2. The red giant branch can be distinguished by its bimodal appearance rising almost vertically between the main sequence and the red clump. Both the extended red clump streak and the doubled red giant branch are consequences of dust extinction.
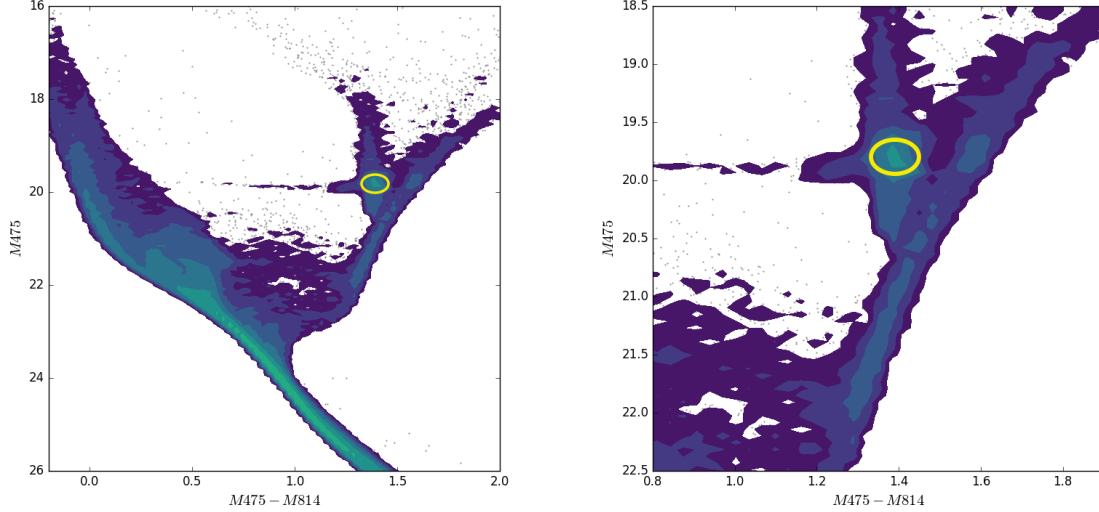
Figure 2.3. *F475W* synthetic CMD with the unreddened red clump location indicated by the yellow ellipse in both panels. The contours are logarithmic in number of stars per decimag. The selection of the unreddened red clump is based on parameters specific to the Small Magellanic Cloud as explained in Sec. 2.3.2. For clarity, the width and height of the ellipse represent twice the size of the unreddened red clump intrinsic spread in color and magnitude. Synthetic CMDs for the rest of the SMIDGE filters are plotted in the Appendix.

and is obtained by the *Hubble Space Telescope's* ACS and WFC3 instruments in the set of *HST's F275W, F336W, F555W, F658N, F775A, F775U, F110W*, and *F160W* filters, where *F775A* is ACS/WFC *F775W*, and *F775U* is WFC3/UVIS *F775W*. We choose the ACS/WFC *F775W* filter due to the larger number of sources in this passband, and we omit the narrow-band filter *F658N* as we do for the SMIDGE extinction curve analysis. Further survey details about the observations, data reduction and quality, and catalog presentation are discussed in Sabbi et al. (2016).

2.3 Extinction from Red Clump Stars

2.3.1 Overview

The reddened red clump is prominently visible in the SMIDGE CMDs. Figure 2.2 shows the CMDs of the spatially resolved stars in SMIDGE's eight *HST* photometric bands
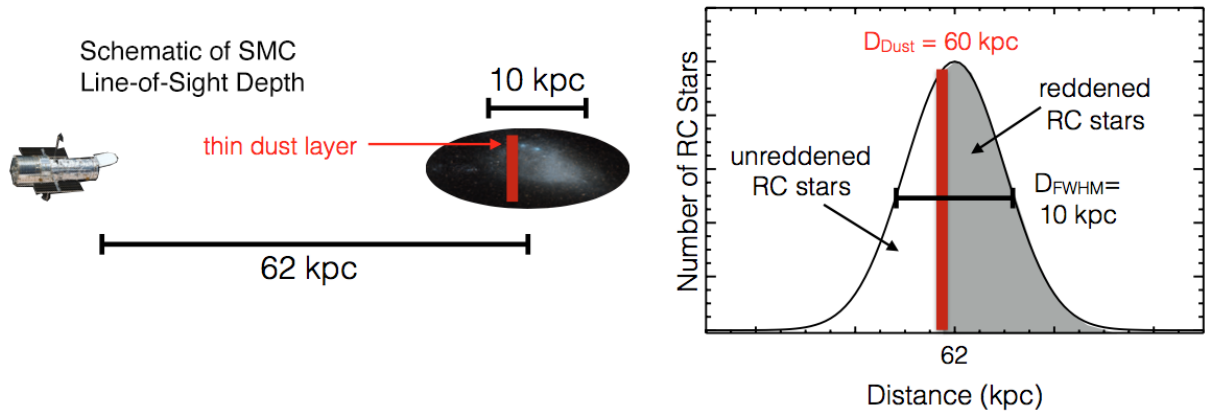
Figure 2.4. Example of the stellar and dust distribution in our model with parameters correspond-ing to the example in Figure 2.5. The bimodality of the red giant branch leads us to conclude that the dust is located in a thin layer relative to the stars leading to either unreddened or reddened red clump stars (see Sec.2.3.3).

using optical $F475W - F814W$ color chosen for its best signal-to-noise ratio. In the absence of dust, the RC would be seen as a compact feature on the CMD at the red end of the horizontal branch and blueward of the red giant branch (RGB). Due to variable extinction by dust, however, SMIDGE observations reveal a RC which appears as a streak above and almost parallel to the main sequence (MS) with a tail extending towards redder colors and fainter magnitudes. Since the effects of dust are great compared to the photometric uncertainty of the RC, the feature can be easily studied. To measure the extinction and extract the extinction curve slope, we measure the slope of the reddened red clump streak in each CMD. The measurement requires carefully defining an unreddened RC color and magnitude which we discuss in the next section.

Another prominent feature in the SMIDGE CMDs is the bimodal red giant branch (RGB). The RGB would theoretically appear as a narrow and almost vertical sequence just redward of the RC. Due to dust, however, the RGB assumes a bimodal distribution and this bimodality allows us to infer that the dust is in a thin layer relative to the stars. If the dust and stars were well mixed, the stellar distribution would fully sample the extinction distribution and we would see a continuously reddened RGB, which is not what we observe. Assuming the RC and RGB stars follow the same spatial distribution, we can infer that same bimodality should be present for
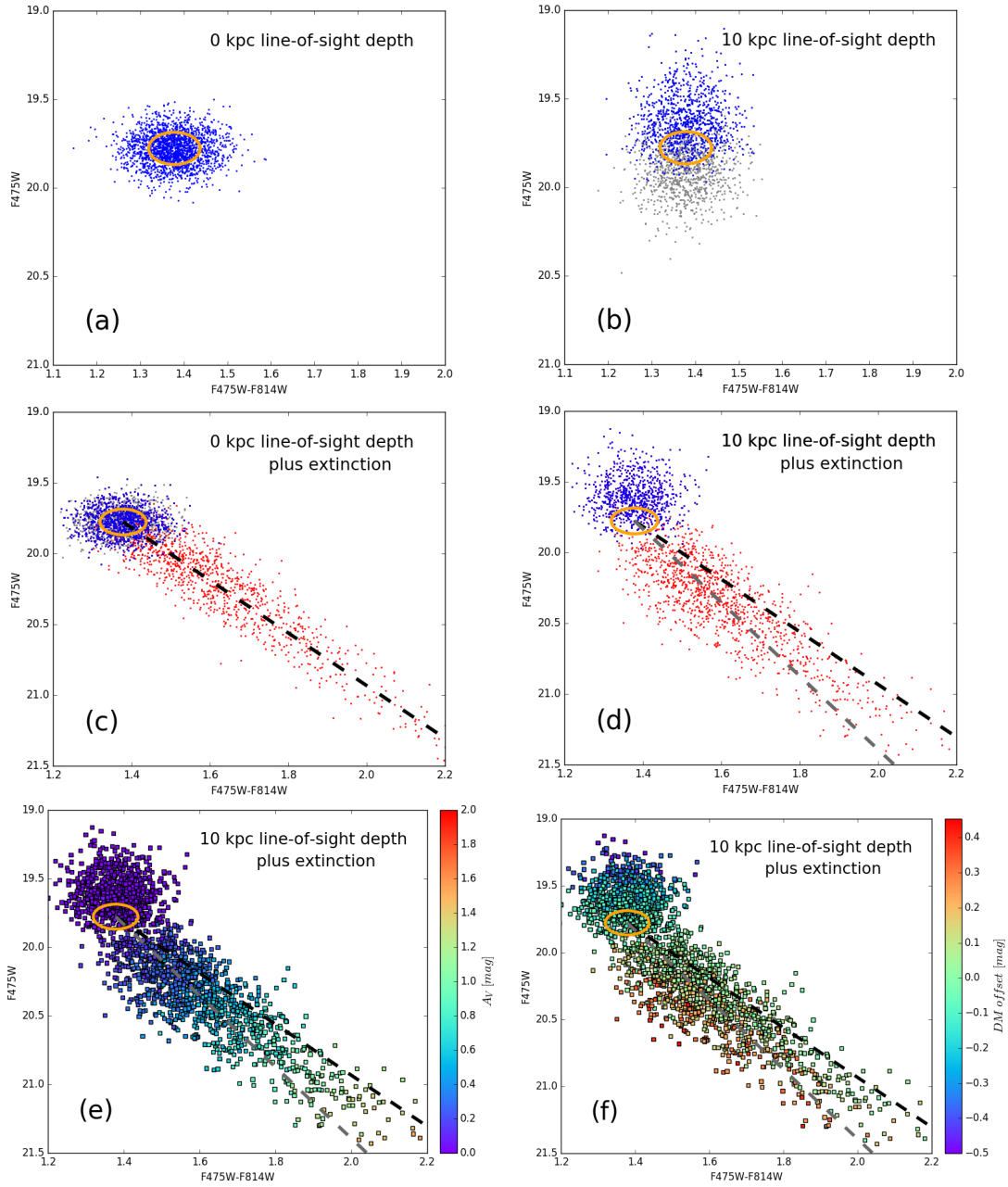
Figure 2.5. A 2000-star red clump (RC) model simulating the SMC line-of-sight depth. (a) and (b) show a simulated RC population at a mean distance of 62 kpc, unaffected by dust extinction and subject to depths of 0 & 10 kpc. Due to the elongated galactic shape (see Fig. 2.4), stars have varying distances seen as a spread in magnitude in (b), with stars closer in blue. The orange ellipse shows the theoretical RC unreddened location (Table 2.2). (c) and (d) show models with depth of 0 & 10 kpc. Unreddened foreground stars are in blue. Stars in red are reddened with a V-band log-normal distribution of extinctions with a median $A_V = 0.4$ mag (width $\sigma_{A_V} = 0.3$), a dust distance of 60 kpc, and a 0.65 reddened fraction. (e) and (d) are models with a 10-kpc depth. Stars are color-coded by A_V and distance offset. R_{in} (black dashed line) shows the input reddening vector slope. R_{out} in gray dashed traces the slope of the reddened RC with a 10 kpc line-of-sight depth as recovered from the model. At zero-depth, the extinction vector follows R_{in}. At a 10-kpc depth, the vector steepens since the reddened stars are further away and are fainter.

Table 2.3. LMC Red Clump Properties

Filter	Theoretical RC_{Mag}	σ_{Mag}
F275W	22.20	0.12
F336W	20.34	0.12
F555W	19.16	0.08
F775W	18.21	0.08
F110W	17.72	0.10
F160W	17.15	0.10

Note. — Unreddened LMC 30 Dor red clump location from Girardi & Salaris (2001) and De Marchi et al. (2016, DM16) with a corresponding 1 σ spread. MW foreground reddening of $E(B-V) = 0.07$ ($A_V = 0.22$) has been applied. The adopted $F555W - F775W$ color for all photometric bands is 0.97 ± 0.12.

the RC[1] (i.e. a foreground unreddened population and a background reddened population). Since there are no regions in the SMIDGE field which are free from dust, we have no unreddened red clump reference from our data. To accurately measure the extinction curve shape, we therefore need to rely on a model (described in the rest of Sec. 2.3) for the RC and the reddening it experiences.

2.3.2 A Model for the Unreddened Red Clump

We construct a model for the red clump as a two-dimensional Gaussian distribution of stars in color and magnitude. The key parameters which will set the model unreddened red clump (zero-point and widths in color and magnitude) are: age, metallicity and star formation history (SFH), average distance modulus, foreground reddening and SMC depth along the line of sight. We define the red clump unreddened zero point and width by using a SFH incorporating the full ranges of ages and metallicities appropriate for the SMIDGE region. This is an improvement upon previous works using this method which use single age and metallicity (e.g. De Marchi et al. (2014), De Marchi & Panagia (2014), and De Marchi et al. (2016)). We create a simulated CMD with foreground Milky Way extinction of $A_V = 0.18$ (derived from the Milky Way HI foreground towards the SMIDGE field; Muller et al., 2003; Welty et al., 2012) and $R_V = 3.1$, zero

---

[1]Note the unreddened RGB falls in the region between the unreddened and reddened red clump, making it difficult to observe this bimodality.
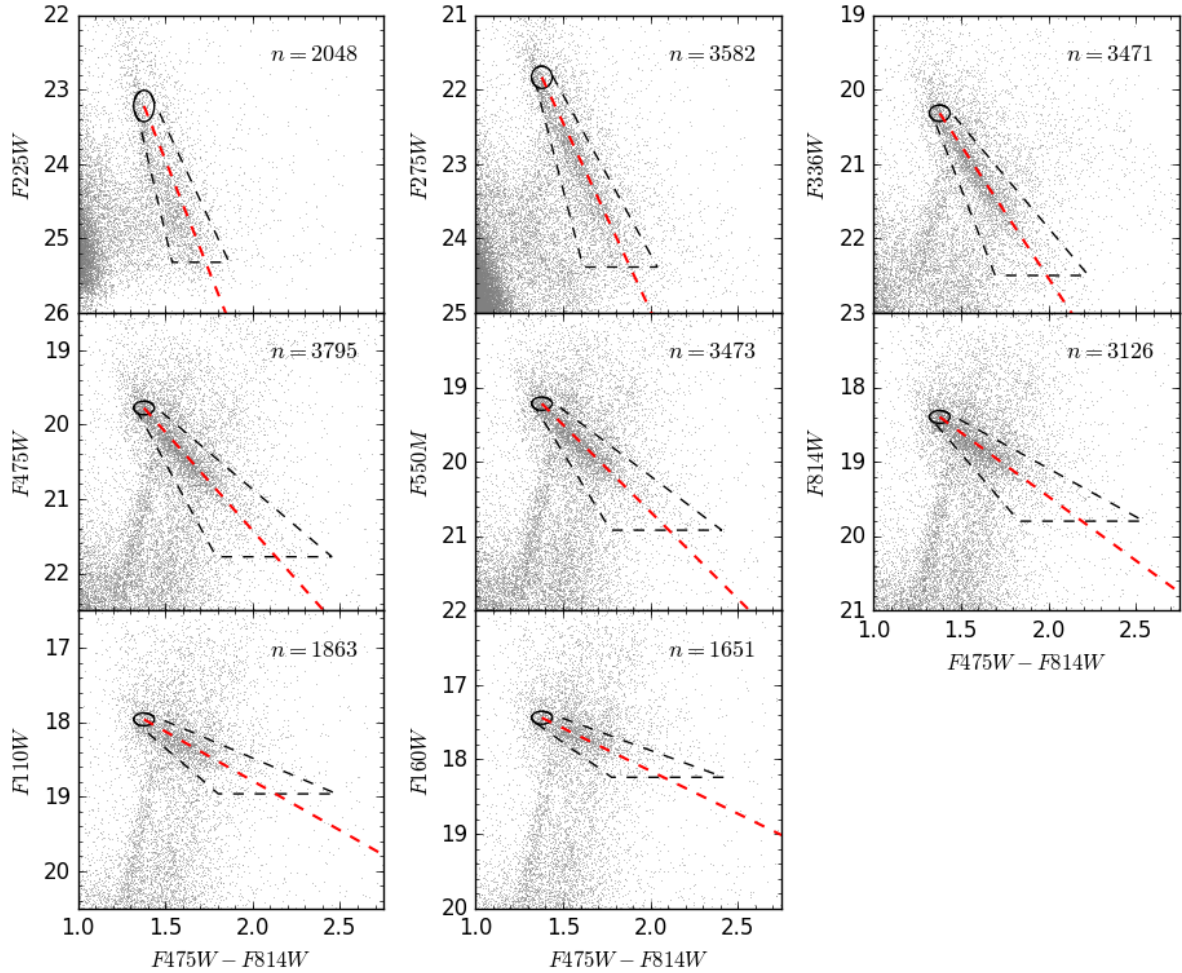
Figure 2.6. Selecting reddened red clump stars from SMIDGE color-magnitude diagrams with a focus on the red clump. The cone-shaped selection region is shown bound by the black dashed line. The unreddened red clump appropriate to the Small Magellanic Cloud (see Section 2.3.2) is indicated by the black ellipse. The size of the ellipse represents the intrinsic spread in color and magnitude of the theoretical red clump location due to the age range and metallicity of SMC red clump stars. The red dashed line represents the calculated reddening vector obtained as described in Section 2.3.4 with values given in Table 2.4. The size of the cone is determined by the approximate slope of the reddening vector with outer boundaries obtained by multiplying this slope by a factor of 1.4 in either direction (See Sections 2.3.4 and Appendix A). The number of sources within the selected reddened red clump region is indicated by n for each photometric band.
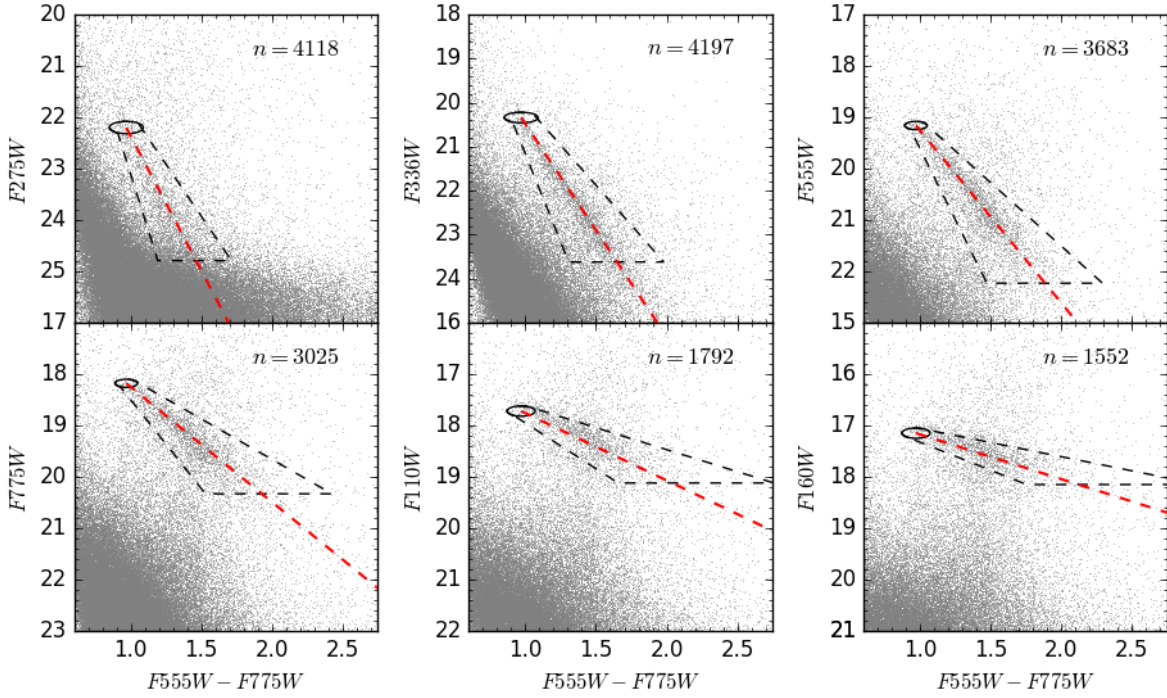
Figure 2.7. LMC 30 Dor CMDs from the HTTP survey with a focus on the red clump. See Figure 2.6 for a detailed description of the features on the CMDs.

line-of-sight depth, a distance modulus of 18.96 (Scowcroft et al., 2016), and a SFH based on Weisz et al. (2013), shown in Figure 2.3. Weisz et al. (2013) modeled the CMD of a nearby region in the SMC with similar RGB stellar surface density and with low internal dust attenuation based on deep *HST* photometry. Older populations dominating the RC are well mixed spatially and we expect no significant difference between the Weisz et al. (2013) field and SMIDGE, except for young ages (<200 Myr). We use a simplified approximation of the SFH and age-metallicity relation (AMR) where we adopt a smooth star formation rate (SFR(t)), with SFR enhancements at 500 Myr and 1.5-3.0 Gyr and similar Z(t) but offset to lower values by 0.2-0.3 dex. We compare the SMC SFH and AMR of Rubele et al. (2015) and Weisz et al. (2013) and find good consistency between the RC properties obtained from our model and from the Rubele et al. (2015) results (where higher metallicity, but lower A_V and older dominant RC ages compensate). We use the `fake` CMD simulation tool (part of the `MATCH` software package; Dolphin, 2002) to produce the unreddened RC model, adopting the PARSEC stellar evolution models (Bressan

et al., 2012; Tang et al., 2014; Chen et al., 2015) and a Kroupa (2001) initial mass function. The match between the observed location of the unreddened RGB in SMIDGE and the synthetic RGB give us confidence in the modeled CMD. The above model allows us to account for a potentially complicated red clump morphology such as, for example, a secondary red clump composed of younger stars extending toward fainter magnitudes.

We create synthetic CMDs for all $F475W - F814W$ color-magnitude combinations. The resulting $F475W$ CMD is plotted in Figure 2.3, and the rest of the color-magnitude combinations are plotted in Figure 2.12 in the Appendix. We model the position of the unreddened red clump using the full stellar population in the area, which includes red clump stars with a mean age of 1.81 ± 0.95 Gyr and a mean metallicity [M/H] $= -0.95 \pm 0.14$ where the uncertainty represents one standard deviation from the mean. We select red clump stars in $F475W - F814W$ matched across all eight CMDs by defining a wide box around the overdensity blueward of the red giant branch from which we pick objects which fall within a density contour encompassing 70% of the total number of sources in the box. This subsample of stars has a mean age of 2.02 ± 0.66 Gyr and an average [M/H] $= -0.90 \pm 0.11$. We use the 70 percentile contour to define a mean and a standard deviation for the red clump which is represented by the yellow ellipse in Figure 2.3. The ellipse center is defined by measuring the centroid of the color and magnitude in the subsample in each model CMD where the width and height of the ellipse indicate the standard deviation in color and magnitude respectively due to the intrinsic age and metallicity spread of the RC (Table 2.2). This ellipse is then used to designate the theoretical unreddened red clump location in the observed CMDs. In the Appendix we examine the effects of moderate variations in the zero point and in the width of the unreddened model RC. Effects from line-of-sight binaries are negligible due to the brightness of the RC giant primary stars. We additionally use artificial star tests to determine that the photometric error is small and therefore also negligible.

The theoretical location of the unreddened red clump population is dependent on the distance to the galaxy. We adopt an average SMC distance modulus of $\mu_0 = 18.96$ mag (62 kpc) from Scowcroft et al. (2016). We test the sensitivity of our results to the assumed distance

modulus in the Appendix since there is a well-known systematic distance variation as a function of position across the SMC. This variation is demonstrated by observations of Cepheid and RR Lyrae variables, supergiants, red clump stars, or a combination of these populations (Florsch et al., 1981; Caldwell & Coulson, 1986; Welch et al., 1987; Hatzidimitriou & Hawkins, 1989; Gardiner & Hawkins, 1991; Gardiner & Hatzidimitriou, 1992; Subramanian & Subramaniam, 2009, 2012; Haschke et al., 2012; Kapakos & Hatzidimitriou, 2012; Nidever et al., 2013; Scowcroft et al., 2016; Jacyszyn-Dobrzeniecka et al., 2016, 2017; Subramanian et al., 2017). Several of these studies conclude that the galaxy is elongated along an axis approximately along our line of sight with a 10-kpc full-width-half-maximum (FWHM) of the stellar density distribution (Gardiner & Hawkins, 1991; Gardiner & Hatzidimitriou, 1992; Nidever et al., 2013; Jacyszyn-Dobrzeniecka et al., 2016; Subramanian et al., 2017). Since we extend our analysis to the Large Magellanic Cloud, we note that an LMC line-of-sight depth would similarly impact extinction curve results. For the LMC Jacyszyn-Dobrzeniecka et al. (2016) conclude a FWHM distribution along the line of sight of about 5 kpc, where the LMC distance is ~50 kpc ($\mu_0 = 18.48 \pm 0.04$ mag) (Monson et al., 2012). For both the Small and the Large Magellanic Clouds this means that stars will have distances which vary significantly relative to the distance of the center of the galaxy itself as illustrated in the left panel of Fig. 2.4. This effect will inevitably be reflected on a color-magnitude diagram by creating a spread in the magnitude of stars.

2.3.3 Modeling the Reddened Red Clump

The line of sight depth of the SMC and the extinction the stars experience from the thin dust layer lead to an important effect: the unreddened red clump stars are closer (and therefore brighter) than the reddened red clump stars. An illustration of the model is given in the right panel of Figure 2.4. To account for all contributions to the extinction curve shape, we show the combined effect of line-of-sight depth and extinction by including a thin dust layer in our model of the red clump. We begin with a population of red clump stars positioned at the theoretical CMD red clump location described in Sec. 2.3.2. We then assume the stars have a Gaussian

distance distribution with a mean of 62 kpc average SMC distance (Scowcroft et al., 2016). In generating the model reddened red clump, we convolve the initial Gaussian distribution of magnitudes for the stars with this assumed Gaussian distance distribution. As discussed in Sec. 2.3.1, we see a clear separation between the reddened and the unreddened red giant branch, and we can thus assume that we can neglect the dust layer's depth along the line of sight since it is negligible compared to the depth of the distribution of the stars. The dust in our model is thus positioned in front of a fraction of the red clump population which we set at 0.65. Since this reddened fraction varies with the position of the dust relative to the stars, it is ultimately a function of the geometry of the region. Varying the fraction between 0.65 and 0.35 steepens the red clump slope by 0.1 - 0.2 across photometric bands ranging from F160W to F225W respectively. In a future study we plan to explore the way in which the relative geometry of the dust and stars affects the full synthetic CMD rather than only this simplified model of the red clump.

The model assumes the dust extinction experienced by the stars behind the screen has a log-normal column density distribution of A_V sampled randomly by the stars. There are several reasons for choosing a log-normal distribution (see Dalcanton et al., 2015). Observations and simulations suggest that log normal probability density functions should be a ubiquitous feature of the turbulent interstellar medium (Hennebelle & Falgarone, 2012; Kainulainen et al., 2009; Hill et al., 2008).

Our model employs the following parameters: $\langle D \rangle$ is the mean distance to the galaxy, D_{FWHM} is the FWHM line of sight depth of the galaxy, the dust layer is located at a distance D_{dust}, the stars experience a mean extinction $\langle A_V \rangle$ where the width of the log-normal distribution of extinctions is $\langle \sigma_{A_V} \rangle$. The input extinction curve slope which corresponds to the slope of the reddening vector is R_{in}.

To illustrate the effect of the line of sight depth on the measured extinction curve, we generate synthetic red clump datasets using this model with an input extinction curve slope and a line-of-sight depth as in Figure 2.5. It is clear in panels c) and d) in the figure that the line of sight

depth causes a steepening of the reddening vector. This results from the fact that the reddened stars are more distant and therefore fainter than the unreddened stars. Panels (e) and (f) of Figure 2.5 show the distance modulus offset and A_V for each of the stars in the 10-kpc line-of-sight depth model depicted in panel (d). The result of the Gaussian distribution of distance moduli and the log-normal distribution of A_V is that for even the highest A_V stars there is a range of distance moduli which, due to the Gaussian nature of the distribution, is weighted towards smaller offsets. The slope of the reddened RC is determined by the mean of this combined distribution. We also note that the theoretical, zero-depth red clump ellipse is at fainter magnitudes than the observed unreddened red clump. The reason for this is that the unreddened foreground RC population is closer. Nidever et al. (2013), Girardi (2016), and Subramanian et al. (2017) suggest the effect of an extended RC seen in color-magnitude diagrams can be attributed to the large line-of-sight depth rather than to population effects.

2.3.4 Measuring the Red Clump Reddening Vector Slope

To extract the extinction curve shape from the observed color-magnitude diagrams we need to determine the slope of the vector along which the red clump is extended from its theoretical unreddened location. Figure 2.6 illustrates our technique. To find the slope of the reddening vector using the method described below we need to first select the stars which will be used in the calculation since the extended red clump is not completely isolated on the CMDs but blends into other features. We select red clump stars by placing a boundary around these sources. First, we define a generous selection box surrounding the reddened red clump streak. We then find the approximate slope of the reddened red clump by fitting a linear slope to the points inside this region using the bisector of two lines found with the ordinary least squares method (Isobe et al., 1990). To refine this value, we then narrow the selection region by defining upper and lower boundaries set by the width of the ellipse representing the unreddened red clump and tangents to this ellipse whose slope is plus or minus 40% of the approximate slope. The bottom bound is set where the number density of sources in a region spanning one tenth of a magnitude
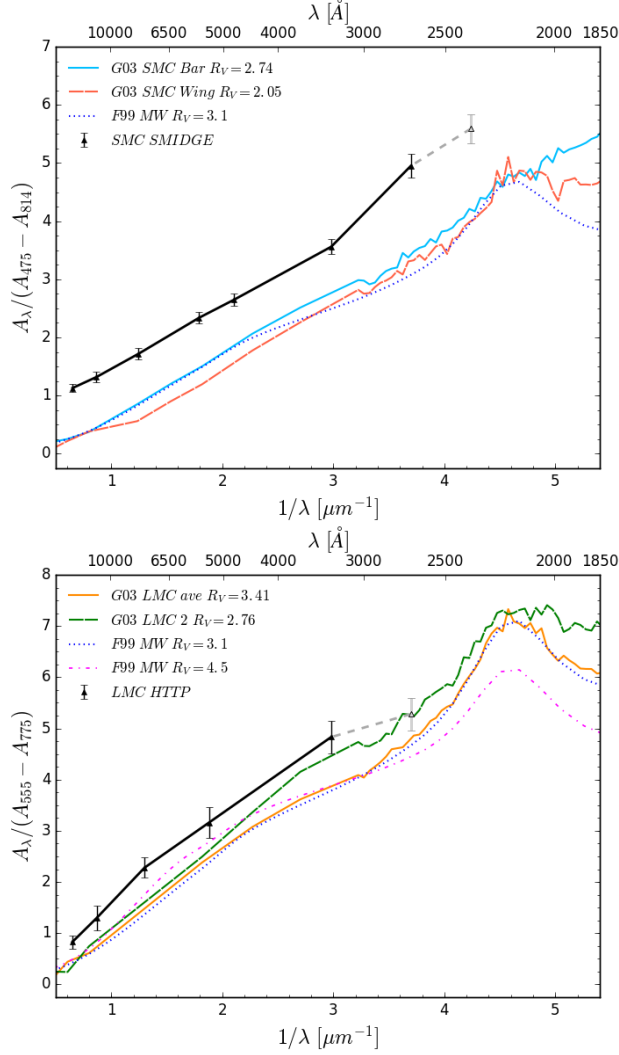
Figure 2.8. Top: The SMC SMIDGE extinction curve is plotted in black. For comparison, the Gordon et al. (2003, G03) SMC Bar and SMC Wing curves, and the Fitzpatrick (1999, F99) Milky Way $R_V = 3.1$ curves normalized to SMIDGE wavelengths are shown as well. On the bottom is the 30 Dor LMC extinction curve. The LMC average and LMC 2 Gordon et al. (2003) curves, and the Fitzpatrick (1999) Milky Way $R_V = 3.1$ and $R_V = 4.5$ curves are plotted as well. We conclude that the observed offsets in both the SMC and the LMC curves (the latter also noted by De Marchi et al. (2016, DM16)) are a result of the significant depth along the line of sight of both galaxies (see Sec. 2.3.2).

falls below 20 sources. We have investigated the effects of these boundary choices on the output slope by performing a series of sensitivity tests as described in the Appendix.

To determine the reddening, which is canonically given by $E(B-V) = A_B - A_V$, we choose *HST's* optical *F475W* and *F814W* to obtain $E(F475W - F814W)$ resulting in $R_\lambda = A_\lambda/(A_{475} - A_{814})$. *F475W* and *F814W* have effective wavelengths of 474.7 nm and 802.4 nm and are closely related to the SDSS g' and Johnson-Cousins *I* filters with effective wavelengths of 477 nm and 806 nm respectively (Dressel, 2014). We thus approximately obtain $R_{g I} = A_\lambda / E(g' - I)$.

The boundaries are determined independently for each combination of magnitude and *F475W - F814W* color. Although some of the reddened sources may come from the RGB instead of strictly from the RC (see Figure 2.3), since they are reddened due to dust along the same vector as RC stars are, they do not interfere with our slope measurement. We tested alternative ways to set the bounds of the RC selection, such as defining a wider or a narrower region around the apparent RC feature, extending the top and bottom bounds, or shortening the bottom bound. These variations and the results they produce are explored further in the Appendix, but they do not alter the results in addition to the reported uncertainties.

To measure the slope of the reddening vector using the refined selection of stars, we again use the bisector of the two ordinary least squares lines. The result is the ratio of the extinction in magnitudes (absolute extinction) to that in color (selective extinction), or R_λ. The values of this vector for the range of wavelengths explored by SMIDGE produce the extinction curve itself.

Uncertainties on calculating R_λ using our method result from a combination of factors. One source of error results from the intrinsic spread of the unreddened red clump population caused by the range of ages and metallicities attributed to the clump. Another is due to the scatter in the red clump distribution affecting the fit of the ordinary least squares bisector line to the red clump reddening vector. Since the RC becomes almost vertical in *F225W*'s CMD, it becomes difficult to measure the slope of the reddening vector in this filter resulting in another source of error. All these are taken into account and are used to report the uncertainty in our results. The photometric error for these bright sources as determined using artificial star tests is small and

Table 2.4. SMC SMIDGE Extinction Curve Results

λ [Å]	λ^{-1} [μm]	Band Combination	R_λ
2359	4.24	$A_{225}/(A_{475}-A_{814})$	5.59 ± 0.23
2704	3.70	$A_{275}/(A_{475}-A_{814})$	4.95 ± 0.19
3355	2.98	$A_{336}/(A_{475}-A_{814})$	3.56 ± 0.13
4747	2.10	$A_{475}/(A_{475}-A_{814})$	2.65 ± 0.11
5581	1.79	$A_{550}/(A_{475}-A_{814})$	2.34 ± 0.10
8024	1.25	$A_{814}/(A_{475}-A_{814})$	1.72 ± 0.09
11534	0.87	$A_{110}/(A_{475}-A_{814})$	1.32 ± 0.08
15369	0.65	$A_{160}/(A_{475}-A_{814})$	1.13 ± 0.07

Table 2.5. LMC 30 Doradus Extinction Curve Results

λ [Å]	λ^{-1} [μm]	Band Combination	R_λ	$R_\lambda DM16$[1]
2704	3.70	$A_{275}/(A_{555}-A_{775})$	5.28 ± 0.32	5.15 ± 0.38
3355	2.98	$A_{336}/(A_{555}-A_{775})$	4.83 ± 0.32	4.79 ± 0.19
5308	1.88	$A_{555}/(A_{555}-A_{775})$	3.16 ± 0.30	3.35 ± 0.15
7647	1.31	$A_{775}/(A_{555}-A_{775})$	2.28 ± 0.20	2.26 ± 0.14
11534	0.87	$A_{110}/(A_{555}-A_{775})$	1.30 ± 0.24	1.41 ± 0.15
15369	0.65	$A_{160}/(A_{555}-A_{775})$	0.83 ± 0.13	0.95 ± 0.18

Note. — (1) Note that De Marchi et al. (2016) call this value R and not R_λ.

is not taken into account. An additional systematic uncertainty in R_{225} which is not quantified results from *HST's F225W* red leak.[2]

We perform the same analysis on data from the 30 Doradus region in the Large Magellanic Cloud from the Hubble Tarantula Treasury Project (Sabbi et al., 2013, 2016) to compare to the De Marchi et al. (2016) extinction curve results. The HTTP survey uses observations in near-ultraviolet, optical, and near-infrared wavelengths in the range 0.27-1.5 μm. The unreddened locations for red clump stars in the 30 Dor region are those used by De Marchi et al. (2014) based on Girardi & Salaris (2001) models which De Marchi et al. (2014) identify (in Section 3.1 of their paper) as the RC stars with the lowest metallicity which fit the observations. To define the magnitude of the RC they conclude a metallicity of Z = 0.004 for the oldest (> 1 Gyr) RC

---

[2]The red leak affects the measured stellar magnitudes in *F225W* by contributing to an off-band flux in the red part of the spectrum (Dressel, 2014).
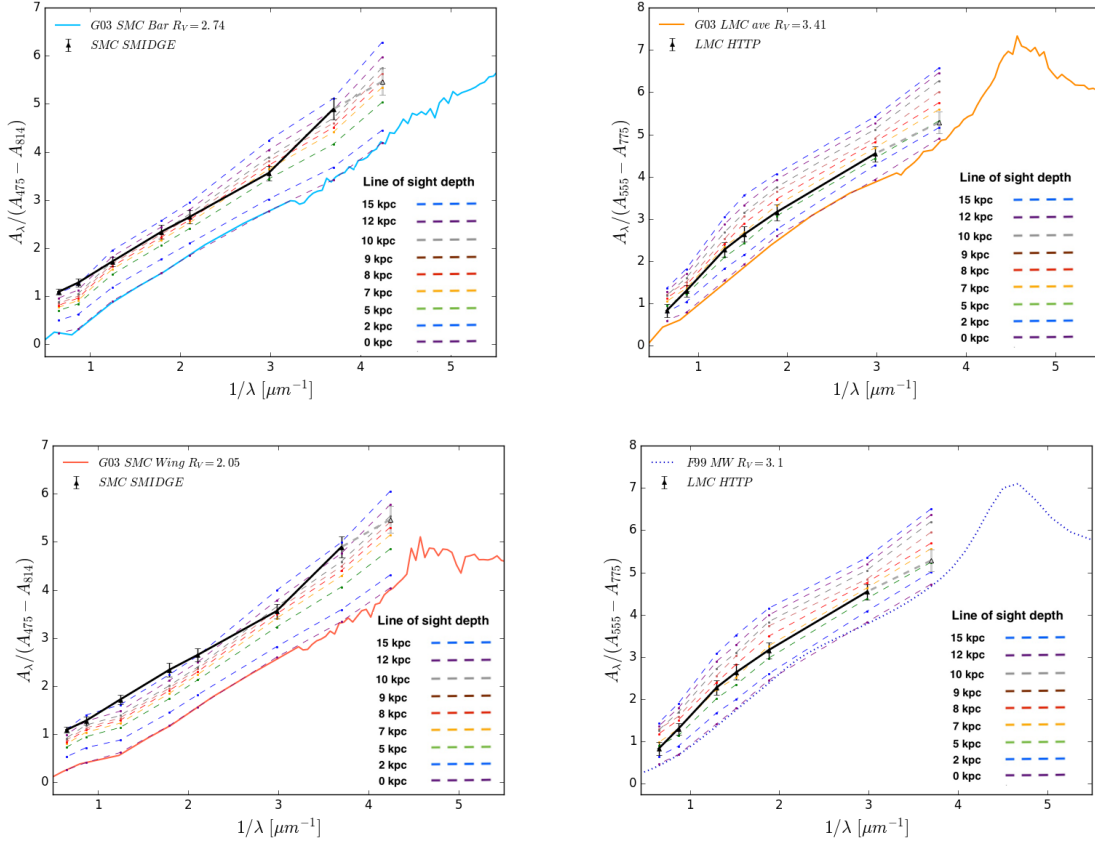
Figure 2.9. Effect of the line of sight depth of the SMC and the LMC on the SMC and LMC extinction curves of Gordon et al. (2003) and the MW R_V=3.1 curve of Fitzpatrick (1999) showing the offset in the presence of galactic depth between 0 and 15 kpc. The SMC SW Bar extinction curve found in this study and plotted in black in the two panels on the left indicates a line-of-sight depth of 10 ± 2 kpc when compared to the Gordon et al. (2003) SMC Bar curve, and a 12 ± 2 kpc when compared to the G03 SMC Wing curve. The LMC 30 Doradus extinction curve is plotted in black in the panels on the right, and indicates it is probing a region with a line of sight depth of 5 ± 1 kpc when compared to the Gordon et al. (2003) LMC average curve and 7 ± 1 kpc when compared to the Fitzpatrick (1999) MW R_V=3.1 curve. Details of this analysis are in Sec. 2.4.1.

stars in the 30 Dor region. To narrow down the average color for the RC they select stars of ages 1.4-3.0 Gyr. These unreddened RC location values are listed in Table 2.3. The extended red clump feature in the LMC color-magnitude diagrams is defined in the same way as the red clump in the SMIDGE analysis. 30 Dor color-magnitude diagrams are shown in Figure 2.7. Since the LMC is not as deep along the line of sight as the SMC, there is less vertical spread in magnitude which in turn allows for a clearer definition of the unreddened red clump in the LMC CMDs in Fig. 2.7. At the same time the LMC stars studied here are much more heavily reddened than the SMC stars and this results in an extended and noticeable reddened red clump streak. LMC uncertainties in reddening vector calculations stem from similar sources as those in the SMIDGE analysis discussed above. In our final analysis we calculate the slope for six LMC photometric bands - *F275W, F336W, F555W, F775W, F775U, F110W*, and *F160W*.

2.3.5 Results

R_λ results for the SMC and the LMC are given in Tables 2.4 and 2.5. We plot the extinction curves in Figure 2.8 along with other known extinction curves for comparison, such as those of Gordon et al. (2003) and Fitzpatrick (1999). Our results for the LMC are in good agreement with the results of De Marchi et al. (2016). For both the SMC and LMC we observe a larger R_λ than indicated by existing spectroscopic extinction curve measurements. For comparison, the new SMC extinction curve has $R_{475} = A_{475}/(A_{475} - A_{814}) = 2.65 \pm 0.11$, while the Gordon et al. (2003) equivalents are $R_{475}^{SMCbar} = 1.86$ and $R_{475}^{SMCwing} = 1.57$, and the Fitzpatrick (1999) Milky Way R_V=3.1 equivalent is $R_{475}^{MW} = 1.83$. The LMC extinction curve we measure has $R_{555} = A_{555}/(A_{555} - A_{775}) = 3.16 \pm 0.3$, while the Gordon et al. (2003) equivalents are $R_{555}^{LMCave} = 2.48$ and $R_{555}^{LMC2} = 2.61$, and the Fitzpatrick (1999) Milky Way R_V=3.1 equivalent is $R_{555}^{MW} = 2.37$. In the section which follows we discuss the interpretation of these measurements in light of recent observations that both the SMC and the LMC have a substantial line-of-sight depth which significantly impacts the calculations.

2.4 Interpreting Extinction Results

2.4.1 Line-of-Sight Depth Effect on Model Extinction Curves

We use our reddened red clump model to determine what the line of sight depth impact would be on SMC and LMC extinction curves observed by Gordon et al. (2003) and modeled by Weingartner & Draine (2001), as well as the Fitzpatrick (1999) model Milky Way curves. We begin by taking the R_λ value of an observed or modeled extinction curve as an input extinction curve slope R_{in} for the red clump model. The unreddened RC locations are those specified in Tables 2.2 and 2.3. We then apply the procedure described in Section 2.3.3 while we vary the line of sight depth between 0 and 15 kpc to extract an output slope R_{out}. The results plotted in Figure 2.9 indicate that an increasing depth along the line of sight steepens the reddening vector slope such that the extinction curve produced as a result experiences an offset towards higher R_λ.

As shown by the monotonic increase in R_{out} with depth, the line-of-sight depth effect is color-independent to first order in that all wavelengths are affected by the extended structure along the line of sight approximately equally. Essentially, the line of sight depth means that the reddened red clump stars are further away than the theoretical zero-point would suggest, leading to the reddened stars being offset to fainter magnitudes. In essence, distance offsets are mimicking a truly "gray" extinction curve. This fact allows us to separate the distance effect from the effect of extinction by dust. However, our sensitivity tests, described in the Appendix, illustrate that the assumed average RC distance modulus is somewhat degenerate with the line-of-sight depth shown in Fig. 2.9. In the sensitivity tests we move the RC zero-points for all filter combinations by ± 0.15 mag, which in effect shifts the average distance of the RC stellar distribution by ± 4.5 kpc (we note this is well outside the measured uncertainty of the average distance to the SMC; Scowcroft et al., 2016). The shift in R_{out} introduced by this offset is color independent to first order, as is the line-of-sight depth effect. We find that a $+ 0.15$ mag shift in the RC zero-point would lead to a line-of-sight depth measurement of ~ 7 kpc, rather than 10 kpc, and a - 0.15 mag shift leads to an even larger line-of-sight depth. This test shows that for

40

a reasonable range of SMC distance moduli, explaining our measured reddening vector slopes necessitates a large line of sight depth.

To test the degree of agreement between the resulting SMC SMIDGE region extinction curve and the extinction curves of Gordon et al. (2003), Fitzpatrick (1999), and Weingartner & Draine (2001), and to extract the line of sight depth for the galaxy from RC stars, we find the minimum χ^2 value by comparing our measured R_λ values to those for modeled reddened red clumps with varying line-of-sight depths and input extinction curves. A similar measurement is performed for our LMC extinction curve results. Our results suggest that the observed SMC and LMC red clump extinction curves indicate a significant depth along the line of sight in both galaxies. For the SMC, we find the χ^2_{min} at a line-of-sight depth of 10 kpc $\pm$ 2 kpc at a 90 % confidence level for the SMC Bar extinction curve. Comparing the SMIDGE extinction curve with other curves (Gordon et al. (2003)'s SMC Bar ($R_V = 2.74$), SMC Wing (AzV 456, $R_V = 2.05$), LMC2 Supershell ($R_V = 2.76$), LMC Average ($R_V = 3.41$), Fitzpatrick (1999)'s MW $R_V = 3.1$ and MW $R_V = 5.5$, and with Weingartner & Draine (2001)'s curves), we find that the newly-derived SMC extinction curve compares almost equally well with both the G03 SMC Bar and SMC Wing extinction curves (see left-side panels of Fig. 2.9). To differentiate between the two, our future work will use UV bright stars to study the *F225W* extinction, which will eliminate issues with the red leak.

For the LMC 30 Dor region we obtain a χ^2_{min} at a line-of-sight depth of 5 kpc $\pm$ 1 kpc at the 90 % confidence level. Comparing the LMC extinction curve with the above curves, we find that this curve similarly does not favor a single observed extinction curve but that it instead can be well-described by either the Gordon et al. (2003) LMCave extinction curve ($R_V = 3.41$) or the Fitzpatrick (1999) MW $R_V = 3.1$ curve. The latter would suggest a 7 ± 1 kpc line-of-sight depth.

2.4.2   Comparison to Other Extinction Curve Shape Measurements

Extinction curves in the SMC and the LMC have been measured spectroscopically by Gordon & Clayton (1998), Gordon et al. (2003), Maíz Apellániz & Rubio (2012) and Maíz

Apellániz et al. (2014). Gordon et al. (2003) derive extinction curves for the SMC and the LMC via the pair method using ultraviolet spectroscopy and optical and near infrared photometry. They base their conclusions on five stars in the SMC, four of which are in the SMC Bar producing an average $R_V = 2.74 \pm 0.13$, and one star in the SMC wing with $R_V = 2.05 \pm 0.17$. They also measure an average LMC2 Supershell ('LMC2') $R_V = 2.76 \pm 0.09$ for nine stars and an LMC Average $R_V = 3.41 \pm 0.06$ for ten stars. These extinction curves are plotted in Fig. 2.8 for comparison with the extinction curve results from this study. We observe a general consistency in our results for the shape of the SMC and LMC extinction curves with the shape of the Gordon et al. (2003) curves for wavelengths longward of $F225W$'s. At the same time we note the offset between the two sets of curves which we attribute to the effect of the depth of the two galaxies along the line of sight described in Sec. 2.3.2. We can not make a strong statement about the UV portion of the curve as we are limited by photometric effects when using red clump stars.

De Marchi et al. (2014), De Marchi & Panagia (2014), and De Marchi et al. (2016) use UV-IR multiband HST photometry to examine 30 Doradus in the LMC. They find an offset between their results and the results of Gordon et al. (2003) and the canonical Galactic extinction curves due to red clump reddening vector slopes which are considerably steeper than existing measurements. Our measurements reproduce De Marchi et al. (2016)'s results. The authors attribute their results to the presence of "gray" extinction at optical wavelengths due to the vertical offset of their curves from the Galactic and Gordon et al. (2003) curves. Our model explains this effect as the result of the line-of-sight depth of the LMC where the extinction curve is well-reproduced by the Gordon et al. (2003) LMC average R_V=3.41 extinction curve with a 5-kpc line-of-sight depth (see Fig. 2.9).

Maíz Apellániz & Rubio (2012) use UV spectroscopy to obtain the extinction for four stars in the SMC quiescent cloud B1-1, and NIR/optical photometry to obtain the extinction curve for the five SMC stars studied by Gordon et al. (2003). They conclude a significant variation from star to star in the extinction curve for the SMC B1-1 stars, particularly in the strength of the 2175 Å bump. Their results may imply that their sources are sampling ISM environments with

a different dust composition. In the section which follows we discuss the type of environment probed by the SMIDGE region and conclude that our results are most likely dominated by the diffuse ISM. However, we currently do not have a conclusive result about the strength of the 2175 Å bump due to the limitations of our red clump photometry.

Maíz Apellániz et al. (2014) use spectroscopy and NIR and optical photometry of O and B stars to derive the extinction curve inside 30 Doradus. They find an R_V equivalent which is also larger than the R_V suggested by Galactic or Gordon et al. (2003) extinction cures. Although our results for 30 Dor agree with the authors' R_V=4.5 curve at optical wavelengths when the curves are expressed in $E(B-V)$ instead of $E(F555W-F775W)$ using spline interpolation, our extinction curve is better reproduced at NIR wavelengths by the Gordon et al. (2003) LMC average R_V=3.41 curve with a 5-kpc line-of-sight depth. The latter is also the case when the curves are normalized to A_V. We obtain very similar results when we compare the De Marchi et al. (2016) curve (with values in the last column of Table 2.5) to the Maíz Apellániz et al. (2014) curve.

Recent work by Hagen et al. (2017) uses SMC UV, optical, and IR data integrated into 200" regions to measure the attenuation curve of the SMC. They find a 2175 Å bump in most of the galaxy and a dust curve which is steeper than the Galactic curve. We note that their study measures the attenuation curve (i.e. the combined effects of extinction, scattering and geometry (see Calzetti et al. (1994))). Our results, which are extinction curves, are not directly comparable to this study.

Red clump stars have been extensively used as a distance indicator to objects within the Milky Way and nearby galaxies (Cannon, 1970; Girardi & Salaris, 2001; Bovy et al., 2014, also see Girardi (2016) and references therein). Within the Galaxy in particular, they have been used to indicate the distance to the Galactic Center (Paczyński & Stanek, 1998; Alves, 2000; Francis & Anderson, 2014) and to open clusters (Percival & Salaris, 2003). Distribution of stellar distances in the Magellanic Clouds have been measured with RR Lyrae and Cepheids (Haschke et al., 2012; Subramanian & Subramaniam, 2012; Scowcroft et al., 2016; Jacyszyn-Dobrzeniecka

et al., 2016, 2017), and with red clump stars (Subramanian et al., 2017). Our results in Sec. 2.4.1 indicating that the SMC has a depth of ~10 kpc along the line of sight and that the LMC's depth is ~5 kpc are generally consistent with distances derived from the Cepheids and RR Lyrae studies above.

2.5   Discussion

We present measurements of the average extinction curve shape in the southwest bar region of the Small Magellanic Cloud covering an area of 100×200 pc using red clump stars. Our results indicate an extinction curve consistent with measurements from UV spectroscopy performed by Gordon et al. (2003). The significantly elongated structure of the SMC along the line of sight causes a perceived steepening of the reddening vector which if not accounted for would give the appearance of an extinction curve with a "gray" component. The latter is the conclusion of De Marchi et al. (2016) for the extinction curve of the 30 Doradus nebula in the LMC, which they attribute to the presence of an additional component due to gray dust. We conclude that gray extinction is not necessary to explain the observations in the SMC and the LMC when one accounts for the depth of the stellar distribution along the line of sight.

There are several implications of our measurements. By sampling a relatively large region of the interstellar medium in the SMC, we can compare our averaged extinction curve results to measurements derived using the pair method targeting individual stars. We do this while noting that compared to the pair method, the technique we use presents a number of advantages, one of which is that by observing red clump stars on a color-magnitude diagram we do not need to know the location of the dust since we are taking an average measure of dust properties. One of the pair method's major limitations comes from having to carefully select stars in regions containing a significant amount of dust. At the same time, due to photometric limitations resulting from *HST*'s red leak and the faintness of the stars in *F225W*, the red clump technique we use in this paper does not allow us to have a strong handle on the strength of the 2175 Angstrom bump or

the far UV rise.

One comparison we can make is with the work of Gordon et al. (2003) who studied SMC extinction with the pair method. An interpretation of the similarity between our results and those of Gordon et al. (2003) may be that over a relatively large area in the SMC there is little variation in the extinction curve shape. Another possibility is that both studies are sampling the same ISM phases. The dust probed with O- and B-type stars such as those from the UV spectroscopy sight lines of Gordon et al. (2003) is generally assumed to be located in the diffuse envelopes of molecular clouds which would bias the extinction curves towards regions of star formation dominated by grain growth. However, the Gordon et al. (2003) SMC Bar A_V extinctions of 0.35 - 0.68 indicate that these sight lines are probing the diffuse ISM, or at least regions where coagulation and grain growth are unlikely to have happened.

To address the hypothesis that both sets of extinction curves are probing the same ISM phases (e.g., diffuse atomic or molecular gas), we assess the type of environment the SMIDGE survey area covers by calculating the fraction of stars along lines of sight that have abundant molecular gas. Using APEX ^{12}CO (2–1) mapping of the SW Bar at 28$''$ resolution (A. Bolatto, private communication), we make a conservative cut at $I_{CO} = 1$ K km s^{-1} to define molecular regions. We find that 23% of the red clump stars are found toward such regions, indicating that our new average extinction curves are dominated by diffuse material. It remains a possibility that both Gordon et al. (2003) and our work are sampling mainly the diffuse ISM, rather than molecular gas where grain growth may occur. In future work we will investigate the change of the extinction curve with ISM phase using the full stellar populations available from SMIDGE.

Another implication of our study is that extinction in the SMC and the LMC can be explained without the need to invoke "gray" extinction as suggested by De Marchi et al. (2014), De Marchi & Panagia (2014), and De Marchi et al. (2016) for the LMC. If there were gray dust, the latter suggest that the reason may be the selective addition of fresh large grains due to Type II supernova explosions in 30 Dor. If recent supernova were the cause, this could suggest a bias towards gray extinction for galaxies with high star formation rates. Gray dust also has

implications for studies of the cosmological expansion with supernovae as their faintness could be interpreted as extinction without much reddening which would invariably impact inferring distances on cosmological scales. Observationally there are demonstrations of the presence of gray extinction (Strom et al., 1971; Dunkin & Crawford, 1998; Gall et al., 2014). However, our study concludes that extinction curves in the LMC can be explained without the need for an extra "gray" component of the dust, thus removing the argument for supernova dust production modifying the extinction curve.

2.6   Conclusions

We use color-magnitude diagrams based on SMIDGE *HST* multiband photometry to measure the slope of the reddening vector of red clump stars in the southwest bar of the Small Magellanic Cloud in order to derive the extinction curve shape in the region. After noting that the depth along the line of sight of the SMC has a significant bearing on extinction curve shape results using this method, we model this effect to understand its impact on our results. When we properly account for the line-of-sight depth and analyze its effect on extinction curves, we conclude that the effect is significant and tends to give the appearance of steeper reddening vector slopes which in turn produce what appears to be gray extinction. Motivated by recent extinction curve shape results for 30 Dor in the Large Magellanic Cloud by De Marchi et al. (2014) and De Marchi et al. (2016) who use the same red clump method and also report an offset, we perform the same analysis on 30 Dor in the LMC.

Our conclusions for the optical and near-infrared portions of the extinction curve shape in both the SMC and the LMC is consistent with previous work such as the analysis of Gordon et al. (2003) using spectroscopic measurements. Since depth effects in both galaxies produce an offset in the extinction curve due to a perceived steepening of the reddening vector, we conclude that it is the shape of the Gordon et al. (2003) curves which our extinction curves match rather than a specific R_V value. Our recommendation to correct for dust extinction for individual objects

is to therefore use the extinction curves derived by Gordon et al. (2003). Correcting for dust extinction when using a full stellar population, however, calls for the need to account for the depth of the SMC and the LMC. Additionally, we show that it does not have to be the case that gray extinction is responsible for the offset in the LMC 30 Dor extinction curve as De Marchi et al. (2014) and De Marchi et al. (2016) conclude, but that rather one needs to account for the depth along the line of sight when using methods relying on stellar distances to determine the extinction curve shape. Future work aims at modeling the effect of extinction on all CMD features rather than simply on a generic red clump. Such an analysis will provide a way to understand the more subtle effects of dust on the extinction curve shape.

Figure 2.10. Sensitivity of the calculated reddening vector slope to three parameters. The top plot shows the sensitivity to the approximate slope which determines the width of the reddened red clump selection region. The middle plot tests the sensitivity to the intrinsic width in color of the unreddened red clump. The bottom plot illustrates the sensitivity to the unreddened red clump location.
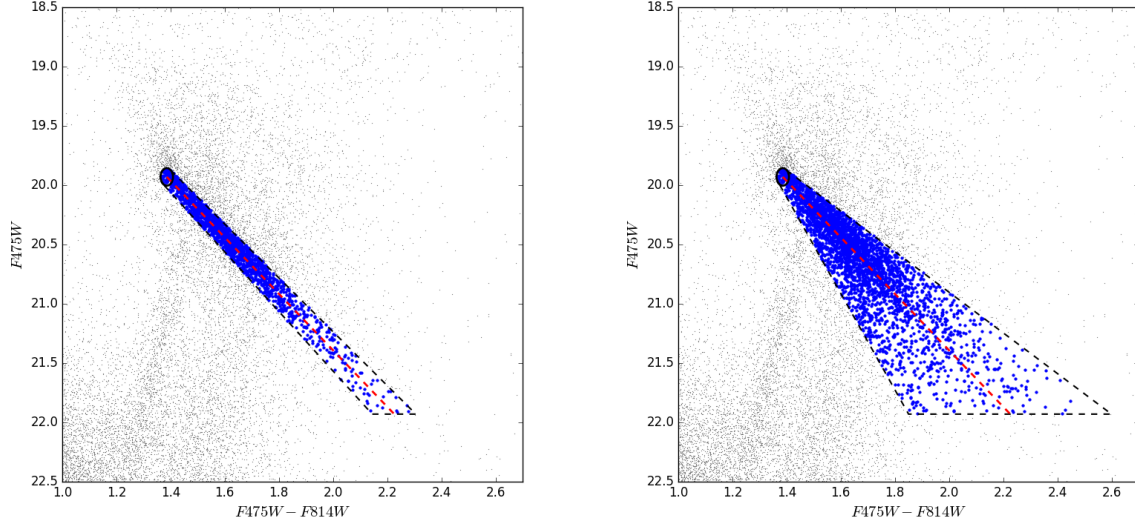
Figure 2.11. Red clump selection with variations in the approximate reddening vector slope to determine the effect of the selection on the slope calculation. The top panel shows a selection box corresponding to a $\pm 5\%$ variation in the approximate slope; the bottom panel shows the selection after a $\pm 40\%$ variation is added. The blue points represent the highlighted reddened red clump stars inside the selection region.

2.7 Appendix (Chapter 2): Model Sensitivity Tests

A number of factors influence the calculated slope of the reddening vector using the red clump method. We perform tests to determine how this slope varies with changing parameters such as:

- the width of the selection boundary around the red clump,
- the intrinsic width of the unreddened red clump, and
- the unreddened red clump location.

We specify the width of the reddened red clump selection region by first calculating the feature's approximate slope and then adding and subtracting a percent to this slope to define the slopes of the two boundaries tangent and extending redward of the unreddened RC ellipse (see Sec. 2.3.4, top). To understand the behavior of the resulting reddening vector slope as we define these tangent boundaries, we vary the percent added and subtracted to the approximate
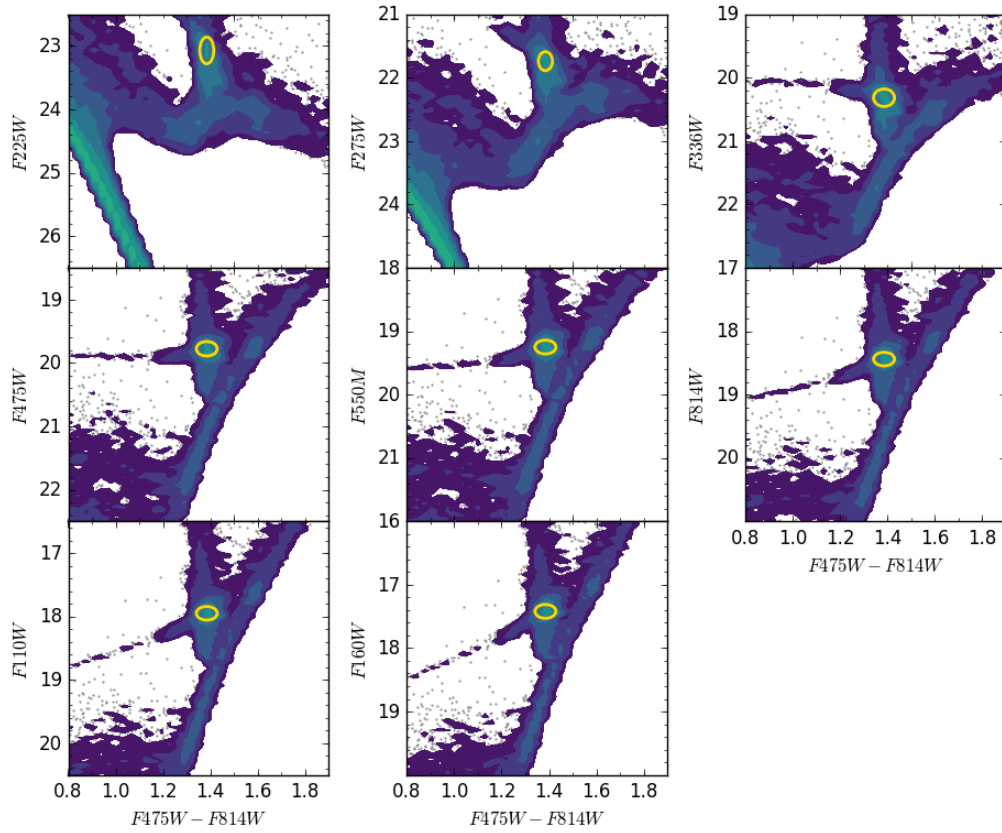
Figure 2.12. SMC synthetic CMDs generated to determine the location of the unreddened red clump (yellow ellipse, with values indicated in Table 2.2) as described in Section 2.3.2 and Figure 2.3.

slope between 0% and 40% (Fig. 2.10, top). A 0% variation would mean that the reddened red clump boundary encompasses a relatively narrow region defined by two tangents to the ellipse of the unreddened red clump running parallel to the approximate slope. A 40% variation, on the other hand, means that the red clump boundary encompasses a relatively large cone-shaped region whose width is set by ellipse tangents with slopes $\pm 40\%$ of the approximate slope. These selection boundaries are illustrated in Fig. 2.11 where we more realistically depict the $\pm 5\%$ case rather than the 0% case.

We also explore the effect the intrinsic width of the unreddened red clump has on the slope of the reddening vector (Fig. 2.10, middle). This width is present due to the age and metallicity uncertainties of the red clump discussed in Sec 2.3.2. We observe the effect of a changing width on our results by varying σ_{col} from 0.06 mag (see Table 2.2) to twice this value.

Lastly, to allow for a potential ambiguity in the unreddened position of the red clump in magnitude due to the distance effect discussed in Sec. 2.3.2, we let the centroid of the RC distance modulus vary by 0.15 mag to simulate the effect of a distance shift away from 62 kpc ($\mu = 18.96$, Scowcroft et al. (2016)) by ~4.5 kpc (Fig. 2.10, bottom).

We observe that the variation in both the approximate reddening vector slope and the width of the unreddened red clump produces relatively constant results which fall within the overall uncertainties. The slope of *F225W* is most susceptible to variation due to the steepness and faintness of the red clump at this wavelength. Our third sensitivity test which varies the magnitude position of the unreddened red clump by ± 0.15 mag away from the values given in Table 2.2 results in a calculated reddening vector slope with a similar offset across each CMD. For the range of magnitude variations we find a χ^2_{min} which supports a significant line-of-sight depth (between 7 and 15 kpc). We therefore conclude that a variation in the unreddened red clump zero-point does not remove the necessity to account for a substantial galactic depth when analyzing the extinction curve using the red clump method.

Chapter 3

Three-Dimensional Structure and Dust Extinction in the Small Magellanic Cloud

Abstract of Chapter 3

We examine the three-dimensional structure and dust extinction properties in a ~200 pc × 100 pc region in the southwest bar of the Small Magellanic Cloud (SMC). We model a deep Hubble Space Telescope optical color-magnitude diagram (CMD) of red clump and red giant branch stars to infer the dust extinction and galactic structure. We model the distance distribution of the stellar component with a Gaussian distribution and find a centroid distance of 65.2 (distance modulus $\mu = 19.07$ mag) with a FWHM ≈ 11.3 kpc. This large extent along the line of sight reproduces results from previous studies using variable stars and red clump stars. Additionally, we find an offset between the stellar and dust distributions, with the dust on the near side relative to the stars by $3.22\,^{+1.69}_{-1.44}$ kpc, resulting in a 73% reddened fraction of stars. Modeling the dust layer with a log-normal A_V distribution indicates a mean extinction $\langle A_V \rangle = 0.41 \pm 0.09$ mag. We also calculate $A_V/N_H = 3.2$ - 4.2×10^{-23} mag cm^2 H^{-1} which is significantly lower than the Milky Way value but is comparable to previous SMC dust-to-gas ratio measurements. Our results yield the first joint dust extinction and 3D geometry properties in a key region in the SMC. This study demonstrates that CMD matching can be a powerful tool to simultaneously constrain dust extinction and geometry properties in nearby galaxies.

3.1 Introduction

Understanding dust and dust extinction at low metallicity is important for a number of reasons. Dust in galaxies attenuates starlight, and affects the star formation, radiative transfer, thermodynamics, and chemistry in the interstellar medium (ISM). The amount and type of dust is likely strongly dependent on metallicity (e.g. Dwek, 1998; Zubko, 1999; Clayton et al., 2003; Sofia et al., 2006; Zhukovska et al., 2008; Asano et al., 2013; Rémy-Ruyer et al., 2014; Roman-Duval et al., 2014; Feldmann, 2015; Chastenet et al., 2019; De Vis et al., 2019), making low-metallicity dust studies critical due to the prevalence of these conditions in the early universe.

Fundamental dust extinction properties in low-metallicity environments show distinct differences from the Milky Way. For example, the observed extinction curve of the Small Magellanic Cloud (SMC) at 1/5 - 1/8 $Z_\odot$ (Dufour, 1984; Russell & Dopita, 1992; Kurt et al., 1999; Lee et al., 2005; Rolleston et al., 1999, 2003) shows a steep UV rise and a weak or absent 2175 Å bump (Lequeux et al., 1982; Prevot et al., 1984; Gordon & Clayton, 1998; Gordon et al., 2003; Maíz Apellániz & Rubio, 2012). These differences may hold clues to how the dust in such environments behaves and evolves, in turn affecting galaxy evolution.

Accounting for dust extinction at high-redshift can be challenging (Somerville et al., 2001), but fortunately a great deal can be learned from nearby low-metallicity galaxies which can be considered analogues to the high-redshift universe where galaxies must have formed at a very low metallicity (Madau & Dickinson, 2014). The SMC in particular is an especially suitable target due to its proximity, with its center at $\sim$ 62 kpc (de Grijs & Bono, 2015; Scowcroft et al., 2016). Indeed, "SMC-like" extinction is the standard used to account for dust at high-redshift and/or low metallicity (Gordon et al., 2003), thus it is a natural target for low-Z studies of dust properties.

The SMC's proximity also allows us to study in detail its geometry, including the distance to the stars and the ISM, and the relative positions of these two galactic components. One of the goals of our study, named the Small Magellanic Cloud Investigation of Dust and Gas
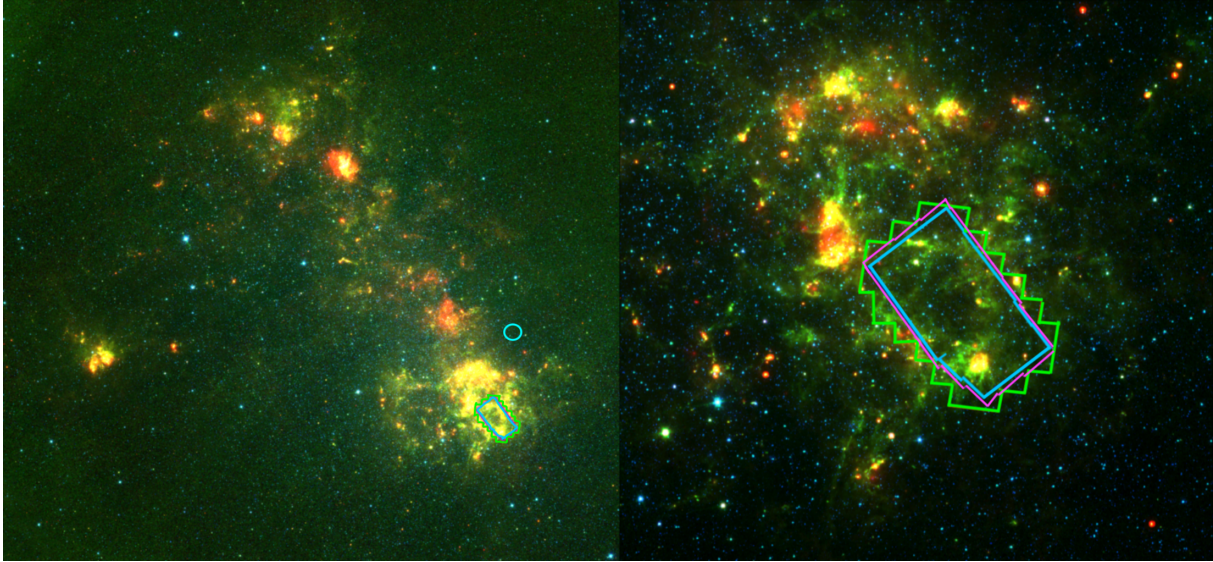
Figure 3.1. The SMIDGE survey field (100×200 pc) in the SW bar of the SMC is overlaid on a *Spitzer Space Telescope* composite image in 3.6, 8, and 24 μm from the SAGE-SMC survey (Gordon et al., 2011). The *HST* imaging footprint is shown for ACS/WFC (green), WFC3/UVIS (magenta), and WFC3/IR (blue). The cyan circle indicates the Weisz et al. (2013) SMC-2 field used in our star formation history analysis.

Evolution (SMIDGE) (Yanchulova Merica-Jones et al., 2017, hereafter YMJ17), is to examine dust extinction and 3D geometry holistically and derive resolved maps of extinction (A_V and R_V) for low metallicity dust.

Traditionally, the shape of dust extinction curves are studied using the pair method (Trumpler, 1930; Massa et al., 1983; Cardelli et al., 1992) which compares the spectra of a reddened and an unreddened star of approximately the same spectral type. However, this method relies on individual lines of sight to a select sample of UV-bright stars with high signal-to-noise data. An efficient and complementary technique to measure dust extinction and the extinction curve is to use multiband photometric observations of resolved stars to measure the average extinction properties in a galactic region. Using resolved stellar photometry to measure dust extinction, however, may require modeling the galactic geometry as well.

Interstellar dust is expected to affect all color-magnitude diagram (CMD) features. These effects depend on its distribution relative to the stars. If the dust is in a foreground screen

relative to the stars, the stars will be reddened to various degrees depending on the ISM column density distribution (often observed to be log-normal (Hill et al., 2008; Kainulainen et al., 2009; Hennebelle & Falgarone, 2012)). If it is mixed with the stars, some stars will experience only a fraction of the overall reddening. If the dust is in a thin layer and the stars are in a spatially extended distribution (assuming they are not embedded in the dust layer), a part of the CMD will be foreground to the dust and unreddened, while the rest will experience the full reddening from the dust layer. In general, CMD features that are compact or perpendicular to the reddening vector are the most useful for measuring the effects of dust and geometry. CMD modelling of these effects can give clues about the relative line of sight depths of the dust and the stars and the reddened fraction of stars. The models can then be used to produce a map of the extinction and/or the geometry. Extinction mapping of reddened stars using color-color or color-magnitude diagrams has been the subject of numerous Milky Way (Lombardi & Alves, 2001; Nataf et al., 2013; Schlafly et al., 2016), M31 (Dalcanton et al., 2015), LMC (Imara & Blitz, 2007; Dobashi et al., 2008; Choi et al., 2018), and SMC (Gardiner & Hawkins, 1991; Dobashi et al., 2009; Yanchulova Merica-Jones et al., 2017) studies.

Geometric effects, such as an elongation of the galaxy along the line of sight spreads the stars in magnitude, but not color. Dust, on the other hand, affects both the color and magnitude of stars in a CMD. Features that would appear narrow in the absence of dust tend to get spread out when there is dispersion in the amount of extinction due to the column density structure of the ISM. If this effect can be modelled, then we can measure the mean and the width of the extinction distribution. By finding the stars' observed displacement in a CMD from a predicted theoretical unreddened location, we can calculate the dust extinction in magnitudes, A_λ, where λ is the approximate effective wavelength of each photometric band. We can measure $R_\lambda = A_\lambda/(A_\lambda' - A_\lambda'')$ (related to the dust grain size distribution) from a single CMD color. Measuring R_λ across photometric bands from IR to UV allows us to sample the extinction curve shape.

The SMC, however, presents a unique challenge due to the combined effects of its

extinction, relative proximity and its appreciable elongation along the line of sight (Subramanian & Subramaniam, 2009; Haschke et al., 2012; Jacyszyn-Dobrzeniecka et al., 2016). For example, in YMJ17 we found that to accurately measure the SMC extinction curve from the slope of reddened red clump (RC) stars, we also needed to account for the galactic depth along the line of sight. This effect, due to the appreciable spread in stellar distances, could give the impression of a steeper RC slope since stars behind the dust layer will have fainter magnitudes at increasing distances. This observation would in turn seem to imply higher R_λ values. We accounted for the depth by employing a simple model for the RC which specified a theoretical unreddened RC location based on the local star formation history (SFH), and a set of parameters for the extinction distribution, the extinction law, and the galactic depth along the line of sight.

In this paper, we build on our previous work and use the full RC and red giant branch (RGB) CMD to model the dust extinction, 3D geometry, and the SFH holistically. The effects of dust are ubiquitous in the SMIDGE data, and beside spreading the reddened RC into a streak, dust also widens the reddened RGB. The signature of SMC's geometry is most clearly seen in the doubled RGB which is a result of the relative thicknesses along the line of sight and the absolute positions of the dust and stellar components of the galaxy. The SMC's depth is not as immediately obvious from the CMD, but it nonetheless results in a measurable and significant spread in the magnitude of both the RC and the RGB. Analyzing the RC and the RGB simultaneously, versus only the RC, allows us to better constrain the CMD stellar number counts statistically (and thus the SFH), and to separately account for the effects of galactic geometry and dust extinction. The reason for this is that the RC reddening vector slope is a product of both the extinction curve and galactic geometry (where in YMJ17 we showed these can be degenerate without additional information). At the same time, while it would be challenging to constrain the slope of the extinction vector using the RGB alone, the RGB very strongly constrains the relative offset between the dust and the centroid of the stellar distribution. Modeling the combined effects of the RC and the RGB in theory enables one to separate these effects and better constrain the slope of the extinction vector.

Accurately modeling the CMD requires a representative star formation history (SFH) as a starting point. There have been numerous efforts to obtain the SFHs in the SMC by modeling CMDs of resolved stellar populations (Tosi et al., 1989; Tolstoy & Saha, 1996; Harris & Zaritsky, 2001; Dolphin, 2002; Williams, 2002; Zaritsky & Harris, 2004; Cignoni et al., 2009; Weisz et al., 2013; Williams et al., 2017; Rubele et al., 2018). These models commonly need to account for the initial mass function (IMF), binary fraction, stellar evolution, time resolution, metallicity, distance, extinction, and photometric noise. Typically, the distance is a parameter specified by ancillary studies. Although some approaches can also account for the extinction within a galaxy, to simplify the solution most studies preferably examine regions with low internal A_V which is treated in a minimal way. Deriving the SFH itself seems to be unaffected by the presence of a significant galactic depth (Harris & Zaritsky, 2004; Rubele et al., 2018).

In this paper, we forward model the SMIDGE RC and RGB CMD with realistic noise and a model which includes geometry, distance, and dust. We first create synthetic model CMDs based on a set of input SFHs and stellar evolution parameters. Then we model the line-of-sight depth of the stellar distribution, the relative offset of the dust with respect to the stars, and the dust extinction distribution. Using a realistic model of photometric uncertainties, we compare model CMDs to SMIDGE observations to measure properties of the SMC's 3D distribution of gas and dust.

We begin in Section 2.2 where we briefly describe the SMIDGE data. We discuss the CMD matching process in Section 3.3 by providing details about how we model the SMIDGE star formation history, how we introduce 3D geometry and dust extinction into the CMD models, and how we account for the uncertainties. Our results are presented in Section 3.4 and discussed in Section 2.5. We conclude with Section 2.6 and provide more relevant information in the Appendix.
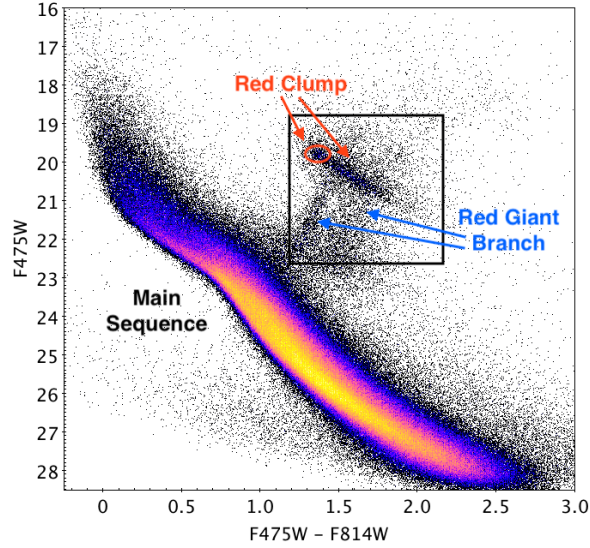
Figure 3.2. The SMIDGE *F475W−F814W* optical color-magnitude shows the boundaries of the red clump and red giant branch region analyzed here. Dust extinction is evident from the extended reddened red clump (which would theoretically be located within the red ellipse in the absence of dust) and the extended and bimodal reddened red giant branch (which would be represented by a single vertical sequence if unreddened). The observed bimodal RGB indicates that the dust layer is thin relative to the stellar distribution, with few embedded stars. These combined effects cause a distinct unreddened and reddened stellar populations.

3.2 Data

The SMIDGE survey (GO-13659) consists of eight-band *Hubble Space Telescope* (HST) imaging of a ~100 pc × 200 pc region in the SMC southwest bar. Its location is shown in Figure 3.1. We refer to YMJ17 for the details of the SMIDGE imaging footprint, HST camera and filter selections, photometry processing, and data culling. Also see the SMIDGE survey paper (Sandstrom et al., in preparation) for complete details. This work is based on the *F475W−F814W* vs *F475W* CMD shown in Figure 3.2 (where the units of all magnitudes are Vega magnitudes).

3.3 Matching Color-Magnitude Diagrams

3.3.1 CMD Modeling Approach

Our goal is to constrain the SMC dust extinction and 3D geometry parameters by finding the best matching model CMDs to the SMIDGE observations. The best match is determined

by comparing the number of stars in bins of color and magnitude between the modeled and the observed CMD. The optical CMD is ideal for this purpose due to its high signal-to-noise (compared to other available filter combinations), and broad wavelength baseline. The RC and RGB populations are intrinsically narrow and most strongly display the effects of dust extinction and 3D geometry as seen in Figure 3.2, where the RC is extended and the RGB is extended and doubled. We define the RC/RGB region as stars with *F475W−F814W* color of 1.2 - 2.2 mag and *F475W* magnitude of 18.5 - 22.75 mag and obtain a CMD subset of ∼12,000 stars. These ranges encompass the unreddened RC, the streak of the reddened RC, and the tip and base of the RGB.

We expect dust and geometry effects to impact all CMD features, thus we do not expect the results to be affected by expanding the selection box. The most critical information we rely on is contained in the RC/RGB. To model the dust and geometry we do not need to include the whole RGB, nor do we have to cut the selection box at fainter magnitudes with an exquisite precision. On the other hand, if the selection box is extended to fainter magnitudes, we would end up selecting main sequence stars, but this is not optimal since we do not include the unreddened main sequence in the analysis.

The location and number of stars in the CMD of the RC/RGB are mainly determined by these factors:

1. The SFH, i.e. the star formation rate SFR(t) and metallicity evolution Z(t), which defines the density, unreddened position and morphology of the stellar populations.

2. The distribution of dust extinction, which sets the additional spread in color and magnitude of the stars,

3. The extinction law, which sets the slope of the reddening vector,

4. The average distance modulus which sets the overall apparent magnitude of the stars,

5. The line-of-sight depth, which affects the spread in magnitude of the stellar populations, and,

6. The dust - stellar centroid offset (which we simply call the dust-stars offset), which, along with an assumption of the relative thickness of the dust and stellar distributions, determines the fraction of reddened stars and their distance distribution.

The CMD matching method we use is based on the approach presented in Dolphin (2002, hereafter D02) who developed a widely used technique for CMD modelling (e.g. Dolphin, 1997; Aparicio et al., 1997) to derive the SFHs of nearby galaxies with spatially resolved stellar populations (Tolstoy et al., 2009; Weisz et al., 2013, 2014). D02 created a maximum likelihood CMD fitting package - MATCH - to recover the best SFH by modelling the observed stellar density on a Hess diagram (a binned CMD showing the relative density of stars). We do not use MATCH per se to find the SMIDGE SFH or to fit the SMIDGE CMDs, but we use it to generate synthetic CMDs as we search for the best-fitting SFH, and we rely on the D02 approach conceptually to search combinations of dust extinction and geometry parameters for the best-fit CMD (see Sec. 3.3.1).

Knowing the SFH of the SMIDGE field is key for our analysis since it allows us to successfully reproduce the unreddened stellar positions and morphology on the CMD. An appropriate SMIDGE SFH in turn ensures that our CMD model is sensitive to potentially subtle variations in the SMC dust extinction and geometry properties. We therefore build upon the SFH refinement we made in YMJ17 to obtain a SMIDGE-specific SFH as detailed in Sec. 3.3.2.

In principle, finding the best fit model could involve searching through a large grid of CMD models covering all possible variables. The dimensions of this grid would be the SFH(t_i) and Z(t_i) for time bins t_i; the dust extinction parameters; and the 3D geometry parameters. Depending on the number of time bins in the SFH, such a calculation can become very computationally expensive. Since the SFH is not the primary goal of our study, and the extinction and geometry parameter fitting only requires a coarse knowledge of the SFH (focused on the RC and RGB), we proceed by simplifying the procedure into two steps outlined in detail in Sections 3.3.2 - 3.3.6.

Here is a conceptual outline of the CMD matching process:

1. Fit a star formation history for the SMIDGE field. (Section 3.3.2).

   (a) First generate unreddened synthetic CMDs according to a range of star formation rates and metallicities based on adjustments of a known SFH of a nearby region.

   (b) Compare RC/RGB stellar number counts between the unreddened synthetic and the observed CMDs in coarse bins designed to be insensitive to extinction and geometry (Fig. 3.3a). Select SFHs producing CMD statistics consistent with the SMIDGE stellar number counts.

   (c) Refine the SFH selection by applying a fixed set of geometry, distance, and dust extinction parameters (obtained in YMJ17) to the CMDs in 1b above. Also include realistic observational noise (see Part II). Recalculate the stellar number counts in the RC/RGB coarse bins. Perform a second SFH refinement using a narrower range of the cuts.

   (d) Select the SFH producing a best-fit coarse CMD and use it as a foundation for the analysis in Part 2.

2. Fit the dust extinction and geometry model combinations. (Section 3.3.3 - 3.3.6).

   (a) Generate model CMDs, with the SFH from step I, in a grid of combinations of dust extinction and 3D galactic geometry parameters.

   (b) Add observational noise to the stars in the model CMDs as characterized using artificial star tests.

   (c) Find the best fitting model and the uncertainty in the results by measuring the probability density function of the model grid.

We use `MATCH`'s `fake` CMD simulation tool (D02) to generate synthetic unreddened CMD models such as the one in the left panel of Figure 3.3 using the following fixed input

61

parameters: a Kroupa (2001) initial mass function, PARSEC stellar evolution models (Bressan et al., 2012; Tang et al., 2014; Chen et al., 2015), a binary fraction of 0.35, a foreground MW extinction of $A_V = 0.18$ mag derived from MW HI foreground towards the SMIDGE field (Muller et al., 2003; Welty et al., 2012), preliminary distance modulus $\mu = 18.96$ mag that we refine, as described below. The output of fake provides effective temperature, surface gravity, and metallicity for each star in the simulated CMD.

Although MATCH can also model a dust extinction distribution, it is not designed to model a spread of stellar distances within a galaxy. Furthermore, MATCH can take as an input a specified reddened fraction to imply a relative position of the dust and the stellar centroid, but it does not independently fit a dust-stars offset and stellar positions modeling a line-of-sight depth. Since the SMC geometry necessitates that we take into account these features, we develop a fitting method which builds on the MATCH foundation, but facilitates our use of more complex models for distance and extinction distributions with the syncmd [1] code. syncmd applies distance, reddening effects, and a noise model using functions available from the Bayesian Extinction and Stellar Tool (BEAST) of Gordon et al. (2016, hereafter G16) to create CMDs which we can directly compare to the data.

Accurate simulated noise is critical to our forward modeling approach as it accounts for photometric errors, crowding and incompleteness (See Section 4.4 in G16) through artificial star tests (ASTs) performed on the SMIDGE observations. For details on how ASTs are used in our analysis, see Section 2.3.1 of Williams et al. (2014) who use the same procedures for the Panchromatic Hubble Andromeda Treasury (PHAT) survey. We employ a conservative noise model using the "toothpick" method G16 which is used for data that are known to be correlated between photometric bands by treating the bands independently. The model is computed in equally spaced bins and assumes that each AST entry corresponds to one artificial star. See Section 5 in G16 for details on how ASTs are used to determine the noise model.

To properly model the CMD, we must also know the average distance to the stars in

---

[1] syncmd as of 2020 February 29 (C. Johnson): https://github.com/lcjohnso/syncmd/tree/simple_attenuation

the region. The SMC's mean distance modulus varies across the galaxy due to SMC's three-dimensional structure. Scowcroft et al. (2016) measure a distance modulus of $\mu = 18.96 \pm 0.01$ mag for the center of the SMC using Cepheid variables. Haschke et al. (2012) find a distance modulus varying between 18.94 mag $\leq \mu \leq 19.17$ mag using RR Lyrae stars and Cepheids in the bar and wing of the SMC. Nidever et al. (2013) use RC stars to measure the SMC line-of-sight depth and find $\sim$23 kpc for the eastern side and $\sim$10 kpc for the western side. Ripepi et al. (2017) use classical Cepheids and find a distance spread in the SMC SW Bar of 62.5 - 65 kpc ($18.98 \leq \mu \leq 19.06$ mag). Models of the SMC and the LMC (Besla et al., 2007, 2012, 2016), show that the Magellanic Clouds have experienced repeated interactions with each other which cause asymmetry in the stellar structures of the galaxies. Additionally, it is well-known that the SMC has a large depth along the line of sight (Subramanian & Subramaniam, 2009, 2012; Subramanian et al., 2017; Jacyszyn-Dobrzeniecka et al., 2016, 2017).

We investigate the distance modulus appropriate for the SMIDGE field in the SW Bar by performing a Poisson likelihood ratio CMD matching calculation (Section 3.3.5). First we create a synthetic CMD based on adjustments to the Weisz et al. (2013, hereafter W13) SMC SFH with the fixed input parameters described in Sec. 3.3.2 using a $\mu = 18.96$ mag for the center of the SMC. Then we shift the CMD in distance. The dust extinction and 3D geometry parameters we use are based on values we obtained in YMJ17. They are: an extinction law consistent with SMC Bar Gordon et al. (2003) extinction, a log-normal median $\widetilde{A_V} = 0.32$ and width $\langle \sigma_{A_V} \rangle = $ 0.3, a dust distance $D_{dust} = 60$ kpc (dust-stars offset of ~ 2 kpc), and a 10-kpc line-of-sight depth (resulting in a 0.65 fraction of reddened stars). These parameters are held constant as the synthetic CMDs are shifted in distance (magnitude) over the range 18.8 mag $\leq \mu \leq 19.3$ mag. Comparing to the SMIDGE observations, we find a best match at μ=19.07 mag as shown in Figure 3.4. The larger distance is expected for the SMIDGE region based on models of the extended stellar distribution placing SMC's NE regions closer than the SW regions (i.e. Haschke et al., 2012).

Table 3.1. Grid of Star Formation History parameters

Time [Gyr ago]	SFR [$10^{-4} M_\odot/yr$]	[M/H]
0.004 – 0.01	1.0 – 3.0	-0.65 – -0.45
0.01 – 0.03	1.0 – 3.0	-0.65 – -0.45
0.03 – 0.05	1.0 – 3.0	-0.65 – -0.45
0.05 – 0.16	1.0 – 3.0	-0.65 – -0.45
0.16 – 0.25	1.0 – 3.0	-0.65 – -0.45
0.25 – 0.40	1.0 – 3.0	-0.65 – -0.45
0.40 – 0.63	6.0 – 9.0	-0.70 – -0.60
0.63 – 1.0	1.5 – 4.0	-0.75 – -0.65
1.0 – 1.26	1.5 – 4.0	-0.75 – -0.65
1.26 – 1.59	1.5 – 4.0	-0.75 – -0.65
1.59 – 2.5	5.0 – 8.0	-0.95 – -0.85
2.5 – 3.2	5.0 – 8.0	-1.10 – -1.0
3.2 – 4.0	1.5 – 3.0	-1.10 – -1.0
4.0 – 6.3	1.5 – 3.0	-1.20
6.3 – 10.0	1.5 – 3.0	-1.40
10.0 – 14.13	1.5 – 3.0	-1.70

Note. — SFR and metallicity values in each age bin are equally spaced within the range given: 4 - 400 Myr age bins assume 5 values; 400 Myr - 3.2 Gyr assume 4 values, and bins with ages $\geq$ 3.2 Gyr assume 3 values. The metallicity spread at each time bin is 0.25.

Table 3.2. RC/RGB region stellar number counts for SFH selection

Region	All SFH Models	SMIDGE	Best-fit SFH
Red Clump	3000-6000	4385	4332
Upper RGB	800-1600	1350	1395
Mid RGB	1000-2500	1469	1621
Low RGB	1100-2400	1919	1899
Total RC + RGB	6000-12000	9123	9247

Note. — The Region column corresponds to each of the RC/RGB regions in Figure 3.3. The "All SFH Models" column shows the full range of stellar number counts in each region sampled by the combinations of SFH parameters in Table 3.1. The SFH cuts we impose are based on the SMIDGE stellar number counts in a region $\pm$ a percentage of the full range of this same region for all SFH models. The cuts are, (a) $\pm$ 10 % for the initial unreddened CMD models, and (b) $\pm$ 5% for the final reddened CMD models (there is a small deviation from these cuts for the mid RGB region (red in Fig. 3.5) due to a horizontal branch contribution noted towards the end of Section 3.3.2).
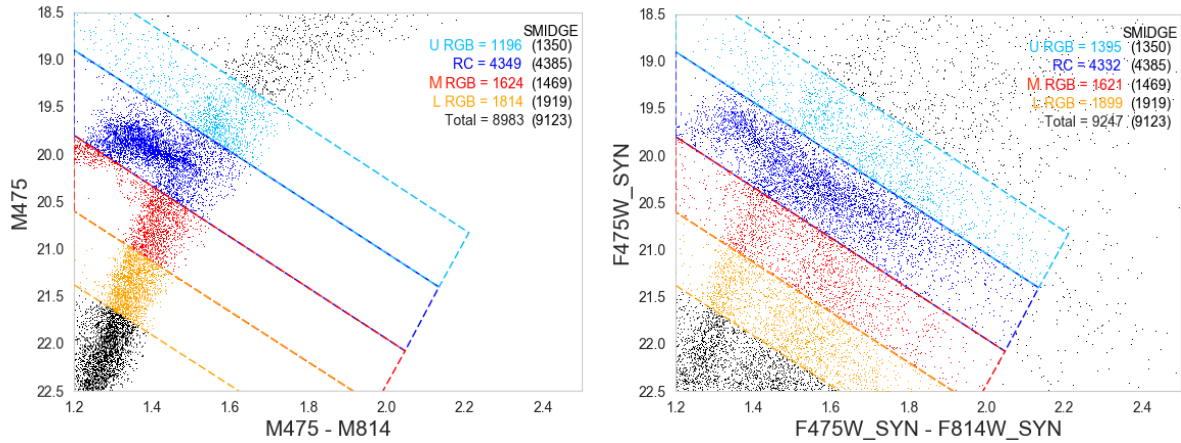
Figure 3.3. (Left) The unreddened synthetic CMD generated by `MATCH/fake` (Dolphin, 2002) based on the best-fit SMIDGE SFH chosen as described in Section 3.3.2. (Right) The same synthetic CMD processed with observational noise, dust extinction and geometry effects (Sections 3.3.4 3.3.3). The CMD is divided in the following subregions marked by diagonal bins: upper RGB (URGB; light blue), RC & RGB (blue), mid RGB (MRGB; red), and low RGB (LRGB; orange). A comparison of stellar number counts (in both the unreddened and the reddened CMDs) is made with the same regions in the SMIDGE field. The diagonal orientation of the bins follows the slope of the reddening vector (subject to SMC Bar extinction (Gordon et al., 2003), as found in YMJ17). The boundaries of the colored boxes coincide with the boundaries of the RC/RGB region chosen here and in the rest of our analysis. The stellar number counts are shown in the legend and are color coded correspondingly. The respective SMIDGE stellar number counts for each region are in black. In the reddened CMD on the right stars in CMD features outside of the defined RC/RGB region are reddened into some of the subregions and increase the number of stars there. Other regions (the RC) experience a negligible decrease in the number of stars due to a low/no contribution from CMD features lying in the opposite direction of the reddening vector and due to possible displacement outside of the defined reddening vector boundaries.
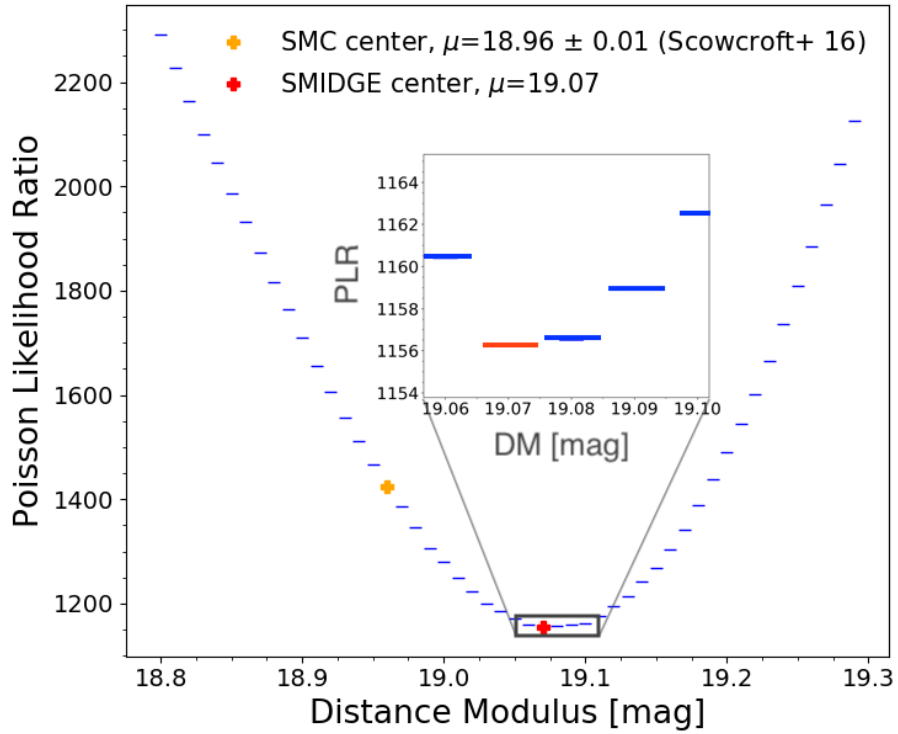
Figure 3.4. Distance modulus test for the SMIDGE field using a Poisson likelihood ratio test (see Section 3.3.5). The SMC center is measured to be at μ=18.96 $\pm$ 0.01 mag by de Grijs & Bono (2015) and Scowcroft et al. (2016), while we measure the center of the SMIDGE field to be located at μ=19.07 mag. The greater SMIDGE distance is expected from models and measurements of the extended stellar distribution.
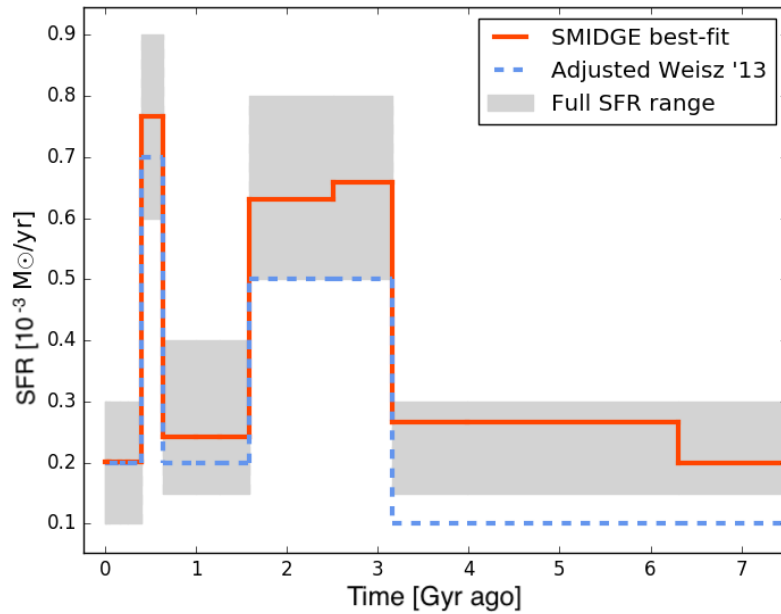
Figure 3.5. The SMIDGE SFH derived as described in Sec. 3.3.2. Adjustments to the Weisz et al. (2013) SFH are shown in dashed blue and were used in our Yanchulova Merica-Jones et al. (2017) work. We allow the SFR to vary within the range in the gray band with the resolution specified in Table 3.1. The SFH remains constant for ages beyond 7 Gyr. Our results for SMIDGE are in red and show SFR enhancements to the Weisz et al. (2013) SFH at almost all ages, including at times where our SFR is allowed to vary below their result. We see a SFR at older ages (≥ 3 Gyr) which is enhanced by a factor of 2.

3.3.2   Modeling the SMIDGE Star Formation History

While finding the SFH for the SMIDGE field is not the primary goal of our study, we need a SFH to generate a representative synthetic unreddened CMD as a starting point in the dust extinction and 3D geometry analysis. The SFH affects the stellar density, the position, and the morphology of CMD features. To first order, the degree of match between the model and observed CMD is set by the number of stars in the RC and the RGB. Our main focus, therefore, is on a SFH which reproduces the SMIDGE RC/RGB star counts, the position of the unreddened RC, and the width of the unreddened RGB, thus we use only the RC/RGB portion of the CMD defined by the cuts in Section 2.2.

SFH studies exist for regions near SMIDGE (Weisz et al., 2013; Rubele et al., 2015, 2018). Although those regions are close by, there are significant differences in the number counts of RC/RGB stars between their fields and SMIDGE. Adjustments to existing SFH results allow us to obtain a better fit to the observations since stellar number counts of RC and RGB stars are directly related to the SFR(t) over ages relevant for stars to evolve off the main sequence. For example, when modeling the unreddened RC in YMJ17, we performed a rough refinement of the SMC SFR(t) and Z(t) derived by W13 to match to first order the RC morphology and stellar positions (we neglected the stellar number counts; see Sec. 3.2 in YMJ17). Here we need an additional SFH refinement since our method is sensitive to stellar number counts, the width of the unreddened RGB, and the morphology of the red clump.

As a starting point we use the results of W13, who have used deep HST photometry to study the SFH of a region in the SMC Bar near SMIDGE (shown in Figure 3.1) with low internal dust extinction and an RGB stellar surface density which is somewhat lower than that of the SMIDGE region. Rubele et al. (2015, 2018) have also examined the SFH of regions near SMIDGE. Upon a SFH and age-metallicity comparison with (W13) we find that although the Rubele et al. (2015, 2018) results show higher metallicity and lower A_V, their results for older dominant RC ages compensate for these differences and show a consistency in the stellar number

68

counts and morphology of the RC and the RGB.

The RC consists of low-mass K giants in their He-burning post-RGB phase. A K giant has a nearly constant absolute magnitude during this phase of its evolution, which places RC stars within a tight clump in the CMD. The RC is thus less affected by age variations than the RGB in terms of CMD position. However, both the RC and the RGB are sensitive to the metallicity and metallicity dispersion at a given age. We model these effects simultaneously by varying both the SFR(t) and the metallicity, Z(t), to the ranges we specify in Table 3.1. We assume a constant metallicity dispersion for all ages.

The adjustments we made in YMJ17 to the W13 SFH are indicated by the dashed blue line in Figure 3.5 and include star formation enhancements at t = 500 Myr and 1.5 Gyr $\leq$ t $\leq$ 3 Gyr, and metallicity offsets to lower values by 0.2 - 0.3 dex. We additionally enhance the SFR in this work in order to match the total number of stars in the observed RC/RGB region ($\sim$ 12,300) where we increase the lower bound of the sampled SFR range for ages $\geq$ 3 Gyr to 1.5 $\times 10^{-4} M_\odot$ per year. We use a set of 16 logarithmic time bins — rebinned from the original 40 time bins of W13 — which range from 6.6 $\leq$ log(t) $\leq$ 10.15 (listed in Table 3.1). We make this simplification since the RC/RGB populations consist of older ages and smoothing over the W13 bins at younger ages results in a minimal variation in the relevant areas of the CMD.

We search metallicity centered on values between [M/H] = -1.7 and -0.45 dex at different time bins based on small metallicity adjustments to the nearby W13 region. We search a range of $\pm$ 0.1 dex at time bins up to 4 Gyr, while the spread of the distribution is fixed at all time bins. We use a metallicity dispersion described by a uniform distribution to account for the metallicity spread at a given age. Separately, we determine the best metallicity dispersion in a range between 0.1 - 0.3 dex by comparing the width of the unreddened RGB in color to that of model CMDs in the following way: we define a box around the unreddened RGB in a highly reddened region where the unreddened and the reddened stars are well-separated from each other, and compare the standard deviation in color between the models and the SMIDGE data. We find that a metallicity spread of 0.25 dex best reproduces the unreddened RGB width, and therefore

adopt this value in all subsequent CMD models.

As the first step on our SFH fit, we generate synthetic CMDs without noise, extinction or geometric effects. We search for the best match in a range around our initial estimate for the SFH (Section 3.3.1) illustrated by the width of the gray band in Figure 3.5. We define coarse diagonal CMD bins representing the upper RGB, RC & RGB, mid RGB (below the reddened RC), and lower RGB (Figure 3.3) , and compare the stellar number counts per bin in each unreddened synthetic CMD to SMIDGE. We search for an initial set of SFHs producing CMDs that fall within the cuts in Table 3.2 which are chosen to allow for a small variation around the SMIDGE counts. The diagonal bins are parallel to the extinction vector which we know from the approximate slope of the RC reddening vector in YMJ17. They are designed to be relatively wide in color and magnitude such that reddening, geometry and noise would minimally affect the number counts.

To account for any subtle changes to the CMD stellar number counts due to dust and geometry and due to the reddening of stars with unreddened positions bluer than $F475W - F814W$ = 1.2 mag, we refine the initial selection of models by transforming the unreddened CMDs with `syncmd` into models incorporating geometry, dust extinction, and observational noise effects. We use the dust extinction and geometry values we found for SMIDGE in YMJ17 as approximate parameters and follow the process in Sections 3.3.3 and 3.3.4. Our final SFH choice is guided by a second round of narrower cuts around the SMIDGE number counts (see Table 3.2) which improve the fit slightly. The resulting best-fit SFH is shown in red in Figure 3.5.

We note that the model CMDs overpredict the contribution of red horizontal branch (HB) stars due to known challenges in modeling the HB morphology stemming from RGB mass-loss uncertainty (Catelan, 2009; Gratton et al., 2010). Despite this contamination, we do not expect the HB contribution to be significant or to dominate the statistics given that we find that the HB accounts for only about 3% of the total number of RC/RGB stars.

The SFH we find to be suitable for the SMIDGE field in Figure 3.5 shows enhancements to the W13 SFR at almost all ages, even those where we allowed values to vary below their

Table 3.3. Model CMDs Grid Parameter Ranges

Parameter	Min	Max	Resolution
Galactic Line-of-Sight Depth[1]	.05 mag (3.5 kpc)	.275 mag (21.3 kpc)	.025 mag
Dust - stars offset[2]	.02 mag (.6 kpc)	.2 mag (5.7 kpc)	.02 mag
Dust Extinction[3], log-normal $\widetilde{A_V}$	.23 mag	.41 mag	.02 mag
Dust Extinction, width $\widetilde{\sigma_{A_V}}$	.40	.95	.05

Note. — (1) The SMIDGE distance modulus is measured to be μ=19.07 (see Fig. 3.4) indicating a distance of 65.16 kpc. Galactic depth range in kpc is expressed as the FWHM of the Gaussian stellar distribution where μ=19.07 $\pm$ 0.05 mag (lowest grid boundary for the galactic depth) corresponds to a FWHM = 3.53 kpc (1 σ depth of 1.50 kpc) and μ=19.07 $\pm$ 0.275 mag (highest grid boundary) corresponds to a FWHM = 19.81 kpc (1 σ depth of 8.41 kpc). (2) The dust layer is offset on the near side of the stellar distribution by the distance indicated. (3) Log-normal distribution of dust extinctions where $\widetilde{A_V}$ is the log-normal median, and $\widetilde{\sigma_{A_V}}$ is the dimensionless distribution width (see Sec. 3.3.3.)

result. The most significant difference is at older ages ($\geq$ 3 Gyr) where the SFR is enhanced by a factor of 2. The two star formation peaks at more recent times are also slightly enhanced. These differences are expected due to the higher stellar surface brightness of the SMIDGE field compared to the W13 field.

3.3.3 Modeling the Extinction

We use the best fit SFH to generate and search a finely resolved grid of synthetic model CMDs sampling a range of extinction and geometry parameters. `fake` outputs the effective temperature, surface gravity, and metallicity for each star in the CMD. We input these into `syncmd` which uses the BEAST to compute the associated stellar spectra in order to correctly apply extinction to the models. We redden the stellar spectra by applying a G03 SMC Bar R_V=2.74 extinction law. The BEAST then extracts the integrated band fluxes and computes synthetic *HST* photometry which we can compare to the observations. Through `syncmd` we use the BEAST to add observational noise and completeness to the model CMD (see Sec. 3.3.1).

Following Dalcanton et al. (2015), the log-normal distribution has a median extinction $\widetilde{A_V}$ and a dimensionless width $\widetilde{\sigma_{A_V}}$. The (normal) mean A_V is related to the median $\widetilde{A_V}$ and $\widetilde{\sigma_{A_V}}$ of the log-normal by:

$$\langle A_V \rangle = \widetilde{A_V} e^{\widetilde{\sigma_{A_V}^2}/2} \tag{3.1}$$

The width of the log-normal, $\langle \sigma_{A_V} \rangle$, can be related to $\widetilde{\sigma_{A_V}}$ by:

$$\langle \sigma_{A_V}^2 \rangle = \widetilde{A_V}^2 \, e^{\widetilde{\sigma_{A_V}^2}} (e^{\widetilde{\sigma_{A_V}^2}} - 1) \tag{3.2}$$

or in an alternate way as in Sec. 3.1 of Dalcanton et al. (2015). The range of extinction parameters is shown in Table 3.3.

It is also possible to vary the extinction curve, but since we are modeling CMDs only with the optical color *F475W − F814W*, we are not sensitive to the difference between an SMC and a MW extinction curve (see discussion in the Appendix). Thus we model our CMDs with the extinction law fixed to the G03 SMC Bar extinction curve, which is one of the reasons we focus on this color combination. In future work we plan to expand this technique to multiple color combinations and vary the extinction curve as well.

3.3.4   Modeling the 3D Geometry

We apply distance and geometry offsets using the `syncmd` code in the following way: We use the unreddened, single-distance CMD which we obtain from the SFH work and apply a random Gaussian distance distribution to the stars with a width σ_{DM}. We then place a single thin dust layer at a specified position and find which stars are foreground and background to the dust, and redden the stars behind the dust as described in Section 3.3.3.

We consider two contributions to the three-dimensional geometry which impact the SMIDGE CMD: the depth along the line of sight of the stellar component and the relative offset between the stars and a thin dust layer. We could assume that the stellar density follows one of a number of distributions such as a Gaussian, a log-normal, an exponential, etc. Subramanian & Subramaniam (2009) find that the spread in color and magnitude of red clump stars in the central region of the SMC (covering 2.5 square degrees, which includes the SMIDGE region) is best fit with a Gaussian. Using Cepheid observations to study the 3D structure of the SMC, Jacyszyn-Dobrzeniecka et al. (2016) also find a Gaussian-like distance distribution for the galaxy.

Our model also assumes a Gaussian stellar distribution along the line of sight (centered at a mean distance of μ=19.07 mag) with a FWHM between 3.5-19.8 kpc which spans the range found by previous observations. We can easily adapt this model to explore a variety of stellar density distributions in the future.

In our model, we assume the dust is in a thin layer relative to the stellar distribution. We can test this assumption with a population of stars which is distributed uniformly and independently of the dust layer. RGB stars can serve this purpose since they are evolved stars and would be distributed regardless of the location of the dust layer. Indeed, we do not see RGB stars covering the full range of possible extinctions, but rather we see a bimodal RGB which indicates that stars are essentially either unreddened or reddened, placing them either in front of or behind a thin dust layer. If the dust layer had a substantial thickness relative to the stellar distribution, this clear bimodality would not be evident. From stellar counts in the reddened and unreddened RGB, we conclude that the reddened fraction is $> 50\%$. We thus consider only dust layer positions closer to us than the centroid of the stellar distribution, as specified in Table 3.3.

3.3.5   Comparing Model and Observed CMDs

We generate a grid of model CMDs for each dust and geometry parameter combination from Table 3.3 for a total of 12,000 models. To compare each model CMD to the SMIDGE observations, we calculate the probability that a model produces the observations by comparing the number of stars in the respective CMDs in a way which is sensitive to CMD features (described below). This calculation results in the probability density as a function of each dust extinction and geometry parameter, or a combinations of parameters. The probability density function (PDF) can in turn inform us about the confidence interval for each parameter based on a set probability threshold.

To compare the number of stars in the model and data CMDs, we bin each model CMD in an identical way to the observed CMD and calculate the probability, from a Poisson distribution, that a model with a predicted number of stars n_i produces an observed m_i stars in bin i:
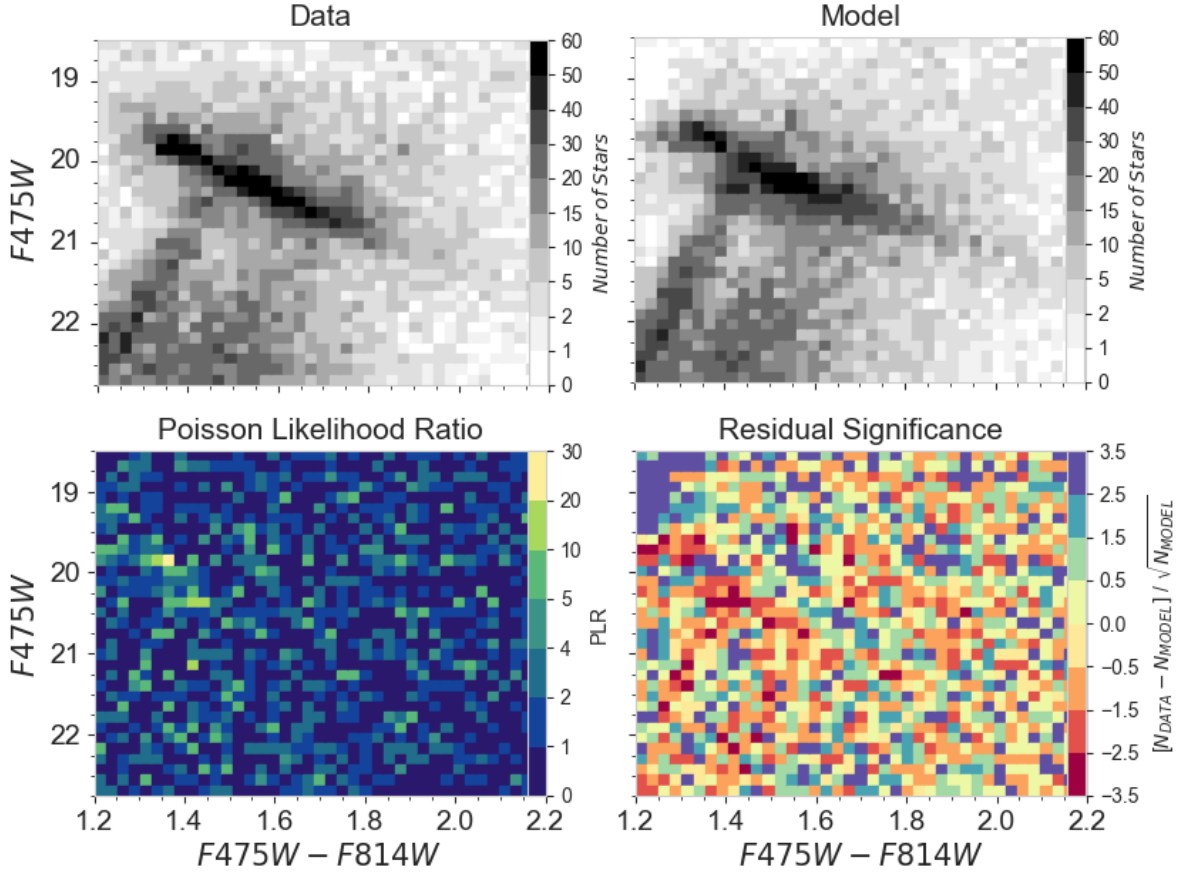
Figure 3.6. CMD matching of the SMIDGE color-magnitude diagram with a focus on the red clump and the red giant branch. Top: The SMIDGE observations and the best-fit model are binned in a Hess diagram to show the density of sources according to the binning scheme used in our CMD fitting. Top left: the SMIDGE data as in Figure 3.2. Top right: the best fit maximum probability model obtained as in Section 3.3. Bottom left: Poisson Likelihood Ratio map shows the PLR calculated for each CMD bin using Equation. 3.3.5. Bottom right: Residual significance map showing the difference in the number of sources between data and model weighted by the uncertainty in the model measurement. The best-fit model in the upper right has the following parameters: dust-stars offset of 0.10 mag, 1σ distance modulus spread of 0.15 mag, dust extinction with a log-normal median $A_V = 0.33$ mag, and width $\sigma_{A_V} = 0.65$.

$$P_i = \frac{m_i^{n_i}}{e^{m_i} n_i!} \tag{3.3}$$

We follow the recommendation of Dolphin (2002, 2013) who suggest that in the case of binned CMD data, the Poisson probability distribution should be used instead of the canonical Gaussian distribution, e.g. as in χ^2 minimization (Mighell, 1999). The results for all CMD bins are multiplied to obtain the total probability for each model-data comparison.

The probability can be measured for any binning of the CMD in color and magnitude. There are several considerations to take into account when defining the binning. First, if there are features in the CMD which we would like to be sensitive to, we must choose binning sufficiently small such that these features are preserved. For our purposes, we want to be sensitive to features such as the unreddened and the reddened RC, the tip of the RGB, and the unreddened RGB, among others. The smallest (narrowest) of these features is the unreddened RGB (which spans $\sim$ 0.1 mag in color) and the unreddened RC (spanning $\sim$ 0.5 mag in magnitude). Second, we also make sure that our bins are not too small that we end up with a significant number of bins (≥ 5 %) containing no sources. Finally, we must choose either uniform binning, where all CMD bins are of equal rectangular size, or irregular binning, to fit parts of the CMD in a bin of a special size if we have a sense for known errors or uncertainties in the data. Here we follow D02 in choosing uniform binning. Our final bin size is 0.025 mag in color and 0.125 mag in magnitude, which finely samples the CMD features of interest while minimizing the number of empty bins. With our SFH analysis in Section 3.3.2 we ensure that the difference in the total number of stars in the RC/RGB region between the SMIDGE CMD and each model CMD is insignificant. The variation in this number due to noise in each model CMD is addressed in Section 3.3.6.

The model with the highest probability is our best-fit model. To visualize the goodness of fit per bin, it is convenient to calculate a maximum likelihood statistic based on this probability. Similarly to D02 who applied this statistic to find the best star formation history for nearby

galaxies, we calculate the Poisson likelihood ratio (PLR) for each model-data comparison. Many studies use the PLR for CMD fitting, primarily to analyze SFHs (Dolphin, 1997; Aparicio et al., 1997; Dolphin, 2002; Harris & Zaritsky, 2009; Weisz et al., 2011). The PLR is defined as the ratio of the probability of drawing n_i stars from model m_i to the probability of drawing n_i stars from model n_i and has the following form:

$$PLR_i = \frac{m_i^{ni} e^{n_i}}{n_i^{ni} e^{m_i}} \tag{3.4}$$

We simulate distance, dust extinction and observational noise simultaneously on our unreddened synthetic CMDs and then measure the degree of match. In this sense our synthetic model CMD is stochastically sampled, and to calculate the likelihood - $L(n_1, n_2)$ - that two samples, n_1 and n_2, come from the same underlying model, m, we use:

$$L(n_1, n_2) = \int_0^\infty \frac{m^{n_1}}{e^m n_1!} \frac{m^{n_2}}{e^m n_2!} dm = \frac{0.5^{(n_1+n_2+1)}(n_1+n_2)!}{n_1! n_2!} \tag{3.5}$$

The equivalent PLR for this expression when n_1 is the observed data and n_2 is the model is (see Sec. 2.3 of D02 for details):

$$-2\ln PLR = -2\ln \frac{L(n_1, n_2)}{L(n_1, n_1)} \tag{3.6}$$

We sum the log of the PLR for all bins to obtain a total PLR for each model-data comparison.

The best-fit maximum probability model and the corresponding PLR results per bin are shown in Figure 3.6. The residual significance measures the fit quality by subtracting the model from the observed CMD and dividing this difference by the uncertainty in the model count,

76

$(n-m)/\sqrt{m}$. This result is simply the residual in units of standard deviation (e.g., a value of $+1$ or -1 is a 1σ outlier). There is a very good agreement between the overall number of stars in the RC/RGB CMD, but some weaknesses in the match are evident. The overestimated contribution of the horizontal branch (HB) discussed in Section 3.3.2 can be seen just below the red clump in both the CMD data-to-model comparison (as a slight bulge) and in the residual significance map (as a red patch). One consequence of this HB overestimate is the appearance of a "dip" in the reddened model RC (near the location of the unreddened RGB) even though the measured RC slopes of the data and the best fit model are nearly identical. The steeper model RGB slope is another potential consequence of this contribution. Both the PLR and the residuals maps show a poor match (an overestimation) in the number of (reddened and unreddened) RC stars which may have to do with the overestimation of the number of stars in the HB. In the Appendix we also show examples of models which are bad fits to the data.

3.3.6   The Probability Density Function and Uncertainties in the Results

Each model CMD is subject to two main sources of uncertainty. One is a result of number statistics due to the small number of stars in each CMD bin. Additionally, each CMD contains an intrinsic uncertainty in the stellar positions due to the random photon noise and crowding effects (simulated by the BEAST). These effects result in an inherent variability in the model predictions when a model is generated multiple times with the same set of parameters.

We generate synthetic CMDs over a well-sampled evenly-spaced grid of models based on the ranges of geometry and dust extinction parameters in Table 3.3. To account for the sources of uncertainty above, we generate each CMD in the grid 50 times and calculate the average number of stars per CMD bin. Each model is fit to the data by the process in Section 3.3.5. The repeated trials average out the noise.

In addition to finding the best-fit model (see end of Section 3.3.5), we also calculate the median and the confidence intervals of the 1-dimensional PDFs of each parameter. We define the 50th percentile of the cumulative probability as the PDF median, and the 16-84th percentile

77
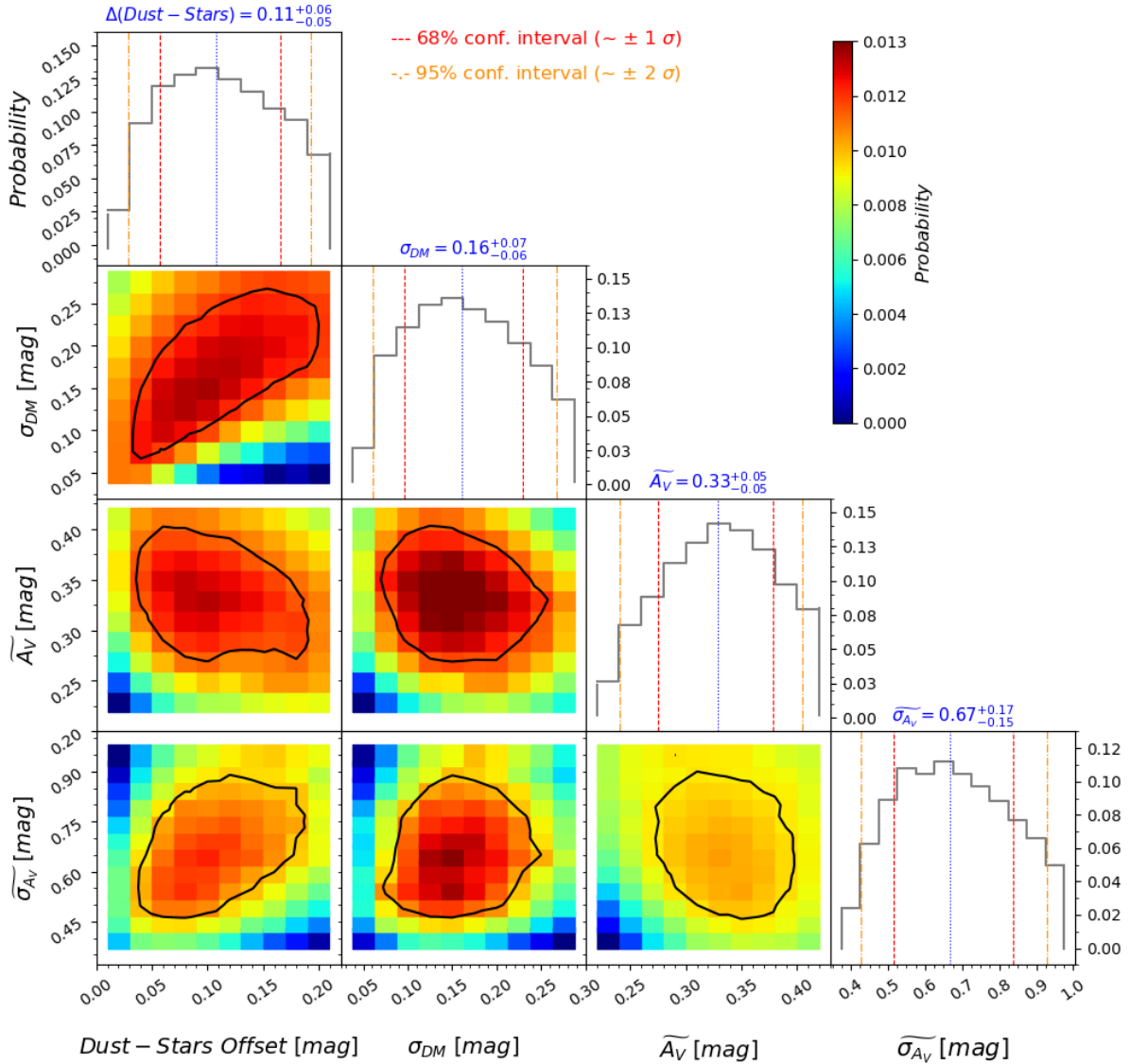
Figure 3.7. 1D and 2D probability distribution functions based on CMD matching results for the 3D geometry and dust extinction of the SMIDGE field. The 1D 68% and 95% confidence intervals fall between the red dashed and orange dot-dashed lines, respectively. The 50% probability threshold shown in dotted blue indicates the most likely value of the corresponding parameter. If the PDF followed a normal distribution, then the 68% confidence interval would be equivalent to $\pm 1\sigma$ uncertainty and the 50% blue line would indicate the mean. 2D probability distribution functions show the correlation among the geometry and extinction parameters. The black contours represent the 2D 68% confidence interval threshold.

Table 3.4. SMIDGE 3D Structure and Dust Extinction Results

Parameter	PDF 50% median and 68% confidence intervals	
Dust - stars offset	$0.11\,{}^{+0.06}_{-0.05}$ mag;	$3.22\,{}^{+1.69}_{-1.44}$ kpc
Distance modulus spread, σ_{DM}	$0.16\,{}^{+0.07}_{-0.06}$ mag;	FWHM $\approx$ 11.3 kpc
Reddened fraction, f_{RED}	$0.73\,{}^{+0.13}_{-0.13}$	
Extinction log-normal, A_V	$\widetilde{A_V} = 0.33\,{}^{+0.05}_{-0.05}$ mag;	mean $\langle A_V \rangle = 0.41 \pm 0.09$ mag
Extinction log-normal width, σ_{A_V}	$\widetilde{\sigma_{A_V}} = 0.67\,{}^{+0.17}_{-0.15}$	mean $\langle \sigma_{A_V} \rangle = 0.09 \pm 0.003$

Note. — The dust layer is on the near side of the stars. The log-normal median $\widetilde{A_V}$ and $\widetilde{\sigma_{A_V}}$ are converted into the mean (normally-distributed) $\langle A_V \rangle$ and $\langle \sigma_{A_V} \rangle$ using Eqns. 3.1-3.2.

confidence interval threshold as a measure of the PDF width (68% around the median), or the uncertainty in our results, informing us of the range of parameter values which contains the corresponding proportion of the probability. If the probability distribution were Gaussian, then the 68% confidence interval would correspond to $\pm$ one standard deviation, σ, and the 50th percentile would correspond to the mean. The results of this analysis are shown in Figures 3.7 and 3.8.

To obtain a 1D PDF for each parameter, we marginalize over all other parameters after one step of renormalizing. In this step, we assume that the probability of a model outside the grid is ~ 0, thus we cover a total probability of 1 in the grid, where each model is normalized accordingly. We marginalize over various dimensions of the grid to produce 1-D and 2-D PDFs for each parameter and parameter pair. In this way we can find desired confidence intervals for our parameters.

3.4 Results

The results for the 3D geometry and dust extinction parameters and their 68% confidence interval thresholds are presented in Table 3.4 and Figures 3.7 and 3.8. We find that the dust layer is offset on the near side of the centroid of the stellar distribution by $3.22\,{}^{+1.69}_{-1.44}$ kpc, and that the CMD is best fit with a stellar distribution along the line of sight with a 1 σ width of $0.16\,{}^{+0.07}_{-0.06}$
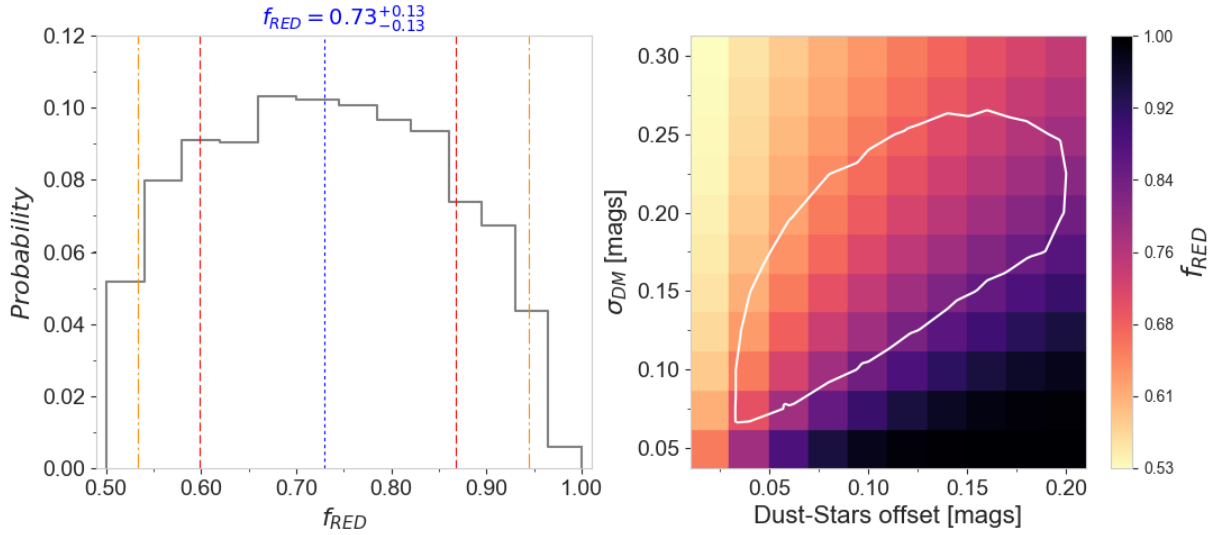
Figure 3.8. The result of the SMC 3-dimensional structure on the reddened fraction, f_{RED}, in terms of the relationship between the spread in the stellar distribution and the location of the dust layer relative to the stars. As expected, f_{RED} increases as the dust is farther removed from the stars (on the near side) while the stellar distribution remains compact. Lines of constant reddened fractions align with the white 68% confidence interval contours of the dust-stars offset and σ_{DM} 2D PDF in Fig. 3.7. The observations indicate $f_{RED}=0.73^{+0.13}_{-0.13}$. (See Sec. 3.4.)

mag, or an equivalent FWHM of 11.3 kpc. The reddened fraction of stars is $f_{RED}=0.73^{+0.13}_{-0.13}$ with the dust on the near side of the stellar midplane. The log-normal of dust extinction has a median of $\widetilde{A_V}=0.33 \pm 0.05$ mag and width $\widetilde{\sigma_{A_V}}=0.67^{+0.17}_{-0.15}$. This corresponds to a mean $A_V = 0.41$ mag and a width $\sigma_{A_V} = 0.097$ (where the foreground $A_V = 0.18$ mag applied to model the SFH is not a part of this result, thus it is solely attributable to SMC dust.).

There is a lack of strong correlation between the geometry and the extinction parameters in the fitting procedure. In particular, $\widetilde{A_V}$ and $\widetilde{\sigma_{A_V}}$ do not appear correlated with the dust-stars offset or the line-of-sight depth. The interpretation of this result is that since stars lie either in front of or behind the thin dust layer, they experience either all of the dust column or none of it (as discussed in Section 3.3.3). The geometrical arrangement of the stars and the dust is therefore independently constrained from the extinction properties of the dust layer.

Figure 3.7 and Figure 3.9 show that all parameters are well-constrained. Figure 3.9 shows a slice through the multidimensional grid, with all parameters held fixed at their best-fit values

from Section 3.3.5, aside from the value on the x-axis. Both figures show that small values of the line-of-sight depth, σ_{DM}, are strongly ruled out.

One of the most strongly constrained parameters from the observations is f_{RED}, which can be found simply from counts of RGB stars in the unreddened and reddened branches. f_{RED} is a purely geometrical effect which results from the relative arrangement of the dust-stars offset and the stellar distribution along the line-of-sight (σ_{DM}). The correlation between the line-of-sight depth and the dust-stars offset is the strongest among all the parameters. f_{RED} can be predicted theoretically from the relationship between σ_{DM} and the dust-stars offset as illustrated in the right-hand panel of Figure 3.8. Regions of constant f_{RED} indicate that the closer the dust layer is to the centroid of the stellar distribution, the smaller the line-of-sight depth required to preserve the same reddened fraction. Indeed, the 68% confidence intervals of of the dust-stars offset - σ_{DM} 2D PDF trace lines of constant f_{RED}. Our results for $f_{RED} = 0.73^{+0.13}_{-0.13}$ are consistent with the 68% confidence interval.

3.5 Discussion

Our two main findings about the SMC galactic structure are that the SW bar of the galaxy shows a significant spread in the distribution of stars along the line of sight of more than 10kpc FWHM, and also that the dust layer, which is clearly observed from its extinction effects, is offset from the centroid of the stars on the near side of the SMC. We obtained a similar result for the line-of-sight depth (10 ± 2 kpc) in YMJ17 employing a simple model for the reddened RC which helped explain the observed offset in the extinction curve in the SMC and the LMC.

Our line-of-sight depth finding is consistent with a number of other studies of the SMC structure employing various methods which generally suggest that the SMC is significantly elongated along the line of sight. Depending on the region studied and the method used, results vary and indicate galactic depths of less than 10 kpc and up to ~ 23 kpc in the outer regions of the galaxy (Hatzidimitriou & Hawkins, 1989; Gardiner & Hawkins, 1991; Harris & Zaritsky,
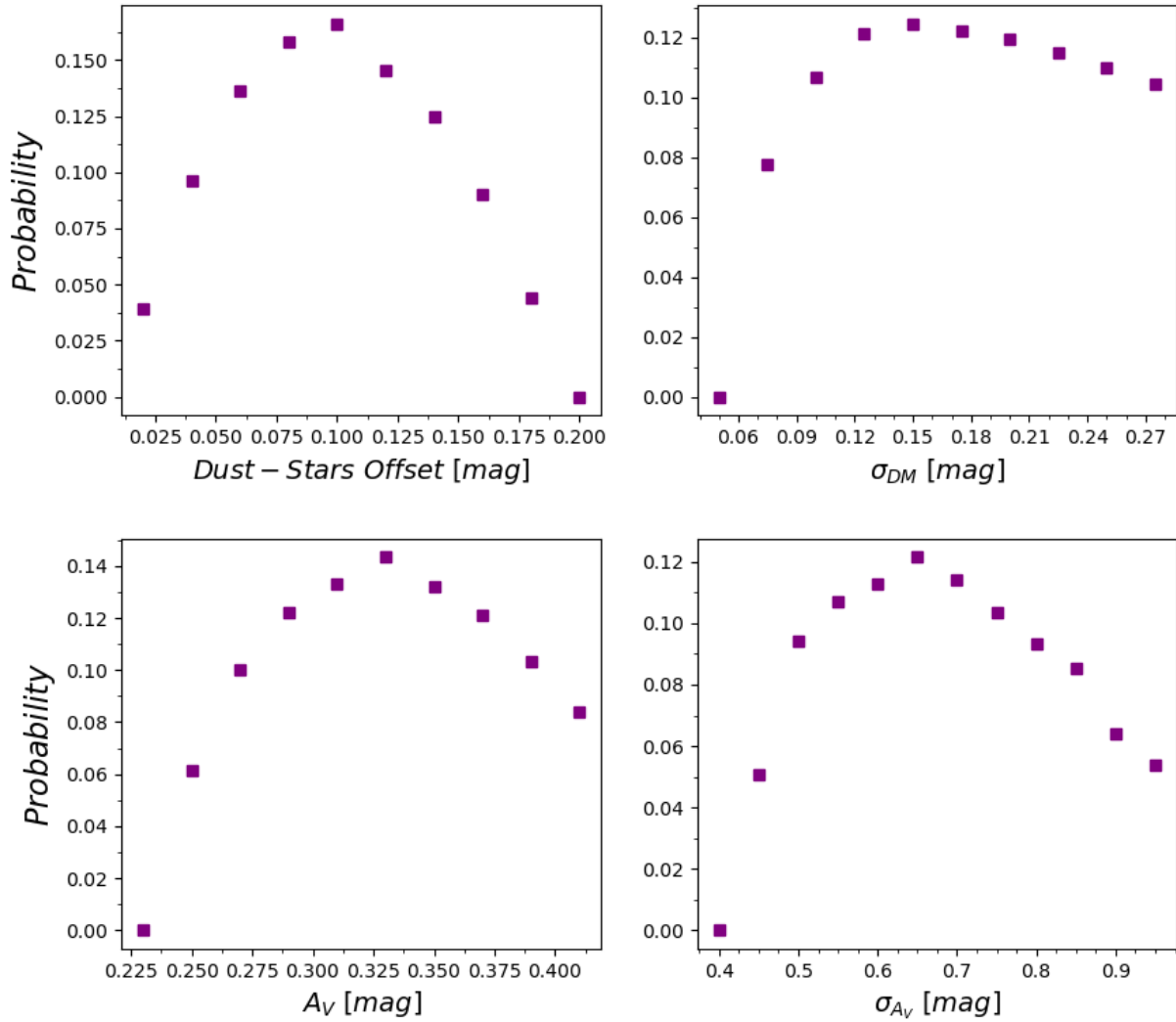
Figure 3.9. Model grid slices in multidimensional space showing the relationship between the best-fit CMD model parameters. The relative probability is shown for the model corresponding to each parameter value on the x-axis where the rest of the parameters for this model are at the best-fit values.

2004; Subramanian & Subramaniam, 2009, 2012; Nidever et al., 2013; Rubele et al., 2018; Muraveva et al., 2018).

Distance tracers show a number of features in the SMC, such as a distance gradient, galactic depth, and a distance bimodality. The distance gradient observed generally suggests that the eastern regions are closer than the western ones (Jacyszyn-Dobrzeniecka et al., 2016; Subramanian & Subramaniam, 2012; Ripepi et al., 2016; Subramanian et al., 2017; Muraveva et al., 2018). The galactic depth has been observed by finding the distribution of RR Lyrae and Cepheid variables (Harris & Zaritsky, 2004; Kapakos & Hatzidimitriou, 2012; Haschke et al., 2012; Jacyszyn-Dobrzeniecka et al., 2016; Muraveva et al., 2018) and the luminosity dispersion of red clump stars (Gardiner & Hawkins, 1991; Nidever et al., 2013; Subramanian et al., 2017). Using the latter also shows a distance bimodality (Subramanian et al., 2017) with two distinct bodies of stellar structures in the eastern regions of the galaxy. Although we do not study the distance gradient here, we note that the distance modulus we find via CMD matching discussed in Section 3.3.2 of μ=19.07 mag indicates that the SMIDGE region in SMC SW Bar is offset from the center of the SMC which is found to be at a distance modulus of μ=18.96 mag (Scowcroft et al., 2016), consistent with the studies above in that it indicates the western region is farther away.

A significant line-of-sight depth is also consistent with an LMC/SMC interaction. Numerical models for the SMC and the LMC indicate that the SMC geometric features, as well as the internal kinematics of the Magellanic Clouds, can be explained by repeated interactions between the two galaxies (Besla et al., 2012, 2016). The models of Besla et al. (2012) show that ram pressure decreases the velocity of the SMC's ISM and plays a role in modifying the properties of the ISM distribution, such as its location and velocity. Our observations that the dust layer is thin and results that the dust is positioned on the near side of the SMC relative to the stellar centroid (therefore placing the dust nearer the LMC as well) may be an expected consequence of such a ram pressure effect. Choi et al. (2018) measured the dust reddening and 3D structure of the LMC using RC stars and discovered a new stellar warp toward the SMC in the outer disk (and an

LMC line-of-sight depth of $\sim$7 kpc). It is clear from our study and others that the line-of-sight geometry of both Magellanic Clouds is complicated, due to their interactions.

We compare our CMD fitting result for the average SMIDGE dust extinction with A_V based on dust mass surface densities, Σ_{M_d}, derived from IR emission observations by the HERschel Inventory of The Agents of Galaxy Evolution (Gordon et al., 2014). We fit the IR dust SED with a modified black body dust emission model as in Chiang et al. (2018) to extract the average dust mass surface density in the SMIDGE footprint, and find $\Sigma_{M_d} = 1 \times 10^4$ M$_\odot$ kpc^{-2}. Using $A_V/\Sigma_{M_d} = 0.7394$ $mag/10^5 M_\odot$ kpc^{-2} from the Draine & Li model and from Draine et al. (2014), the IR-derived extinction is $A_V \approx 0.75$. This overprediction of the observed extinction - here by a factor of $\sim$ 2.3 - is consistent with other comparisons between IR-derived optical extinction results using the Draine & Li dust model and alternative extinction methods. Dalcanton et al. (2015) who use CMD fitting of RGB stars to derive the distribution of dust in M31 find that the dust model A_V estimates are too high by a factor of $\sim$ 2.5 when comparing their results to those of Draine et al. (2014). Similarly, Planck Collaboration et al. (2016) show a discrepancy of a factor of $\sim$ 2 in A_V estimates from all-sky Milky Way optical photometry of quasi-stellar objects. This discrepancy can be attributed to the Draine & Li model overestimating the dust mass from IR emission, which would imply that dust grains are more emissive than the model assumes. However, it is notable that M31 and the Milky Way are both at relatively high metallicity. Our comparison is among the first of its kind for a low-metallicity environment containing dust which potentially has very different properties.

Further SMC A_V comparison can be made with the work of Hagen et al. (2017) who use UV, IR and optical observations integrated into $200''$ regions to model the SMC SED and map A_V for the galaxy. Half of their SMC regions have a mean $A_V < 0.25$, with results for the SMIDGE region varying between $A_V = 0.2$ - 0.75 mag. Our results of mean $A_V = 0.41$ are on the high end which is expected since the SMIDGE field was specifically picked as one of the dustiest spots in the SMC. Our upcoming study will resolve the SMIDGE field into smaller regions which will allow for a better comparison with Hagen et al. (2017).

Dalcanton et al. (2015) studied the distribution of dust in M31 by modeling the NIR CMD of red giant branch stars to obtain results for the same set of dust and geometry parameters as the ones we explore here - $\widetilde{A_V}$, $\widetilde{\sigma_{A_V}}$, and f_{RED}. Although they approach modeling the RGB and RC quite differently for a number of reasons, they also observe an RGB broadening and a bimodality due to the combined effects of dust extinction and geometry, and rely on modeling these observed effects to form the basis of their conclusions. Their study explores regions in the star-forming disk of M31 which generally have a more widely-varying and a higher A_V than SMIDGE. They do not observe a correlation between A_V and f_{RED} at high extinctions (median $A_V \geq 1$ mag). A correlation between the two at lower extinctions is interpreted not as a physically-driven result, but rather as a result expected from their fitting approach (which relates f_{RED} to A_V through a "filling factor" describing the areas of the gas cloud and the analyzed pixel such that an increasingly smaller filling factor for dusty gas is due to a decreasing median extinction and also contributes to a decreasing geometric reddened fraction). At the lowest extinctions they observe, which are comparable to the extinctions we find in SMIDGE, (median $A_V \leq 0.3$ mag), the broadening of the RGB in their NIR CMDs is not significant, thus their do not have a strong constraint on f_{RED}.

The LMC, also know n to have an appreciable depth along the line of sight (Subramanian & Subramaniam, 2009) and a relatively low metallicity at 1/2 solar (Russell & Dopita, 1992), is another suitable target for this RC/RGB dust and geometry modeling technique. Our goal is to apply this same approach to data from the LMC METAL survey *HST* (Roman-Duval et al., 2019) to study dust extinction and geometry properties probing the LMC extinction curve and extinction distribution, and 3D structure.

3.5.1 Calculating A_V/N_H

We measure the average H column density in the SMIDGE field using HI observations from Stanimirovic et al. (1999) using the ATCA and Parkes telescopes and ^{12}CO J=(2−1) observations of the SW Bar with the APEX telescope (Rubio et al. in prep). We extract the

average integrated intensities of the HI and CO lines over the full coverage of the ACS imaging from SMIDGE. We convert the HI line integrated intensity to column density assuming no opacity correction. For H_2, we must adopt a CO-to-H_2 conversion factor. The behavior of the conversion factor as a function of metallicity is the subject of much investigation (Bolatto et al., 2013). For the SMC, X_{CO} has been found to be larger than the MW value of $X_{CO} = 2 \times 10^{20}$ cm^{-2} (K km s^{-1}) by a variety of studies (Leroy et al., 2011; Roman-Duval et al., 2014). The SMIDGE field is atomic gas dominated, so for a wide range of conversion factors N_H does not change dramatically depending on the conversion factor choice. We convert the CO (2-1) line to (1-0) using a $R_{21} = (2-1)/(1-0) = 0.7$ and we use X_{CO} values between the MW and 10 times the MW value to obtain N_{H2}, which we multiply by 2 to obtain N_H. We calculate a mean $\langle A_V \rangle = 0.41 \pm 0.09$ mag. The final range of N_H for SMIDGE is 9.7×10^{21} to 1.3×10^{22} cm^{-2}. This yields $\langle A_V \rangle / N_H = 3.2 - 4.2 \times 10^{-23}$ mag cm^2 H^{-1}. These values are substantially lower than the canonical MW $\langle A_V \rangle / N_H = 5.3 \times 10^{-22}$ (Bohlin et al., 1978; Rachford et al., 2009) by more than an order of magnitude. G03 measure the *HI* column density from the UV Lyα absorption profile for four sightlines in the SMC Bar and find $A_V / N_H = 7.7 \times 10^{-23}$ mag cm^{-2} H^{-1}, which is only a factor of ~ 2 higher than our result. Roman-Duval et al. (2014) measure a comparable ratio in the SMC using Herschel IR observations where they find the gas-to-dust ratio to be between 4 and ~ 10 times the MW value in the diffuse and dense ISM, respectively, depending on the methodology used.

3.6   Conclusions and Further Work

We model the dust extinction and 3D geometry properties of the SMIDGE field in the SW Bar of the SMC using the optical *F475W − F814W* CMD of RC and RGB stars. We find the following:

1. The distance modulus for the midpoint of the stellar distribution within the SMIDGE region is 65.2 kpc ($\mu = 19.07$ mag).

2. The CMD is best fit with a 1σ line-of-sight depth $\sigma_{DM} = 0.16\,^{+0.07}_{-0.06}$ mag, or an equivalent FWHM of 11.3 kpc.

3. The dust layer is offset on the near side of the stars by $3.22\,^{+1.69}_{-1.44}$ kpc and is located at a distance modulus of $\mu = 18.96$ mag (61.94 kpc).

4. The combination of dust position and stellar distribution results in a $73^{+0.14}_{-0.13}$ % reddened fraction of stars.

5. The distribution of dust extinction has a mean $\langle A_V \rangle = 0.41 \pm 0.09$ mag and width $\langle \sigma_{A_V} \rangle =$ 0.097 ± 0.003 mag (log-normal median $\widetilde{A_V} = 0.33^{+0.05}_{-0.05}$ mag and dimensionless width $\widetilde{\sigma_{A_V}}$ $= 0.67\,^{+0.17}_{-0.15}$).

The SMC's dust extinction curve is notably different from that of the Milky Way in terms of the lack of a strong 2175 Å bump and a steep rise in the UV (G03). Here we base our model grid on the G03 SMC Bar extinction law (R_V=2.74) as discussed in Section 3.3.3 since our 2017 work (YMJ17) showed consistency with the G03 results. To probe different extinction laws, including a potential extinction law mixture of SMC and Milky Way extinction curves (see Appendix), in subsequent work we will use multiple color combinations for a similar analysis, fixing the geometric parameters of the SMC at the values found here.

System bibliographic services. This research made use of Astropy, a community-developed core Python package for astronomy (Astropy Collaboration et al. 2013), NumPy (Van Der Walt et al. 2011), Matplotlib (Hunter 2007), the `syncmd` tool for BEAST-based post-processing of Synthetic Stellar Populations (C. Johnson), the BEAST (Bayesian Extinction and Stellar Tool; K. Gordon), and the `MATCH` CMD fitting software package (A. Dolphin). Chapter 3, in full, has been submitted for publication of the material as it may appear in The Astrophysical Journal, 2020, Yanchulova Merica-Jones, P., Sandstrom, K.M., Johnson, L.C., Dolphin, A.E., Dalcanton, J., Gordon, K., Roman-Duval, J., Weisz, D.R., Williams, B.F. The dissertation author was the primary investigator and author of this paper.

3.7 Appendix (Chapter 3)

We perform tests to determine the sensitivity of our technique to a number physical- and technique-specific factors in our attempt to measure quantities of interest.

Our sensitivity to the extinction law is limited since extinction curve differences in the optical part of the spectrum are small, and our analysis is based only on optical CMDs. We test how sensitive we are to differentiating between an SMC and a MW extinction curve by simulating CMDs with a mixture of an SMC-like G03 R_V=2.74 law and a Milky Way-like Fitzpatrick (1999) R_V=3.1 law. We do this by varying f_A, which is the fraction corresponding to the mixture between the two extinction laws (see Sec. 3.2 of G16). Although we see a trend of increasing PLR (worse match) as the model moves away from an SMC-like extinction, a pure Milky Way-like law is within the SMC noise model uncertainties. Thus we are not sensitive to the extinction law to a sufficient degree using the optical CMD only.

While Figure 3.6 shows our best fit model, here we show examples of bad model fits where all parameters are held fixed at their minimum-PLR values, except for one parameter which is fixed at a bad-fit value. The PLR and the residual significance plots show the mismatch clearly. The top panel of Figure 3.10 shows the result of placing the dust layer in the middle of

the stellar distribution causing a $\sim 50\%$ reddened fraction. We can see that both the RC and the RGB have an overdensitiy of stars which we do not see in the data.

The middle panel shows a model which underestimates the spread of the stars along the line of sight (FWHM = 5.3 kpc while our results point to a FWHM ≈ 11.3 kpc). We clearly see that the model lacks a sufficient number of unreddened stars extending to brighter magnitudes (which would result from a higher line-of-sight depth). Correspondingly, the model overestimates the number of reddened stars (calculated to be f_{RED}) since the smaller spread in the stellar distribution places a higher fraction of stars behind the dust (see Fig. 3.8).

It can be also seen that the slope of the reddened portion of the red clump is incorrect since a smaller galactic depth produces a shallower RC slope, and in our case a mismatch to the data. Indeed, the main measurement of our previous work (YMJ17), which used the slope of the reddened RC across multiple-color CMD combinations to measure the shape of the SMIDGE extinction curve, showed an offset from previous extinction curve measurements. This result was due to the measured steepness of the RC reddening vector which resulted in higher extinction values across all CMD combinations. Using a toy RC model to simulate an SMC depth, we showed that the offset was consistent with a stellar distribution with a FWHM = 10 ± 2 kpc along the line of sight.

The bottom panel of Figure 3.10 shows a model which underestimates the amount of dust by incorporating a distribution of dust extinctions with $\widetilde{A_V}$=0.1 (contrasted with our result of $\widetilde{A_V}$=0.3). This model also results in a reddened fraction f_{RED}=0.7, since the extinction has no bearing on the dust-stars geometry (and vice-versa) as discussed in Section 2.5. However, since $\widetilde{A_V}$ changes both the color and magnitude of stars, we can see the effect in both CMD dimensions for the RC and the RGB as they tend to be closer to their unreddened positions (see the left panel of Figure 3.3).
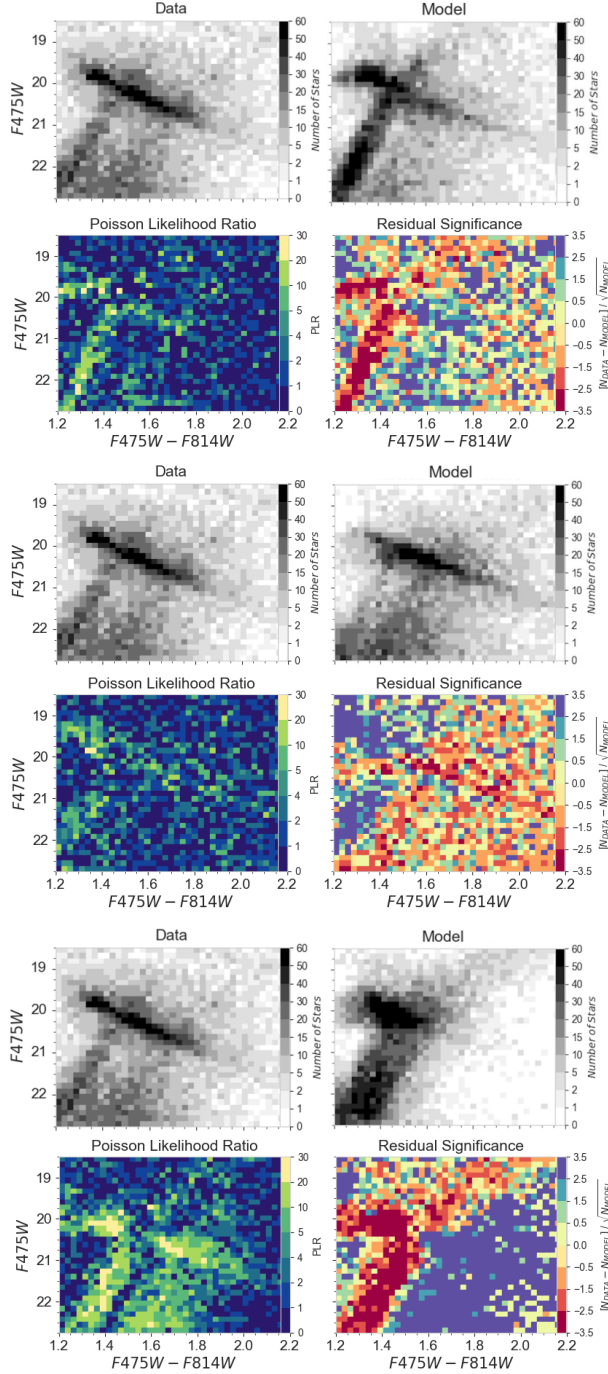
Figure 3.10. Examples of bad model fits where all except for one parameters are at their best fit value listed in Sec. 3.4. a) Dust layer is aligned with the center of the stellar distribution causing a 50% reddened fraction. b) The spread of the stellar distribution is 1/2 of its best-fit value (σ_{DM}=2.25 kpc which results in a distribution with a FWHM = 5.3 kpc. c) The mean of the log-normal distribution of dust extinctions is A_V=0.1 mag.)

Chapter 4

Summary and Future Work

4.1   Summary of Results and Conclusions

Photometric Hubble Space Telescope observations of the SMC SW Bar from the SMIDGE survey are used to construct color-magnitude diagrams of evolved red clump and red giant branch stars to study the SMC dust extinction and galactic geometry properties. The two main techniques used are: 1) Measurement of the red clump extinction vector from the multiband CMD and modeling the SMC depth along the line of sight as discussed in Chapter 2, and 2) Modeling the dust extinction and 3D geometry properties of red clump and red giant branch stars using optical CMDs (see Chapter 3).

The main conclusions are the following:

1. Results for the shape of the SMC optical and near-infrared portions of the extinction curve, together with a model for the SMC depth along the line of sight, show consistency with the SMC extinction curve measurements of individual stars from UV spectroscopy of Gordon et al. (2003). This consistency may be due to one of two possibilities: 1) There is little variation in the extinction curve over a relatively large area in the SMC, or 2) Both UV spectroscopy and multiband photometric SMIDGE measurements sample the same (diffuse) ISM phases.

2. A similar consistency is observed between the 30 Doradus LMC extinction curve measured

91

in this work and Gordon et al. (2003) UV spectroscopy results.

3. Both the SMC and the LMC show a significant galactic depth along the line of sight inferred from modeling the red clump reddening vector: 10 ± 2 kpc for the SMC and 5 $\pm$ 1 kpc for the LMC measured at the 90% confidence level. These results are consistent with recent studies using a variety of stellar populations (RR Lyrae, Cepheids, and Red Clump stars).

4. When the Magellanic Clouds' galactic depth along the line of sight if accounted for, "gray" extinction is not necessary to explain the observed offsets in the extinction curves measured from the slope of the RC reddening vector (in contrast with conclusions by De Marchi et al. (2016)). Gray dust would suggest the presence of fresh large grains due to Type II supernova explosions, which would indicate a bias towards gray extinction for galaxies with high star formation rates. While there is observational evidence for the presence of gray extinction, it is not needed in the LMC and the SMC case to explain the extinction curve.

Modeling the dust extinction and 3D geometry properties of the SMIDGE field using the optical $F475W - F814W$ CMD of RC and RGB stars yields the following:

5. The distance modulus for the centroid of the stellar distribution within the SMIDGE region is 65.2 kpc (distance modulus $\mu = 19.07$ mag). This suggests that the SMC SW Bar is offset by ~3.2 kpc on the far side from the average SMC distance as measured by Cepheids.

6. The SMIDGE CMD is best fit with a 1σ line-of-sight depth, $\sigma_{DM} = 0.16\,^{+0.07}_{-0.06}$ mag, or an equivalent FWHM of 11.3 kpc. This RC/RGB CMD fitting result shows a stellar distribution wider by 1.3 kpc than the distribution obtained from modeling red clump stars only.

7. The dust layer is offset on the near side of the stars by $\Delta_{DUST} = 3.22\,^{+1.69}_{-1.44}$ kpc and is located at a distance modulus of $\mu = 18.96$ mag (61.94 kpc).

8. The combination of dust position and stellar distribution results in a $73^{+0.14}_{-0.13}$ % reddened fraction of stars. This is a refined measurement from the rough estimate in Chapter 2 used to model the red clump ($f_{RED} = 0.65$).

9. The distribution of dust extinction has a mean $\langle A_V \rangle = 0.41 \pm 0.09$ mag and width $\langle \sigma_{A_V} \rangle = 0.097 \pm 0.003$ mag (median $\widetilde{A_V} = 0.33^{+0.05}_{-0.05}$ mag and dimensionless width $\widetilde{\sigma_{A_V}} = 0.67^{+0.17}_{-0.15}$).

10. We measure the ratio of the extinction per hydrogen column density A_V/N_H in the SMC SW Bar to be $\langle A_V \rangle/N_H = 3.2 - 4.2 \times 10^{-23}$ mag cm^2 H^{-1}. These values are substantially lower than the canonical MW $\langle A_V \rangle/N_H = 5.3 \times 10^{-22}$ by more than an order of magnitude, and are consistent with other SMC $\langle A_V \rangle/N_H$ measurements (Gordon et al., 2003; Roman-Duval et al., 2014). This result has implications for calculating the CMD extinction-based dust mass and the interpretation of the far-IR emission at low-metallicity.

4.2   Future Work

The SMIDGE survey aims at mapping the spatially-resolved extinction curve properties A_V and R_V at low metallicity in the Small Magellanic Cloud. The use of color-magnitude diagrams modeling has proven to be a powerful technique to understand the average extinction curve properties. Further, the SMC 3D geometry has been incorporated as a fundamental aspect of the CMD models. While primarily aimed at measuring the extinction, the models have shown that any SMC (and indeed, LMC) CMD-based extinction measurement has to go hand-in-hand with constraining the galactic geometry along the line of sight.

The dust extinction and 3D geometry parameters for the SMC Bar found in Chapter 3 will serve to derive a refined measurement of the average SMC extinction curve and to map the spatial variation in R_V and A_V. Theoretically there are a number of ways to approach mapping spatial variations in the dust extinction. An immediate idea would be to select SMIDGE subregions and use CMD matching of the RC and RGB as in Chapter 3 while we also vary the extinction

curve, R_λ to find a best-fit. There is one fundamental challenges with this approach. Tests show that we are not able to be sufficiently sensitive to different values of R_λ when the number of stars on the CMD, and consequently in the RC/RGB, decreases due to a subselection from the full SMIDGE CMD. This happens because small-number statistics are already inherent in our Poisson probability/likelihood CMD-binning approach (see Sec. 3.3.5).

We can, however, approach the problem in a slightly different way. In short, since we now have a more accurate measurement of the galactic geometry and all dust extinction parameters of interest except for R_λ, we can hold the known parameters fixed while the full SMIDGE CMD is fit by varying the extinction curve, R_λ, across photometric bands for a refined average measurement.

The galactic geometry in terms of the depth along the line of sight, σ_{DM}, and the dust-stars offset, Δ_{DUST} is not expected to vary across the SMIDGE field. There is evidence that due to its dynamical nature, the SMC is composed of overlapping substructures of gas and dust (Besla et al., 2012; Murray et al., 2019). While the dust layer may be patchy and composed of multiple layers, there should also be no major variation in the offset between the dust and the centroid of the stellar distribution.

Very likely the same is valid for the distribution of extinctions A_V and the width σ_{A_V}. If this is the case, we can assume that these quantities also do not vary significantly across the SMIDGE field. To examine the type of environment in the SMIDGE area, in Chapter 2 we calculated the fraction of stars found along lines of sight towards dense molecular gas regions. We found that our survey area is dominated by the diffuse ISM, where 77% of red clump stars sample lines of sight outside dense molecular gas regions. Additionally, the Gordon et al. (2003) SMC Bar A_V extinctions of 0.35 - 0.68 indicate that their sightlines also probe the diffuse ISM where coagulation and grain growth are unlikely to have happened.

Holding σ_{DM}, Δ_{DUST}, A_V, and σ_{A_V} constant we will then fit the SMIDGE CMD across the full range of color-magnitude combinations afforded by the HST multiband photometry. This will allow for an independent non-parametrized extinction curve measurement which does not

assume an existing form (as it does in the analysis in Chapter 3). There are some important considerations to be made in this analysis. First, we will have to ensure that the SMIDGE star formation history (SFH) derived using the optical $F475W - F814W$ CMD is applicable to the full range of UV-IR CMDs. A coarse CMD fitting test using the current SFH can be made in other magnitude combinations where all geometry and dust extinction parameters are varied again to check the consistency among UV-IR CMDs likelihood results. Second, we must find a suitable R_λ grid spacing such that we can convert our results into the more commonly-used extinction curve parametrization such as R_V. Next, we will have to consider how to most accurately (and efficiently) measure the joint CMD probability across photometric bands and how to account for the joint uncertainty. We may consult how this is done in SFH studies which may also use multiband CMDs to derive the star formation rates and stellar metallicities at a certain age.

This measurement will in effect again be aimed at finding changes in the slope of the red clump reddening vector on a CMD which directly traces R_λ.[1] However, this time the analysis will be done by a RC/RGB CMD fitting with a pre-existing knowledge of the precise values for the geometry and the extinction parameters.

An additional goal is to use SED fitting to measure the UV shape of the extinction curve in the SMC SW Bar along the line of sight. Right now we can not say much about this part of the extinction curve due to a systematic uncertainty in R_{225} from *HST's F225W* known red leak problem.[2] At the same time some of the most interesting extinction curve features such as the 2175 Å bump and the steep UV rise are in this part of the spectrum.

We can examine UV-bright stars behind dust so that we can use our 9-band photometry and fit the spectral energy distribution for each individual star to SED models incorporating dust extinction parameters. This approach will allow us to separate the stellar from the dust properties so that we can observe the intrinsic spectrum of dust on a star-by-star basis. This can be accomplished with the full functionality of the Bayesian Extinction and Stellar Tool (BEAST;

---

[1]$R_\lambda = A_\lambda / (A_{\lambda'} - A_{\lambda''})$, where $A_{\lambda'} - A_{\lambda''}$ is the extinction in a chosen color combination

[2]The red leak affects the measured stellar magnitudes in *F225W* by contributing to an off-band flux in the red part of the spectrum (Dressel, 2014).

Gordon et al. (2016)) which we use in Chapter 3 to model the observational noise on our CMDs. The BEAST is designed for use on photometric measurements and applies probabilistic Bayesian SED models to derive the physical properties, such as the mass, age, and the metallicity, and the dust parameters (dust grain composition and size distribution, and dust column density).

The BEAST can be used at all wavelengths supplied by the photometric data, and as such it can be the key to mapping the spatial variability of R_V and A_V in the SMIDGE SW Bar. When this project is completed, it will have provided the most comprehensive distribution of extinction curves in the galaxy to date. These results will be key to understanding what "SMC-like" extinction means, and where the SMC extinction law can be applied. With a better understanding of the detailed properties of dust in high-redshift / low-metallicity galaxies we can have a better understanding of the evolution of these properties, and the evolution of the Universe itself through astrophysical processes in which interstellar dust plays a role.

Bibliography

Alves, D. R. 2000, K-Band Calibration of the Red Clump Luminosity, ApJ, 539, 732

Aparicio, A., Gallart, C., & Bertelli, G. 1997, The Stellar Content and the Star Formation History of the Local Group Dwarf Galaxy LGS 3., AJ, 114, 680

Asano, R. S., Takeuchi, T. T., Hirashita, H., & Inoue, A. K. 2013, Dust formation history of galaxies: A critical role of metallicity for the dust mass growth by accreting materials in the interstellar medium, Earth, Planets, and Space, 65, 213

Asplund, M., Grevesse, N., Sauval, A. J., & Scott, P. 2009, The Chemical Composition of the Sun, ARA&A, 47, 481

Astropy Collaboration, Robitaille, T. P., Tollerud, E. J., Greenfield, P., Droettboom, M., Bray, E., Aldcroft, T., Davis, M., Ginsburg, A., Price-Whelan, A. M., Kerzendorf, W. E., Conley, A., Crighton, N., Barbary, K., Muna, D., Ferguson, H., Grollier, F., Parikh, M. M., Nair, P. H., Unther, H. M., Deil, C., Woillez, J., Conseil, S., Kramer, R., Turner, J. E. H., Singer, L., Fox, R., Weaver, B. A., Zabalza, V., Edwards, Z. I., Azalee Bostroem, K., Burke, D. J., Casey, A. R., Crawford, S. M., Dencheva, N., Ely, J., Jenness, T., Labrie, K., Lim, P. L., Pierfederici, F., Pontzen, A., Ptak, A., Refsdal, B., Servillat, M., & Streicher, O. 2013, Astropy: A community Python package for astronomy, A & A, 558, A33

Besla, G., Kallivayalil, N., Hernquist, L., Robertson, B., Cox, T. J., van der Marel, R. P., & Alcock, C. 2007, Are the Magellanic Clouds on Their First Passage about the Milky Way?, ApJ, 668, 949

Besla, G., Kallivayalil, N., Hernquist, L., van der Marel, R. P., Cox, T. J., & Kereš, D. 2012, The role of dwarf galaxy interactions in shaping the Magellanic System and implications for Magellanic Irregulars, MNRAS, 421, 2109

Besla, G., Martínez-Delgado, D., van der Marel, R. P., Beletsky, Y., Seibert, M., Schlafly, E. F., Grebel, E. K., & Neyer, F. 2016, Low Surface Brightness Imaging of the Magellanic System: Imprints of Tidal Interactions between the Clouds in the Stellar Periphery, ApJ, 825, 20

Bohlin, R. C., Savage, B. D., & Drake, J. F. 1978, A survey of interstellar H I from Lalpha

absorption measurements. II., ApJ, 224, 132

Bolatto, A. D., Wolfire, M., & Leroy, A. K. 2013, The CO-to-H$_2$ Conversion Factor, ARA&A, 51, 207

Bovy, J., Nidever, D. L., Rix, H.-W., Girardi, L., Zasowski, G., Chojnowski, S. D., Holtzman, J., Epstein, C., Frinchaboy, P. M., Hayden, M. R., Rodrigues, T. S., Majewski, S. R., Johnson, J. A., Pinsonneault, M. H., Stello, D., Allende Prieto, C., Andrews, B., Basu, S., Beers, T. C., Bizyaev, D., Burton, A., Chaplin, W. J., Cunha, K., Elsworth, Y., García, R. A., García-Herńandez, D. A., García Pérez, A. E., Hearty, F. R., Hekker, S., Kallinger, T., Kinemuchi, K., Koesterke, L., Mészáros, S., Mosser, B., O'Connell, R. W., Oravetz, D., Pan, K., Robin, A. C., Schiavon, R. P., Schneider, D. P., Schultheis, M., Serenelli, A., Shetrone, M., Silva Aguirre, V., Simmons, A., Skrutskie, M., Smith, V. V., Stassun, K., Weinberg, D. H., Wilson, J. C., & Zamora, O. 2014, The APOGEE Red-clump Catalog: Precise Distances, Velocities, and High-resolution Elemental Abundances over a Large Area of the Milky Way's Disk, ApJ, 790, 127

Bressan, A., Marigo, P., Girardi, L., Salasnich, B., Dal Cero, C., Rubele, S., & Nanni, A. 2012, PARSEC: stellar tracks and isochrones with the PAdova and TRieste Stellar Evolution Code, MNRAS, 427, 127

Caldwell, J. A. R., & Coulson, I. M. 1986, The geometry and distance of the Magellanic Clouds from Cepheid variables, MNRAS, 218, 223

Calzetti, D., Kinney, A. L., & Storchi-Bergmann, T. 1994, Dust extinction of the stellar continua in starburst galaxies: The ultraviolet and optical extinction law, ApJ, 429, 582

Cannon, R. D. 1970, Red giants in old open clusters., MNRAS, 150, 111

Cardelli, J. A., Clayton, G. C., & Mathis, J. S. 1989, The relationship between infrared, optical, and ultraviolet extinction, ApJ, 345, 245

Cardelli, J. A., Sembach, K. R., & Mathis, J. S. 1992, The quantitative assessment of UV extinction derived from IUE data of giants and supergiants, AJ (ISSN 0004-6256), 104, 1916

Cartledge, S. I. B., Clayton, G. C., Gordon, K. D., Rachford, B. L., Draine, B. T., Martin, P. G., Mathis, J. S., Misselt, K. A., Sofia, U. J., Whittet, D. C. B., & Wolff, M. J. 2005, FUSE Measurements of Far-Ultraviolet Extinction. II. Magellanic Cloud Sight Lines, ApJ, 630, 355

Catelan, M. 2009, Horizontal branch stars: the interplay between observations and theory, and insights into the formation of the Galaxy, Astrophysics and Space Science, 320, 261

Chastenet, J., Sandstrom, K., Chiang, I. D., Leroy, A. K., Utomo, D., Bot, C., Gordon, K. D., Draine, B. T., Fukui, Y., Onishi, T., & Tsuge, K. 2019, The Polycyclic Aromatic Hydrocarbon

Mass Fraction on a 10 pc Scale in the Magellanic Clouds, ApJ, 876, 62

Chen, Y., Bressan, A., Girardi, L., Marigo, P., Kong, X., & Lanza, A. 2015, PARSEC evolutionary
    tracks of massive stars up to 350 M$_\odot$ at metallicities $0.0001 \leq Z \leq 0.04$, MNRAS, 452, 1068

Chiang, I.-D., Sandstrom, K. M., Chastenet, J., Johnson, L. C., Leroy, A. K., & Utomo, D. 2018,
    The Spatially Resolved Dust-to-metals Ratio in M101, ApJ, 865, 117

Choi, Y., Nidever, D. L., Olsen, K., Blum, R. D., Besla, G., Zaritsky, D., van der Marel, R. P.,
    Bell, E. F., Gallart, C., Cioni, M.-R. L., Johnson, L. C., Vivas, A. K., Saha, A., de Boer, T.
    J. L., Noël, N. E. D., Monachesi, A., Massana, P., Conn, B. C., Martinez-Delgado, D., Muñoz,
    R. R., & Stringfellow, G. S. 2018, SMASHing the LMC: A Tidally Induced Warp in the Outer
    LMC and a Large-scale Reddening Map, ApJ, 866, 90

Cignoni, M., Sabbi, E., Nota, A., Tosi, M., Degl'Innocenti, S., Moroni, P. G. P., Angeretti, L.,
    Carlson, L. R., Gallagher, J., Meixner, M., Sirianni, M., & Smith, L. J. 2009, Star Formation
    History in the Small Magellanic Cloud: The Case of NGC 602, AJ, 137, 3668

Clayton, G. C., & Martin, P. G. 1985, Interstellar dust in the Large Magellanic Cloud, ApJ, 288,
    558

Clayton, G. C., Wolff, M. J., Sofia, U. J., Gordon, K. D., & Misselt, K. A. 2003, Dust Grain Size
    Distributions from MRN to MEM, ApJ, 588, 871

Compiègne, M., Verstraete, L., Jones, A., Bernard, J. P., Boulanger, F., Flagey, N., Le Bourlot,
    J., Paradis, D., & Ysard, N. 2011, The global dust SED: tracing the nature and evolution of
    dust with DustEM, Astronomy and Astrophysics, 525, A103

Dalcanton, J. J., Williams, B. F., Lang, D., Lauer, T. R., Kalirai, J. S., Seth, A. C., Dolphin, A.,
    Rosenfield, P., Weisz, D. R., Bell, E. F., Bianchi, L. C., Boyer, M. L., Caldwell, N., Dong, H.,
    Dorman, C. E., Gilbert, K. M., Girardi, L., Gogarten, S. M., Gordon, K. D., Guhathakurta,
    P., Hodge, P. W., Holtzman, J. A., Johnson, L. C., Larsen, S. S., Lewis, A., Melbourne, J. L.,
    Olsen, K. A. G., Rix, H.-W., Rosema, K., Saha, A., Sarajedini, A., Skillman, E. D., & Stanek,
    K. Z. 2012, The Panchromatic Hubble Andromeda Treasury, ApJS, 200, 18

Dalcanton, J. J., Fouesneau, M., Hogg, D. W., Lang, D., Leroy, A. K., Gordon, K. D., Sandstrom,
    K., Weisz, D. R., Williams, B. F., Bell, E. F., Dong, H., Gilbert, K. M., Gouliermis, D. A.,
    Guhathakurta, P., Lauer, T. R., Schruba, A., Seth, A. C., & Skillman, E. D. 2015, The
    Panchromatic Hubble Andromeda Treasury. VIII. A Wide-area, High-resolution Map of Dust
    Extinction in M31, ApJ, 814, 3

de Grijs, R., & Bono, G. 2015, Clustering of Local Group distances: publication bias or correlated
    measurements? III. The Small Magellanic Cloud, arXiv.org, 179

De Marchi, G., & Panagia, N. 2014, The extinction law inside the 30 Doradus nebula, MNRAS, 445, 93

De Marchi, G., Panagia, N., & Girardi, L. 2014, Probing interstellar extinction near the 30 Doradus nebula with red giant stars, MNRAS, 438, 513

De Marchi, G., Panagia, N., Sabbi, E., Lennon, D., Anderson, J., van der Marel, R., Cignoni, M., Grebel, E. K., Larsen, S., Zaritsky, D., Zeidler, P., Gouliermis, D., & Aloisi, A. 2016, Hubble Tarantula Treasury Project - IV. The extinction law, MNRAS, 455, 4373

De Vis, P., Jones, A., Viaene, S., Casasola, V., Clark, C. J. R., Baes, M., Bianchi, S., Cassara, L. P., Davies, J. I., De Looze, I., Galametz, M., Galliano, F., Lianou, S., Madden, S., Manilla-Robles, A., Mosenkov, A. V., Nersesian, A., Roychowdhury, S., Xilouris, E. M., & Ysard, N. 2019, A systematic metallicity study of DustPedia galaxies reveals evolution in the dust-to-metal ratios, A & A, 623, A5

Dobashi, K., Bernard, J. P., Hughes, A., Paradis, D., Reach, W. T., & Kawamura, A. 2008, Extinction and dust/gas ratio in LMC molecular clouds, A & A, 484, 205

Dobashi, K., Bernard, J.-P., Kawamura, A., Egusa, F., Hughes, A., Paradis, D., Bot, C., & Reach, W. T. 2009, Extinction Map of the Small Magellanic Cloud Based on the SIRIUS and 6X 2MASS Point Source Catalogs, AJ, 137, 5099

Dolphin, A. 1997, A new method to determine star formation histories of nearby galaxies, Nature, 2, 397

Dolphin, A. E. 2000, WFPC2 Stellar Photometry with HSTPHOT, PASP, 112, 1383

—. 2002, Numerical methods of star formation history measurement and applications to seven dwarf spheroidals, MNRAS, 332, 91

—. 2013, On the Estimation of Random Uncertainties of Star Formation Histories, ApJ, 775, 76

Draine, B. T. 2003, Interstellar Dust Grains, Annual Review of Astronomy & Astrophysics, 41, 241

Draine, B. T., & Fraisse, A. A. 2009, Polarized Far-Infrared and Submillimeter Emission from Interstellar Dust, ApJ, 696, 1

Draine, B. T., & Li, A. 2007, Infrared Emission from Interstellar Dust. IV. The Silicate-Graphite-PAH Model in the Post-Spitzer Era, ApJ, 657, 810

Draine, B. T., Aniano, G., Krause, O., Groves, B., Sandstrom, K., Braun, R., Leroy, A., Klaas, U., Linz, H., Rix, H.-W., Schinnerer, E., Schmiedeke, A., & Walter, F. 2014, Andromeda's

Dust, ApJ, 780, 172

Dressel, L. 2014, Wide Field Camera 3 Instrument Handbook, Version 6.0, "Wide Field Camera 3 Instrument Handbook, Version 6.0", (Baltimore: STScI)

Dufour, R. J. 1984, in IAU Symposium, Vol. 108, Structure and Evolution of the Magellanic Clouds, ed. S. van den Bergh & K. S. D. de Boer, 353

Dunkin, S. K., & Crawford, I. A. 1998, Spatially resolved optical spectroscopy of the Herbig Ae/Vega-like binary star HD 35187, MNRAS, 298, 275

Dwek, E. 1998, The Evolution of the Elemental Abundances in the Gas and Dust Phases of the Galaxy, ApJ, 501, 643

Feldmann, R. 2015, The equilibrium view on dust and metals in galaxies: Galactic outflows drive low dust-to-metal ratios in dwarf galaxies, MNRAS, 449, 3274

Fitzpatrick, E. L. 1985, Interstellar extinction variations in the Large Magellanic Cloud, ApJ, 299, 219

—. 1999, Correcting for the Effects of Interstellar Extinction, PASP, 111, 63

Fleischer, A. J., Gauger, A., & Sedlmayr, E. 1992, Circumstellar dust shells around long-period variables. I. Dynamical models of C-stars including dust formation, growth and evaporation., Astronomy and Astrophysics, 266, 321

Florsch, A., Marcout, J., & Fleck, E. 1981, Aspects of the structure of the Small Magellanic Cloud, A & A, 96, 158

Francis, C., & Anderson, E. 2014, Two estimates of the distance to the Galactic Centre, MNRAS, 441, 1105

Gall, C., Hjorth, J., Watson, D., Dwek, E., Maund, J. R., Fox, O., Leloudas, G., Malesani, D., & Day-Jones, A. C. 2014, Rapid formation of large dust grains in the luminous supernova 2010jl, Nature, 511, 326

Galliano, F., Madden, S. C., Jones, A. P., Wilson, C. D., & Bernard, J.-P. 2005, ISM properties in low-metallicity environments. III. The spectral energy distributions of II Zw 40, He 2-10 and NGC 1140, A&A, 434, 867

Gardiner, L. T., & Hatzidimitriou, D. 1992, Stellar populations and the large-scale structure of the Small Magellanic Cloud. IV - Age distribution studies of the outer regions, MNRAS, 257, 195

Gardiner, L. T., & Hawkins, M. R. S. 1991, Stellar populations and large-scale structure of the SMC. III - The geometry of the northern and north-western outlying regions, MNRAS, 251, 174

Girardi, L. 2016, Red Clump Stars, ARA&A, 54, 95

Girardi, L., & Salaris, M. 2001, Population effects on the red giant clump absolute magnitude, and distance determinations to nearby galaxies, MNRAS, 323, 109

Glatt, K., Gallagher, III, J. S., Grebel, E. K., Nota, A., Sabbi, E., Sirianni, M., Clementini, G., Tosi, M., Harbeck, D., Koch, A., & Cracraft, M. 2008, An Accurate Age Determination for the Small Magellanic Cloud Star Cluster NGC 121 with the Hubble Space Telescope/Advanced Camera for Surveys, AJ, 135, 1106

Gordon, K. D., & Clayton, G. C. 1998, Starburst-like Dust Extinction in the Small Magellanic Cloud, ApJ, 500, 816

Gordon, K. D., Clayton, G. C., Misselt, K. A., Landolt, A. U., & Wolff, M. J. 2003, A Quantitative Comparison of the Small Magellanic Cloud, Large Magellanic Cloud, and Milky Way Ultraviolet to Near-Infrared Extinction Curves, ApJ, 594, 279

Gordon, K. D., Meixner, M., Meade, M. R., Whitney, B., Engelbracht, C., Bot, C., Boyer, M. L., Lawton, B., Sewiło, M., Babler, B., Bernard, J. P., Bracker, S., Block, M., Blum, R., Bolatto, A., Bonanos, A., Harris, J., Hora, J. L., Indebetouw, R., Misselt, K., Reach, W., Shiao, B., Tielens, X., Carlson, L., Churchwell, E., Clayton, G. C., Chen, C. H. R., Cohen, M., Fukui, Y., Gorjian, V., Hony, S., Israel, F. P., Kawamura, A., Kemper, F., Leroy, A., Li, A., Madden, S., Marble, A. R., McDonald, I., Mizuno, A., Mizuno, N., Muller, E., Oliveira, J. M., Olsen, K., Onishi, T., Paladini, R., Paradis, D., Points, S., Robitaille, T., Rubin, D., Sandstrom, K., Sato, S., Shibai, H., Simon, J. D., Smith, L. J., Srinivasan, S., Vijh, U., Van Dyk, S., van Loon, J. T., & Zaritsky, D. 2011, SURVEYING THE AGENTS OF GALAXY EVOLUTION IN THE TIDALLY STRIPPED, LOW METALLICITY SMALL MAGELLANIC CLOUD (SAGE-SMC). I. OVERVIEW, AJ, 142, 102

Gordon, K. D., Roman-Duval, J., Bot, C., Meixner, M., Babler, B., Bernard, J.-P., Bolatto, A., Boyer, M. L., Clayton, G. C., Engelbracht, C., Fukui, Y., Galametz, M., Galliano, F., Hony, S., Hughes, A., Indebetouw, R., Israel, F. P., Jameson, K., Kawamura, A., Lebouteiller, V., Li, A., Madden, S. C., Matsuura, M., Misselt, K., Montiel, E., Okumura, K., Onishi, T., Panuzzo, P., Paradis, D., Rubio, M., Sand strom, K., Sauvage, M., Seale, J., Sewiło, M., Tchernyshyov, K., & Skibba, R. 2014, Dust and Gas in the Magellanic Clouds from the HERITAGE Herschel Key Project. I. Dust Properties and Insights into the Origin of the Submillimeter Excess Emission, ApJ, 797, 85

Gordon, K. D., Fouesneau, M., Arab, H., Tchernyshyov, K., Weisz, D. R., Dalcanton, J. J., Williams, B. F., Bell, E. F., Bianchi, L., Boyer, M., Choi, Y., Dolphin, A., Girardi, L., Hogg,

D. W., Kalirai, J. S., Kapala, M., Lewis, A. R., Rix, H.-W., Sandstrom, K., & Skillman, E. D. 2016, The Panchromatic Hubble Andromeda Treasury. XV. The BEAST: Bayesian Extinction and Stellar Tool, ApJ, 826, 104

Gould, R. J., & Salpeter, E. E. 1963, The Interstellar Abundance of the Hydrogen Molecule. I. Basic Processes., ApJ, 138, 393

Gratton, R. G., Carretta, E., Bragaglia, A., Lucatello, S., & D'Orazi, V. 2010, The second and third parameters of the horizontal branch in globular clusters, A&A, 517, A81

Hagen, L. M. Z., Siegel, M. H., Hoversten, E. A., Gronwall, C., Immler, S., & Hagen, A. 2017, Swift Ultraviolet Survey of the Magellanic Clouds (SUMaC) - I. Shape of the ultraviolet dust extinction law and recent star formation history of the Small Magellanic Cloud, MNRAS, 466, 4540

Harris, J., & Zaritsky, D. 2001, A Method for Determining the Star Formation History of a Mixed Stellar Population, ApJS, 136, 25

—. 2004, The Star Formation History of the Small Magellanic Cloud, AJ, 127, 1531

—. 2009, The Star Formation History of the Large Magellanic Cloud, AJ, 138, 1243

Haschke, R., Grebel, E. K., & Duffau, S. 2012, Three-dimensional Maps of the Magellanic Clouds using RR Lyrae Stars and Cepheids. II. The Small Magellanic Cloud, AJ, 144, 107

Hatzidimitriou, D., & Hawkins, M. R. S. 1989, Stellar populations and large-scale structure of the SMC. II - Geometry of the north-eastern and south-western outlying regions, MNRAS, 241, 667

Hennebelle, P., & Falgarone, E. 2012, Turbulent molecular clouds, A & A Rev., 20, 55

Hill, A. S., Benjamin, R. A., Kowal, G., Reynolds, R. J., Haffner, L. M., & Lazarian, A. 2008, The Turbulent Warm Ionized Medium: Emission Measure Distribution and MHD Simulations, ApJ, 686, 363

Hoppe, P., Fujiya, W., & Zinner, E. 2012, Sulfur Molecule Chemistry in Supernova Ejecta Recorded by Silicon Carbide Stardust, The Astrophysical Journal Letters, 745, L26

Hoppe, P., & Zinner, E. 2000, Presolar dust grains from meteorites and their stellar sources, Journal of Geophysical Research, 105, 10371

Hunter, J. D. 2007, Matplotlib: A 2D Graphics Environment, Computing in Science and Engineering, 9, 90

Imara, N., & Blitz, L. 2007, Extinction in the Large Magellanic Cloud, ApJ, 662, 969

Isobe, T., Feigelson, E. D., Akritas, M. G., & Babu, G. J. 1990, Linear regression in astronomy., ApJ, 364, 104

Jacyszyn-Dobrzeniecka, A. M., Skowron, D. M., Mróz, P., Skowron, J., Soszyński, I., Udalski, A., Pietrukowicz, P., Kozłowski, S., Wyrzykowski, Ł., Poleski, R., Pawlak, M., Szymański, M. K., & Ulaczyk, K. 2016, OGLE-ing the Magellanic System: Three-Dimensional Structure of the Clouds and the Bridge Using Classical Cepheids, Acta Astron., 66, 149

Jacyszyn-Dobrzeniecka, A. M., Skowron, D. M., Mróz, P., Soszyński, I., Udalski, A., Pietrukowicz, P., Skowron, J., Poleski, R., Kozłowski, S., Wyrzykowski, Ł., Pawlak, M., Szymański, M. K., & Ulaczyk, K. 2017, OGLE-ing the Magellanic System: Three-Dimensional Structure of the Clouds and the Bridge using RR Lyrae Stars, Acta Astron., 67, 1

Kainulainen, J., Beuther, H., Henning, T., & Plume, R. 2009, Probing the evolution of molecular cloud structure. From quiescence to birth, A&A, 508, L35

Kapakos, E., & Hatzidimitriou, D. 2012, RR Lyrae variables in the Small Magellanic Cloud - II. The extended area: chemical and structural analysis, MNRAS, 426, 2063

Kroupa, P. 2001, On the variation of the initial mass function, MNRAS, 322, 231

Kurt, C. M., Dufour, R. J., Garnett, D. R., Skillman, E. D., Mathis, J. S., Peimbert, M., Torres-Peimbert, S., & Ruiz, M.-T. 1999, Hubble Space Telescope Observations of the Dusty Small Magellanic Cloud H II Region N88A, Astrophysical Journal, 518, 246

Lee, J.-K., Rolleston, W. R. J., Dufton, P. L., & Ryans, R. S. I. 2005, Chemical compositions of four B-type supergiants in the SMC wing, A&A, 429, 1025

Lequeux, J., Maurice, E., Prevot-Burnichon, M.-L., Prevot, L., & Rocca-Volmerange, B. 1982, SK 143 - an SMC star with a galactic-type ultraviolet interstellar extinction, A & A, 113, L15

Leroy, A. K., Bolatto, A., Gordon, K., Sand strom, K., Gratier, P., Rosolowsky, E., Engelbracht, C. W., Mizuno, N., Corbelli, E., Fukui, Y., & Kawamura, A. 2011, The CO-to-H_2 Conversion Factor from Infrared Dust Emission across the Local Group, ApJ, 737, 12

Li, A., & Draine, B. T. 2001, Infrared Emission from Interstellar Dust. II. The Diffuse Interstellar Medium, ApJ, 554, 778

Lombardi, M., & Alves, J. 2001, Mapping the interstellar dust with near-infrared observations: An optimized multi-band technique, A & A, 377, 1023

Madau, P., & Dickinson, M. 2014, Cosmic Star-Formation History, ARA&A, 52, 415

Maíz Apellániz, J., & Rubio, M. 2012, Ultraviolet extinction toward a quiescent molecular cloud in the Small Magellanic Cloud, A&A, 541, A54

Maíz Apellániz, J., Evans, C. J., Barbá, R. H., Gräfener, G., Bestenlehner, J. M., Crowther, P. A., García, M., Herrero, A., Sana, H., Simón-Díaz, S., Taylor, W. D., van Loon, J. T., Vink, J. S., & Walborn, N. R. 2014, The VLT-FLAMES Tarantula Survey. XVI. The optical and NIR extinction laws in 30 Doradus and the photometric determination of the effective temperatures of OB stars, A & A, 564, A63

Massa, D., Savage, B. D., & Fitzpatrick, E. L. 1983, Peculiar ultraviolet interstellar extinction, ApJ, 266, 662

Mighell, K. J. 1999, Parameter Estimation in Astronomy with Poisson-distributed Data. I.The χ^2 Statistic, ApJ, 518, 380

Monson, A. J., Freedman, W. L., Madore, B. F., Persson, S. E., Scowcroft, V., Seibert, M., & Rigby, J. R. 2012, The Carnegie Hubble Program: The Leavitt Law at 3.6 and 4.5 μm in the Milky Way, ApJ, 759, 146

Muller, E., Staveley-Smith, L., Zealey, W., & Stanimirović, S. 2003, High-resolution HI observations of the Western Magellanic Bridge, MNRAS, 339, 105

Muraveva, T., Subramanian, S., Clementini, G., Cioni, M. R. L., Palmer, M., van Loon, J. T., Moretti, M. I., de Grijs, R., Molinaro, R., & Ripepi, V. 2018, The VMC survey - XXVI. Structure of the Small Magellanic Cloud from RR Lyrae stars, MNRAS, 473, 3131

Murray, C. E., Peek, J. E. G., Di Teodoro, E. M., McClure-Griffiths, N. M., Dickey, J. M., & Dénes, H. 2019, The 3D Kinematics of Gas in the Small Magellanic Cloud, ApJ, 887, 267

Nataf, D. M., Gould, A., Fouqué, P., Gonzalez, O. A., Johnson, J. A., Skowron, J., Udalski, A., Szymański, M. K., Kubiak, M., Pietrzyński, G., Soszyński, I., Ulaczyk, K., Wyrzykowski, Ł., & Poleski, R. 2013, Reddening and Extinction toward the Galactic Bulge from OGLE-III: The Inner Milky Way's R$_V$ ~ 2.5 Extinction Curve, ApJ, 769, 88

Netzer, N., & Elitzur, M. 1993, The Dynamics of Stellar Outflows Dominated by Interaction of Dust and Radiation, ApJ, 410, 701

Nidever, D. L., Monachesi, A., Bell, E. F., Majewski, S. R., Muñoz, R. R., & Beaton, R. L. 2013, A Tidally Stripped Stellar Component of the Magellanic Bridge, ApJ, 779, 145

Noll, S., & Pierini, D. 2005, Dust properties of UV bright galaxies at z ~ 2, A&A, 444, 137

Paczyński, B., & Stanek, K. Z. 1998, Galactocentric Distance with the Optical Gravitational Lensing Experiment and HIPPARCOS Red Clump Stars, ApJL, 494, L219

Percival, S. M., & Salaris, M. 2003, An empirical test of the theoretical population corrections to the red clump absolute magnitude, MNRAS, 343, 539

Planck Collaboration, Ade, P. A. R., Aghanim, N., Alves, M. I. R., Aniano, G., Arnaud, M., Ashdown, M., Aumont, J., Baccigalupi, C., Banday, A. J., Barreiro, R. B., Bartolo, N., Battaner, E., Benabed, K., Benoit-Lévy, A., Bernard, J. P., Bersanelli, M., Bielewicz, P., Bonaldi, A., Bonavera, L., Bond, J. R., Borrill, J., Bouchet, F. R., Boulanger, F., Burigana, C., Butler, R. C., Calabrese, E., Cardoso, J. F., Catalano, A., Chamballu, A., Chiang, H. C., Christensen, P. R., Clements, D. L., Colombi, S., Colombo, L. P. L., Couchot, F., Crill, B. P., Curto, A., Cuttaia, F., Danese, L., Davies, R. D., Davis, R. J., de Bernardis, P., de Rosa, A., de Zotti, G., Delabrouille, J., Dickinson, C., Diego, J. M., Dole, H., Donzelli, S., Doré, O., Douspis, M., Draine, B. T., Ducout, A., Dupac, X., Efstathiou, G., Elsner, F., Enßlin, T. A., Eriksen, H. K., Falgarone, E., Finelli, F., Forni, O., Frailis, M., Fraisse, A. A., Franceschi, E., Frejsel, A., Galeotta, S., Galli, S., Ganga, K., Ghosh, T., Giard, M., Gjerløw, E., González-Nuevo, J., Górski, K. M., Gregorio, A., Gruppuso, A., Guillet, V., Hansen, F. K., Hanson, D., Harrison, D. L., Henrot-Versillé, S., Hernández-Monteagudo, C., Herranz, D., Hildebrand t, S. R., Hivon, E., Holmes, W. A., Hovest, W., Huffenberger, K. M., Hurier, G., Jaffe, A. H., Jaffe, T. R., Jones, W. C., Keihänen, E., Keskitalo, R., Kisner, T. S., Kneissl, R., Knoche, J., Kunz, M., Kurki-Suonio, H., Lagache, G., Lamarre, J. M., Lasenby, A., Lattanzi, M., Lawrence, C. R., Leonardi, R., Levrier, F., Liguori, M., Lilje, P. B., Linden-Vørnle, M., López-Caniego, M., Lubin, P. M., Macías-Pérez, J. F., Maffei, B., Maino, D., Mand olesi, N., Maris, M., Marshall, D. J., Martin, P. G., Martínez-González, E., Masi, S., Matarrese, S., Mazzotta, P., Melchiorri, A., Mendes, L., Mennella, A., Migliaccio, M., Miville-Deschênes, M. A., Moneti, A., Montier, L., Morgante, G., Mortlock, D., Munshi, D., Murphy, J. A., Naselsky, P., Natoli, P., Nørgaard-Nielsen, H. U., Novikov, D., Novikov, I., Oxborrow, C. A., Pagano, L., Pajot, F., Paladini, R., Paoletti, D., Pasian, F., Perdereau, O., Perotto, L., Perrotta, F., Pettorino, V., Piacentini, F., Piat, M., Plaszczynski, S., Pointecouteau, E., Polenta, G., Ponthieu, N., Popa, L., Pratt, G. W., Prunet, S., Puget, J. L., Rachen, J. P., Reach, W. T., Rebolo, R., Reinecke, M., Remazeilles, M., Renault, C., Ristorcelli, I., Rocha, G., Roudier, G., Rubiño-Martín, J. A., Rusholme, B., Sandri, M., Santos, D., Scott, D., Spencer, L. D., Stolyarov, V., Sudiwala, R., Sunyaev, R., Sutton, D., Suur-Uski, A. S., Sygnet, J. F., Tauber, J. A., Terenzi, L., Toffolatti, L., Tomasi, M., Tristram, M., Tucci, M., Umana, G., Valenziano, L., Valiviita, J., Van Tent, B., Vielva, P., Villa, F., Wade, L. A., Wandelt, B. D., Wehus, I. K., Ysard, N., Yvon, D., Zacchei, A., & Zonca, A. 2016, Planck intermediate results. XXIX. All-sky dust modelling with Planck, IRAS, and WISE observations, A&A, 586, A132

Prevot, M. L., Lequeux, J., Prevot, L., Maurice, E., & Rocca-Volmerange, B. 1984, The typical interstellar extinction in the Small Magellanic Cloud, A&A, 132, 389

Rachford, B. L., Snow, T. P., Destree, J. D., Ross, T. L., Ferlet, R., Friedman, S. D., Gry, C., Jenkins, E. B., Morton, D. C., Savage, B. D., Shull, J. M., Sonnentrucker, P., Tumlinson, J., Vidal-Madjar, A., Welty, D. E., & York, D. G. 2009, Molecular Hydrogen in the Far Ultraviolet Spectroscopic Explorer Translucent Lines of Sight: The Full Sample, ApJS, 180, 125

106

Rémy-Ruyer, A., Madden, S. C., Galliano, F., Galametz, M., Takeuchi, T. T., Asano, R. S., Zhukovska, S., Lebouteiller, V., Cormier, D., Jones, A., Bocchio, M., Baes, M., Bendo, G. J., Boquien, M., Boselli, A., DeLooze, I., Doublier-Pritchard, V., Hughes, T., Karczewski, O. Ł., & Spinoglio, L. 2014, Gas-to-dust mass ratios in local galaxies over a 2 dex metallicity range, A & A, 563, A31

Ripepi, V., Marconi, M., Moretti, M. I., Clementini, G., Cioni, M. R. L., de Grijs, R., Emerson, J. P., Groenewegen, M. A. T., Ivanov, V. D., & Piatti, A. E. 2016, The VMC Survey. XIX. Classical Cepheids in the Small Magellanic Cloud, ApJS, 224, 21

Ripepi, V., Cioni, M.-R. L., Moretti, M. I., Marconi, M., Bekki, K., Clementini, G., de Grijs, R., Emerson, J., Groenewegen, M. A. T., Ivanov, V. D., Molinaro, R., Muraveva, T., Oliveira, J. M., Piatti, A. E., Subramanian, S., & van Loon, J. T. 2017, The VMC survey - XXV. The 3D structure of the Small Magellanic Cloud from Classical Cepheids, MNRAS, 472, 808

Rolleston, W. R. J., Dufton, P. L., McErlean, N. D., & Venn, K. A. 1999, The chemical composition of the young, Inter-Cloud population, A & A, 348, 728

Rolleston, W. R. J., Venn, K., Tolstoy, E., & Dufton, P. L. 2003, The present-day chemical composition of the SMC from UVES spectra of the sharp-lined, B-type dwarf AV 304, A & A, 400, 21

Roman-Duval, J., Gordon, K. D., Meixner, M., Bot, C., Bolatto, A., Hughes, A., Wong, T., Babler, B., Bernard, J.-P., Clayton, G. C., Fukui, Y., Galametz, M., Galliano, F., Glover, S., Hony, S., Israel, F., Jameson, K., Lebouteiller, V., Lee, M.-Y., Li, A., Madden, S., Misselt, K., Montiel, E., Okumura, K., Onishi, T., Panuzzo, P., Reach, W., Remy-Ruyer, A., Robitaille, T., Rubio, M., Sauvage, M., Seale, J., Sewilo, M., Staveley-Smith, L., & Zhukovska, S. 2014, Dust and Gas in the Magellanic Clouds from the HERITAGE Herschel Key Project. II. Gas-to-dust Ratio Variations across Interstellar Medium Phases, ApJ, 797, 86

Roman-Duval, J., Jenkins, E. B., Williams, B., Tchernyshyov, K., Gordon, K., Meixner, M., Hagen, L., Peek, J., Sandstrom, K., Werk, J., & Yanchulova Merica-Jones, P. 2019, METAL: The Metal Evolution, Transport, and Abundance in the Large Magellanic Cloud Hubble Program. I. Overview and Initial Results, ApJ, 871, 151

Rubele, S., Girardi, L., Kerber, L., Cioni, M.-R. L., Piatti, A. E., Zaggia, S., Bekki, K., Bressan, A., Clementini, G., de Grijs, R., Emerson, J. P., Groenewegen, M. A. T., Ivanov, V. D., Marconi, M., Marigo, P., Moretti, M.-I., Ripepi, V., Subramanian, S., Tatton, B. L., & van Loon, J. T. 2015, The VMC survey - XIV. First results on the look-back time star formation rate tomography of the Small Magellanic Cloud, MNRAS, 449, 639

Rubele, S., Pastorelli, G., Girardi, L., Cioni, M.-R. L., Zaggia, S., Marigo, P., Bekki, K., Bressan, A., Clementini, G., de Grijs, R., Emerson, J., Groenewegen, M. A. T., Ivanov, V. D., Muraveva, T., Nanni, A., Oliveira, J. M., Ripepi, V., Sun, N.-C., & van Loon, J. T. 2018, The VMC

survey - XXXI: The spatially resolved star formation history of the main body of the Small Magellanic Cloud, MNRAS, 478, 5017

Russell, S. C., & Dopita, M. A. 1992, Abundances of the heavy elements in the Magellanic Clouds. III - Interpretation of results, ApJ, 384, 508

Sabbi, E., Gallagher, J. S., Tosi, M., Anderson, J., Nota, A., Grebel, E. K., Cignoni, M., Cole, A. A., Da Costa, G. S., Harbeck, D., Glatt, K., & Marconi, M. 2009, Star Formation History of the Small Magellanic Cloud: Six Hubble Space Telescope/Advanced Camera for Survey Fields, ApJ, 703, 721

Sabbi, E., Anderson, J., Lennon, D. J., van der Marel, R. P., Aloisi, A., Boyer, M. L., Cignoni, M., de Marchi, G., de Mink, S. E., Evans, C. J., Gallagher, III, J. S., Gordon, K., Gouliermis, D. A., Grebel, E. K., Koekemoer, A. M., Larsen, S. S., Panagia, N., Ryon, J. E., Smith, L. J., Tosi, M., & Zaritsky, D. 2013, Hubble Tarantula Treasury Project: Unraveling Tarantula's Web. I. Observational Overview and First Results, AJ, 146, 53

Sabbi, E., Lennon, D. J., Anderson, J., Cignoni, M., van der Marel, R. P., Zaritsky, D., De Marchi, G., Panagia, N., Gouliermis, D. A., Grebel, E. K., Gallagher, III, J. S., Smith, L. J., Sana, H., Aloisi, A., Tosi, M., Evans, C. J., Arab, H., Boyer, M., de Mink, S. E., Gordon, K., Koekemoer, A. M., Larsen, S. S., Ryon, J. E., & Zeidler, P. 2016, Hubble Tarantula Treasury Project. III. Photometric Catalog and Resulting Constraints on the Progression of Star Formation in the 30 Doradus Region, ApJS, 222, 11

Sandstrom, K. M., Bolatto, A. D., Draine, B. T., Bot, C., & Stanimirović, S. 2010, The Spitzer Survey of the Small Magellanic Cloud (S^{3}MC): Insights into the Life Cycle of Polycyclic Aromatic Hydrocarbons, ApJ, 715, 701

Sandstrom, K. M., Bolatto, A. D., Bot, C., Draine, B. T., Ingalls, J. G., Israel, F. P., Jackson, J. M., Leroy, A. K., Li, A., Rubio, M., Simon, J. D., Smith, J. D. T., Stanimirović, S., Tielens, A. G. G. M., & van Loon, J. T. 2012, The Spitzer Spectroscopic Survey of the Small Magellanic Cloud (S^{4}MC): Probing the Physical State of Polycyclic Aromatic Hydrocarbons in a Low-metallicity Environment, ApJ, 744, 20

Schlafly, E. F., Meisner, A. M., Stutz, A. M., Kainulainen, J., Peek, J. E. G., Tchernyshyov, K., Rix, H.-W., Finkbeiner, D. P., Covey, K. R., Green, G. M., Bell, E. F., Burgett, W. S., Chambers, K. C., Draper, P. W., Flewelling, H., Hodapp, K. W., Kaiser, N., Magnier, E. A., Martin, N. F., Metcalfe, N., Wainscoat, R. J., & Waters, C. 2016, The Optical-infrared Extinction Curve and Its Variation in the Milky Way, ApJ, 821, 78

Scowcroft, V., Freedman, W. L., Madore, B. F., Monson, A., Persson, S. E., Rich, J., Seibert, M., & Rigby, J. R. 2016, The Carnegie Hubble Program: The Distance and Structure of the SMC as Revealed by Mid-infrared Observations of Cepheids, ApJ, 816, 49

Sofia, U. J., Gordon, K. D., Clayton, G. C., Misselt, K., Wolff, M. J., Cox, N. L. J., & Ehrenfreund, P. 2006, Probing the Dust Responsible for Small Magellanic Cloud Extinction, ApJ, 636, 753

Somerville, R. S., Primack, J. R., & Faber, S. M. 2001, The nature of high-redshift galaxies, MNRAS, 320, 504

Speck, A. K., Corman, A. B., Wakeman, K., Wheeler, C. H., & Thompson, G. 2009, Silicon Carbide Absorption Features: Dust Formation in the Outflows of Extreme Carbon Stars, ApJ, 691, 1202

Stanimirovic, S., Staveley-Smith, L., Dickey, J. M., Sault, R. J., & Snowden, S. L. 1999, The large-scale HI structure of the Small Magellanic Cloud, MNRAS, 302, 417

Strom, K. M., Strom, S. E., & Yost, J. 1971, Circumstellar Shells in the Young Cluster NGC 2264, ApJ, 165, 479

Subramanian, S., & Subramaniam, A. 2009, Depth estimation of the Large and Small Magellanic Clouds, A & A, 496, 399

—. 2012, The Three-dimensional Structure of the Small Magellanic Cloud, ApJ, 744, 128

Subramanian, S., Rubele, S., Sun, N.-C., Girardi, L., de Grijs, R., van Loon, J. T., Cioni, M.-R. L., Piatti, A. E., Bekki, K., Emerson, J., Ivanov, V. D., Kerber, L., Marconi, M., Ripepi, V., & Tatton, B. L. 2017, The VMC Survey - XXIV. Signatures of tidally stripped stellar populations from the inner Small Magellanic Cloud, MNRAS, 467, 2980

Tang, J., Bressan, A., Rosenfield, P., Slemer, A., Marigo, P., Girardi, L., & Bianchi, L. 2014, New PARSEC evolutionary tracks of massive stars at low metallicity: testing canonical stellar evolution in nearby star-forming dwarf galaxies, MNRAS, 445, 4287

Testi, L., Birnstiel, T., Ricci, L., Andrews, S., Blum, J., Carpenter, J., Dominik, C., Isella, A., Natta, A., Williams, J. P., & Wilner, D. J. 2014, in Protostars and Planets VI, ed. H. Beuther, R. S. Klessen, C. P. Dullemond, & T. Henning, 339

Tolstoy, E., Hill, V., & Tosi, M. 2009, Star-Formation Histories, Abundances, and Kinematics of Dwarf Galaxies in the Local Group, ARA&A, 47, 371

Tolstoy, E., & Saha, A. 1996, The Interpretation of Color-Magnitude Diagrams through Numerical Simulation and Bayesian Inference, ApJ, 462, 672

Tosi, M., Greggio, L., & Focardi, P. 1989, Star formation in dwarf irregular galaxies - Preliminary results, APSS, 156, 295

Trumpler, R. J. 1930, Absorption of Light in the Galactic System, PASP, 42, 214

Van Der Walt, S., Colbert, S. C., & Varoquaux, G. 2011, The NumPy array: a structure for efficient numerical computation, Computing in Science and Engineering, 13, 22

Weingartner, J. C., & Draine, B. T. 2001, Dust Grain-Size Distributions and Extinction in the Milky Way, Large Magellanic Cloud, and Small Magellanic Cloud, ApJ, 548, 296

Weisz, D. R., Dolphin, A. E., Skillman, E. D., Holtzman, J., Dalcanton, J. J., Cole, A. A., & Neary, K. 2013, Comparing the ancient star formation histories of the Magellanic Clouds, MNRAS, 431, 364

Weisz, D. R., Dolphin, A. E., Skillman, E. D., Holtzman, J., Gilbert, K. M., Dalcanton, J. J., & Williams, B. F. 2014, The Star Formation Histories of Local Group Dwarf Galaxies. I. Hubble Space Telescope/Wide Field Planetary Camera 2 Observations, ApJ, 789, 147

Weisz, D. R., Dalcanton, J. J., Williams, B. F., Gilbert, K. M., Skillman, E. D., Seth, A. C., Dolphin, A. E., McQuinn, K. B. W., Gogarten, S. M., Holtzman, J., Rosema, K., Cole, A., Karachentsev, I. D., & Zaritsky, D. 2011, The ACS Nearby Galaxy Survey Treasury. VIII. The Global Star Formation Histories of 60 Dwarf Galaxies in the Local Volume, ApJ, 739, 5

Welch, D. L., McLaren, R. A., Madore, B. F., & McAlary, C. W. 1987, Distance moduli and structure of the Magellanic Clouds from near-infrared photometry of classical Cepheids, ApJ, 321, 162

Welty, D. E., Xue, R., & Wong, T. 2012, Interstellar H I and H_2 in the Magellanic Clouds: An Expanded Sample Based on Ultraviolet Absorption-line Data, ApJ, 745, 173

Williams, B. F. 2002, Clues about the star formation history of the M31 disc from WFPC2 photometry, MNRAS, 331, 293

Williams, B. F., Lang, D., Dalcanton, J. J., Dolphin, A. E., Weisz, D. R., Bell, E. F., Bianchi, L., Byler, N., Gilbert, K. M., Girardi, L., Gordon, K., Gregersen, D., Johnson, L. C., Kalirai, J., Lauer, T. R., Monachesi, A., Rosenfield, P., Seth, A., & Skillman, E. 2014, The Panchromatic Hubble Andromeda Treasury. X. Ultraviolet to Infrared Photometry of 117 Million Equidistant Stars, ApJS, 215, 9

Williams, B. F., Dolphin, A. E., Dalcanton, J. J., Weisz, D. R., Bell, E. F., Lewis, A. R., Rosenfield, P., Choi, Y., Skillman, E., & Monachesi, A. 2017, PHAT. XIX. The Ancient Star Formation History of the M31 Disk, ApJ, 846, 145

Winters, J. M., Le Bertre, T., Jeong, K. S., Nyman, L. Å., & Epchtein, N. 2003, Mass-loss from dusty, low outflow-velocity AGB stars. I. Wind structure and mass-loss rates, Astronomy and Astrophysics, 409, 715

Yanchulova Merica-Jones, P., Sandstrom, K. M., Johnson, L. C., Dalcanton, J., Dolphin, A. E.,

Gordon, K., Roman-Duval, J., Weisz, D. R., & Williams, B. F. 2017, The Small Magellanic Cloud Investigation of Dust and Gas Evolution (SMIDGE): The Dust Extinction Curve from Red Clump Stars, ApJ, 847, 102

Zaritsky, D., & Harris, J. 2004, Quantifying the Drivers of Star Formation on Galactic Scales. I. The Small Magellanic Cloud, ApJ, 604, 167

Zhukovska, S., Gail, H. P., & Trieloff, M. 2008, Evolution of interstellar dust and stardust in the solar neighbourhood, A & A, 479, 453

Zubko, V., Dwek, E., & Arendt, R. G. 2004, Interstellar Dust Models Consistent with Extinction, Emission, and Abundance Constraints, ApJS, 152, 211

Zubko, V. G. 1999, On the Model of Dust in the Small Magellanic Cloud, ApJL, 513, L29